

Transient optical properties as  
a signature of structural changes within  
FEL irradiated solids

Dissertation zur Erlangung des Doktorgrades  
des Fachbereiches Physik  
der Universität Hamburg

vorgelegt von

Victor Tkachenko

aus

Dubna (RUS)

Hamburg

2017

Gutachter der Dissertation: Prof. Dr. Beata Ziaja-Motyka  
Prof. Dr. Alexander Lichtenstein

Gutachter der Disputation: Prof. Dr. Nina Rohringer  
Dr. Mark Prandolini  
Dr. Martin Beye

Datum der Disputation: 31.07.2017

Vorsitzender des Fach-Promotionsausschusses: Prof. Dr. Michael Rübhausen

Leiter des Fachbereiches Physik: Prof. Dr. Michael Potthoff

Dekan der Fakultät für Mathematik,  
Informatik und Naturwissenschaften: Prof Dr. Heinrich Graener

# Zusammenfassung

Moderne Freie-Elektronenlaser (FEL) im XUV- und Röntgenbereich liefern Energie, die ausreicht, um Festkörpersysteme auf einer ultrakurzen Zeitskala aus dem Gleichgewichtszustand zu bringen. Die Änderungen in der komplexen Dielektrizitätsfunktion und die anschließenden Modifikationen der messbaren optischen Koeffizienten spiegeln dann die Strukturentwicklung des Materials außerhalb des Gleichgewichts wider. Die optische Untersuchung des Materials erlaubt es, die Reflektivität oder den Transmissionskoeffizienten mit Femtosekundenauflösung zu messen.

Aufgrund der Eigenschaften ihrer Bandstruktur sind Halbleiter von besonderem Interesse in der FEL-basierten Wissenschaft. Photonen eines Röntgen-FELs können Atome ionisieren und Elektronen vom Valenzband oder aus inneren Schalen in das Leitungsband eines Halbleiters anregen. Im Falle von großen Ladungsträgerdichten im Leitungsband ändert sich die Fläche der potentiellen Energie der Atome erheblich. Die anschließende Dynamik der Atome führt zu strukturellen Transformationen und irreversiblen Phasenübergängen auf einer Zeitskala von einigen 100 fs. Andererseits können Laserpulse auch thermische Phasenübergänge über Elektronen-Phononenkopplung und infolgedessen Erwärmung des Materials auf einer Zeitskala von  $\approx 1$  ps oder länger einleiten.

Die vorliegende Arbeit untersucht drei verschiedene Materialien -Diamant, Silizium und Galliumarsenid- die Röntgen-FEL-Strahlung ausgesetzt werden. Die entwickelten theoretischen Modelle, mithilfe derer die optische Antwort der untersuchten Materialien untersucht wird, basieren auf semi-empirischen Ansätzen wie, z.B., dem Tight-Binding-Modell, die einem die Möglichkeit geben, die Zeitentwicklung eines Systems mit einer großen Anzahl von Atomen zu behandeln. Die optischen Eigenschaften, die durch strukturelle Modifikationen beeinflusst werden, stellen dann die Verbindung zwischen den mikroskopischen Parametern und den experimentellen Observablen her. Entsprechende Experimente mit diesen Materialien wurden an Freien-Elektronen-Lasern im XUV- und Röntgenbereich wie FLASH, FERMIelettra, LCLS und SACLA durchgeführt. Die gewonnenen optischen Messungen erlaubten es, die Genauigkeit der Modelle zu verifizieren.

# Abstract

Present-day XUV and X-ray free-electron lasers deliver the energy sufficient to drive solid systems out of equilibrium on an ultrashort time scale. Structural evolution of the material in non-equilibrium is then reflected in the modification of its complex dielectric function and subsequent changes of the observable optical coefficients. The optical probing of the material allows to measure the reflection or transmission coefficients with a femtosecond time resolution.

Due to the features of their band structure, semiconductors are of particular interest for the FEL-related research. X-ray FEL photons are capable to ionize atoms and excite valence band or core hole electrons to the conduction band in them. In case of a large density of carriers in the conduction band the potential energy surface of atoms significantly changes. The subsequent atomic dynamics leads to structural transformations and irreversible phase transitions on a time scale of a few hundred fs. On the other hand, laser pulses may also induce thermal phase transitions via electron-phonon coupling and, consequently, lattice heating on a time scale of  $\sim 1$  ps or longer.

The thesis studies three different materials - diamond, silicon and gallium arsenide - exposed to X-ray FEL radiation. The developed theoretical models evaluating the optical response of investigated materials are based on semi-empirical approaches, such as tight-binding scheme, which give an opportunity to treat the time evolution of the system with a large number of atoms. The optical properties, being affected by structural modifications, then set up the link between the microscopic parameters and experimental observables. Corresponding experiments with these materials were performed at such XUV/X-ray FEL facilities as FLASH, FERMI@Elettra, LCLS and SACLA. The obtained optical measurements allowed to verify the accuracy of the models.

# List of publications

**2015** *Modeling of Nonthermal Solid-to-Solid Phase Transition in Diamond Irradiated with Femtosecond x-ray FEL Pulse*

N. Medvedev, V. Tkachenko, B Ziaja.

Contributions to plasma physics, vol. 55, p. 12 (2015)

*Time-resolved observation of band-gap shrinking and electron-lattice thermalization within X-ray excited gallium arsenide*

B. Ziaja, N. Medvedev, V. Tkachenko, T. Maltezopoulos, W. Wurth.

Scientific Reports, vol. 5, p. 18068 (2015)

**2016** *Transient optical properties of semiconductors under femtosecond x-ray irradiation*

V. Tkachenko, N. Medvedev, Z. Li, P. Piekarz, B. Ziaja.

Physics Review B, vol. 93, p. 144101 (2016)

*Transient changes of optical properties in semiconductors in response to femtosecond laser pulses*

V. Tkachenko, N. Medvedev, B. Ziaja.

Applied Sciences, vol. 6, no. 9, p. 238 (2016)

*Soft x-rays induce femtosecond solid-to-solid phase transition*

F. Tavella, H. Höppner, V. Tkachenko, N. Medvedev, F. Capotondi, T. Goltz, Y. Kai,

M. Manfredda, E. Pedersoli, M. Prandolini, N. Stojanovic, T. Tanikawa, U. Teubner, S. Toleikis, B. Ziaja.

arXiv:1612.06698 (2016); Nature Communications, submitted (2017)

**2017** *Electron-ion coupling in semiconductors beyond Fermi's golden rule*

N. Medvedev, Z. Li, V. Tkachenko, B. Ziaja.

Physics Review B, vol. 95, p. 014309 (2017)

*Pulse duration in seeded free-electron lasers*

P. Finetti, H. Höppner, E. Allaria, C. Callegari, F. Capotondi, P. Cinquegrana, M. Coreno, R. Cucini, M.B. Danailov, A. Demidovich, G. De Ninno, M. Di Fraia, R. Feifel, E. Ferrari, L. Fröhlich, D. Gauthier, T. Golz, C. Grazioli, Y. Kai, G. Kurdi, N. Mahne, M. Manfredda, N. Medvedev, I.P. Nikolov, E. Pedersoli, G. Penco, O. Plekan, M.J. Prandolini, K.C. Prince, L. Raimondi, P. Rebernik, R. Riedel, E. Rous-  
sel, P. Sigalotti, R. Squibb, N. Stojanovic, S. Stranges, C. Svetina, T. Tanikawa, U. Teubner, V. Tkachenko, S. Toleikis, M. Zangrando, B. Ziaja, F. Tavella, L. Giannessi.  
Physics Review X, accepted (2017)

*Picosecond Relaxation of X-ray Excited GaAs Bulk*

V. Tkachenko, V. Lipp, N. Medvedev, B. Ziaja.

High Energy Density Physics, accepted (2017)

# Contents

## LIST OF PUBLICATIONS

|          |   |           |
|----------|---|-----------|
| <b>1</b> | <b>Introduction</b>   | <b>1</b>  |
| <b>2</b> | <b>Theoretical basis</b>  | <b>5</b>  |
| 2.1      | Free-electron laser . . . . .                                   | 5         |
| 2.2      | Interaction of X-ray photons with matter . . . . .              | 9         |
| 2.3      | Electron-lattice interaction . . . . .                          | 11        |
| 2.4      | Optical properties . . . . .                                    | 12        |
| 2.5      | Electronic band structure . . . . .                             | 17        |
| 2.5.1    | Drude model . . . . .   | 17        |
| 2.5.2    | Ab initio approaches . . . . .                                  | 19        |
| 2.5.3    | Tight-binding model . . . . .                                   | 21        |
| <b>3</b> | <b>Construction of the model</b>                                | <b>23</b> |
| 3.1      | Calculation of CDF in random phase approximation . . . . .      | 23        |
| 3.2      | CDF formalism for inelastic scattering cross sections . . . . . | 27        |
| 3.3      | XTANT model . . . . .   | 31        |
| 3.4      | Optical coefficients in equilibrium . . . . .                   | 40        |
| <b>4</b> | <b>Non-equilibrium dynamics of FEL irradiated solids</b>        | <b>44</b> |
| 4.1      | Phase transitions . . . . .                                     | 44        |
| 4.2      | Diamond . . . . .   | 45        |

## CONTENTS

|          |   |            |
|----------|---|------------|
| 4.2.1    | Irradiation of diamond below and above graphitization threshold . . .     | 47         |
| 4.2.2    | Effect of non-equilibrium electron kinetics on optical properties . . .   | 60         |
| 4.2.3    | Optically induced radiation damage in diamond . . . . .                   | 61         |
| 4.2.4    | Measured X-ray induced graphitization of diamond . . . . .                | 64         |
| 4.2.5    | Diffusion processes . . . . .   | 72         |
| 4.3      | Silicon . . . . .   | 76         |
| 4.3.1    | Modelling of phase transitions in silicon . . . . .                       | 76         |
| 4.3.2    | Optically induced radiation damage in silicon . . . . .                   | 81         |
| 4.3.3    | Effect of electron-ion coupling on optical properties . . . . .           | 83         |
| 4.4      | Gallium arsenide . . . . .  | 86         |
| 4.4.1    | Electron-lattice thermalization in GaAs . . . . .                         | 86         |
| 4.4.2    | Band separation in semiconductors . . . . .                               | 94         |
| <b>5</b> | <b>Conclusions and outlook</b>  | <b>102</b> |
| 5.1      | Conclusions . . . . .   | 102        |
| 5.2      | Outlook . . . . .   | 105        |
|          | <b>Appendices</b>   | <b>108</b> |
| <b>A</b> | <b>Verlet algorithm</b>   | <b>108</b> |
| <b>B</b> | <b>Ehrenfest approximation in calculation of potential energy surface</b> | <b>110</b> |
| <b>C</b> | <b>Tight-binding parameters</b>   | <b>112</b> |
| <b>D</b> | <b>Cross sections for inelastic electron scattering</b>                   | <b>116</b> |
|          | <b>Bibliography</b>   | <b>119</b> |

# Chapter 1

## Introduction

Ultrashort laser pulses (of femtosecond time duration,  $\tau = 10^{-15}$  fs) generated by modern free-electron lasers (FEL) in XUV and X-ray range (LCLS [1], SACLA [2], FERMI [3], FLASH [4] etc.) are widely used today in physics, material science, chemistry and biology. A broad range of systems from gases to clusters and strongly correlated materials have been already studied in this way. The pulse interaction with matter affects its structure on molecular and atomic level. Depending on the pulse duration, intensity, coherence and incidence angle, FEL radiation can trigger different processes in matter, such as chemical reactions, radiation damage, phase transitions, and creates exotic states of matter etc. X-ray/XUV pulses can be used for various purposes. For example, hard X-rays (with photon energy  $\hbar\omega > 5$  keV) are of importance for X-ray crystallography due to their large penetration depth in the material and the wavelengths comparable with the interatomic distance. On the other hand, soft X-rays ( $\hbar\omega < 5$  keV) and XUV ( $10$  eV  $< \hbar\omega < 124$  eV) are efficient for the processes where photoabsorption is strongly involved, as at such energies it dominates over the Compton scattering.

In our work we are focusing on the simulation of electronic kinetics and atomic dynamics in bulk semiconductors, which leads to structural transformations. The Fermi level in semiconductors is located between the valence band and the conduction band. The bands herewith are situated much closer to each other than in insulators, and the band gap width

in semiconductors may vary from  $\sim 0.1$  eV to a few eVs depending on classification. This implies the situation that in an external field electrons, which at the room temperature occupy only the valence band, can be excited, overcome the band gap and be transferred to the conduction band, thus creating holes in the valence band and forcing the system out of equilibrium. If the number of electron-hole pairs is sufficient, the consequent interatomic potential changes, and atomic relocations then lead to structural modifications of semiconductors. Thus, changing structural properties of semiconductors are interesting not only from the prospective of their application in material science, but also as a phenomenon, in which initial electron-hole excitation triggers a complex transformation process. In case of photoexcitation it is often sufficient to reach the necessary photon density with a single FEL pulse in order to promote enough electrons to the conduction band. It is also easier to deal with a single pulse from the simulation point of view as well as from the experimental perspective, as the modern timing tools can define pulse duration with femtosecond accuracy. Therefore, in our research we will consider simulations and experiments where a single FEL *pump* pulse was used.

The work contains four main Chapters. In Chapter 2 we provide the theoretical background which is vital for our research. An overview of the principle of FEL source work is given in the beginning of the Chapter. Then we subsequently discuss processes that take place within the material after the FEL shot, from absorption of photons by electrons to electron-lattice equilibration. Later we introduce optical properties, which can be measured during the evolution of these processes, and discuss band structure formalisms which can be potentially applied. In Chapter 3 we construct our theoretical model which is able to account for the processes highlighted in Chapter 2 and to calculate the optical properties synchronously with atomic dynamics. At the end of this Chapter we test the model on the materials in equilibrium. In Chapter 4 we come to the actual results of our work. In this work, we discuss the ultrafast (on a time scale up to several picoseconds,  $t \sim 10^{-12}$  s) transient phenomena in three materials - diamond as a crystal structure of carbon, silicon and gallium arsenide. Particularly we study transient dynamics of the laser-induced graphitization of diamond, amorphization of silicon and electron-phonon coupling in GaAs

below damage threshold. The Chapter 5 is dedicated to the conclusions of the work and outlook of the future development of the model and its applications.

Ultrafast phase transitions in diamond and silicon, which we observe, can also be results of a very high density of charge carriers in the conduction band and a corresponding potential energy surface change. Such kind of phase transitions is called non-thermal, as it is not induced by electron-phonon coupling which is typical for a conventional thermal phase transition. Note, that all of these phenomena have been known for significant amount of time, but so far they have been investigated primarily as a consequence of irradiation in optical regime. In contrast, here we concentrate on XUV/X-ray irradiation, proving that such effects can occur in this photon energy range as well. Moreover, semiconducting materials nowadays are used in X-ray optics and then all possible X-ray damage effects should be studied to estimate their radiation tolerance.

There are several ways to trace the non-equilibrium dynamics in theory and experiment. Here we trace it by calculation of the optical response in irradiated materials. This method is chosen as optical constants like reflectivity or transmittance distinctly characterize structural properties of the materials, and are accurately measured in the experiments on a short time scale. The pump-probe technique allows to acquire a time-resolved picture of the structural processes and to unveil their mechanisms by measuring the optical probe pulse signal interacting with the material.

As the band structure of the semiconductors cannot be described accurately enough without quantum theory and on the other hand pure *ab initio* methods are computationally inefficient for the descriptions of the systems with many atoms under non-equilibrium in time-resolved manner, we arrive at the semi-empirical transferable tight-binding description of the band structure. In addition, we are using classical molecular dynamics for treating the atomic motion. We also adopt the idea of separating all electrons in the solid system in two domains and treating them either with Monte Carlo method or with thermodynamical approach, depending on their energy. The calculation of optical properties is based on tight-binding approach and complex dielectric function (CDF) formalism in the random phase approximation (RPA). Such fusion of numerical tools makes the model called XTANT

(X-ray induced thermal and non-thermal phase transitions) [5] hybrid and transferable between different materials. For prediction of non-equilibrium temperature and electron-phonon coupling in GaAs we also apply the theoretical description based on rate equations, Drude model and two-temperature model.

# Chapter 2

## Theoretical basis

### 2.1 Free-electron laser

A free-electron laser (FEL) is a light source which is able to generate coherent, tunable high-power radiation. The generated wavelengths by modern FELs range from microwaves to X-rays. The key feature of FEL is a usage of an undulator (a wiggler), which is essentially a set of magnets, forcing the electron beam to wiggle transversely along the axis of the undulator (wiggler). Acceleration of electrons results in the emission of photons as in the synchrotron. In an FEL the electrons are united into microbunches and separated by one optical wavelength along the propagation axis, thus emitted radiation is monochromatic and coherent. The feedback of the emitted radiation onto the electron beam is called self-amplified spontaneous emission (SASE) [6, 7], which is employed on X-ray free electron laser facilities (XFEL). The modern FELs include VUV and soft X-ray lasers such as FERMI@Elettra in Italy [3] and FLASH in Hamburg [4], and those designed for hard X-rays the Linac Coherent Light Source (LCLS) in the USA [1], SACLA in Japan [2], SwissFEL in Switzerland [8] and European XFEL in Hamburg [9], which is expected to be in operational regime in the second half of 2017.

The XFEL radiation has a wavelength of an order of Angstrom ( $10^{-10}$  m) which is close to the size of an atom. At the same time, XFEL produces ultrashort pulses (down to a few

femtosecond time duration), which is immensely important for structural studies, because the pulse outruns the radiation damage. Together with brilliance (the number of photons per second propagating through a given cross section area and within a given narrow solid angle and spectral bandwidth) much higher than in synchrotrons of any generation (see Fig. 2.1) this makes XFEL a unique tool for investigating time-resolved dynamics of matter on a molecular and atomic scale. Therefore, XFELs have found their application in photon and material science; atomic, molecular, and optical physics (AMO); structural biology; chemistry; medical physics. Ultrafast X-ray imaging leads to a creation of molecular movies which may tell a lot about so far unexplored ultrafast processes within the materials. High intensity of X-ray pulses allows to obtain single-shot diffraction images from single molecules with high spatial resolution.

SASE FEL pulses contain independent, temporally coherent emission spikes [6]. The temporal length of the spikes may vary from hundreds of attoseconds to several femtoseconds. Recent investigations show [10] that, for example, at FLASH the generation of short FEL pulses with high temporal coherence, close to single spike is achievable in the VUV and soft X-ray range.

For accurate measurements, certain pulse parameters have to be accurately determined. One of the most important parameters is a pulse duration which is important in all time resolved experiments and also for the proper definition of the peak FEL intensity. The pulse duration can be evaluated by using autocorrelation measurements or via cross-correlation techniques which in principle compare the investigated pulse with a certain model pulse. Modern methods are capable of providing temporal measurements of complex pulses with multiple peaks both of spatial and temporal character [11]. The other important properties of the pulse are the pulse energy and its shape. With pulse shaping techniques, the pulse source can be modified in terms of amplitude, phase and duration by special devices such as amplifiers or compressors.

Apart of the free-electron laser itself, another key point of X-ray spectroscopy is a usage of the pump-probe techniques. The pump-probe principle was intensively employed before the invention of XUV/X-ray FELs, for example, in two-color measurements with

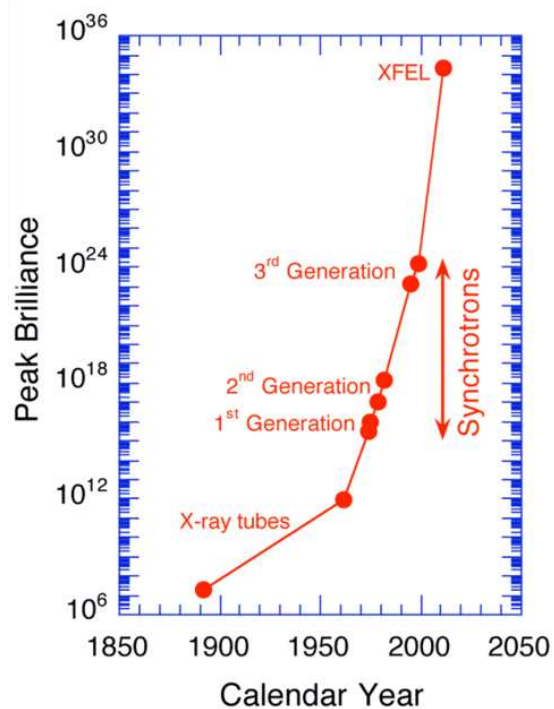


**Figure 2.1:** The order of peak brilliance (in photons/s/mm<sup>2</sup>/mr<sup>2</sup>/0.1%bandwidth) of X-ray sources commissioned at different times. X-ray free electron lasers can be 10 orders of magnitude brighter than third generation synchrotrons (e.g. Petra III, ESRF). The picture is taken from <https://www.psi.ch/swissfel/why-swissfel>.

two optical pulses with different wavelength [12, 13]. The invention of FELs sufficiently extended the scope of using the pump-probe technique. In a pump-probe scheme, the FEL source can be used in combination with another laser, usually an optical one. First, an FEL shot hits the sample and induces an excitation process within it. Then, with an adjustable time delay a probe pulse is sent to the sample (Fig. 2.2). Afterwards, the transmission or reflection signal of the probe pulse can be measured. By scanning the sample with probe pulses with a definite delay, one can obtain the transmission or reflection coefficient as a function of time delay between pump and probe pulses, and in such a manner reconstruct the excitation process in the sample. So, briefly speaking, the pump pulse launches the process and the probe pulse tracks it. As the probe pulse signal contains information about the optical properties of the material, this implies that from the optical properties, measured in the experiment, we may acquire the information on the temporal processes occurring within the material.

Nowadays, XUV or X-ray FEL pulses may be used as probes as well. At the beginning, the FEL pump – FEL probe schemes were based on time-delayed holography [14], where the probe pulse was formed by the pump reflected from the mirror, or on autocorrelation principle, where both pump and probe pulses were generated from one electron bunch and the incoming light was split in two parts by a focusing mirror [14, 15]. Thus, only one colour experiments were available. However in 2013 the LCLS group reported [14, 16] that by using a double undulator scheme, temporally and spectrally separated pump and probe pulses can be generated. This opened wide opportunities for studies of the radiation-matter interactions. With X-ray probe pulse, the X-ray diffraction pattern from the sample is reconstructed. Then, the evolution of Bragg peaks in diffraction images or profiles is used to understand the evolution of the structure of the investigated material.

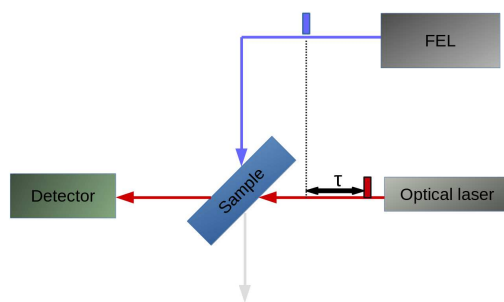


**Figure 2.2:** Schematic picture of a pump-probe experiment. The time  $\tau$  stands for the time delay between the pump and probe pulses.

## 2.2 Interaction of X-ray photons with matter

In general, X-ray photons are known for the capability to penetrate deep into the material, i.e., they have relatively high attenuation length in comparison to optical photons or to infrared radiation. Another important property of X-rays, which was already mentioned in the previous Chapter, is that an X-ray wavelength is comparable with the size of an atom and with the interatomic distance between atoms in a crystal structures of solids. For the majority of materials, X-rays are also practically non-refractive. All these characteristic features of X-rays make them an efficient tool for investigation of solid state structures, along with electron diffraction and neutronography [17].

Irradiation of solids by X-ray photons triggers a number of processes within them. Let us discuss these processes in detail. Immediately after the start of X-ray photons propagation within the material, they begin to photoionize atoms by removing bound electrons from the atomic shells. X-ray photons are able to excite the strongly bound electrons in the atoms from the core shells, in such a way creating core holes. If the photon energy exceeds the binding energy of electrons, a photoionization cross section or a probability of emitting an electron is high. If a single photon energy is below such barriers, multi-photon ionization by several photons combining their energies is still possible, and intense coherent laser pulses raise the probability of multi-photon ionization up.

Direct photoabsorption in XUV regime causes inverse bremsstrahlung heating of slow

electrons as photons exchange their kinetic energy with them in the field of nuclei. Excited electrons after emission may also ionize atoms if they have enough energy: via inelastic scattering. This process is called secondary impact ionization. The elastic scattering, which does not lead to the significant electron energy loss during a scattering event, is also feasible. Secondary electrons themselves increase electron density within the material. A highly charged system is created as a result, and in finite-size samples, this can cause Coulomb explosion after high-energy electrons leave the system. Thermalization of electrons is achieved through electron-electron collisions on a time scale of 10-100 fs, which is much faster than for an ion system because of a large mass difference between ions and electrons.

Recombination of ions with electrons is essentially an inverse process of the secondary ionization. In case of three-body recombination, a spectator electron near an ion receives the kinetic energy released by the recombining electron. The ion charge decreases due to the electron-ion recombination, and the ion can experience photoionization again. This process highly depends on the electron charge and density. In case of radiative recombination, a photon with the wavelength, corresponding to the released energy, is emitted.

The core holes formed by removing electrons from the core shells typically relax via Auger effect in light elements. An electron from a higher energy level may fill a vacancy (e.g., an electron from L-level fills the K-shell core hole). The released energy, equal to the difference between the binding energies of the levels, may then be transferred to a second, higher-lying electron. Thus, this so-called Auger-electron will be removed from the shell, additionally ionizing the atom. The kinetic energy of an Auger-electron thus depends on the type of the atom and its shell structure. Another way of filling the vacancy in inner-shell hole is a radiative process when the energy is carried-off by the photon. Heavy atoms with a large atomic number and large transition energies primarily decay via such radiative process, while for light atoms with a small  $Z$ -number Auger decay is more probable.

## 2.3 Electron-lattice interaction

After electrons absorb energy from the incoming laser pulse, they start to exchange their energy with each other as we stated in the previous Section. At the same time they also exchange their energy with lattice, but in each scattering event they can transfer only a small amount of energy. Therefore, this process lasts on a longer time scale (typically within several picoseconds). This stage of the system evolution is called electron-lattice equilibration. By this exchange, the system evolves towards the equilibrium. After the photoionization events and electron cascading, the electron temperature exceeds the lattice temperature. The electron subsystem then loses the gained energy via emission of phonons or the so-called electron-phonon coupling [18]. In solid state physics a phonon represents a quant of the vibrational mode of the crystal lattice. Thus, the accumulated energy of electrons in non-equilibrium is being transformed to the vibrational excitation of the lattice. Atoms of the lattice gain kinetic energy and start to move from their equilibrium positions. The temperature of electrons starts decreasing, while atomic temperature, in contrast, is increasing. Ultimate flattening of the temperatures of the two subsystems results in the electron-lattice thermalization.

Another process in a bulk material that lowers electron temperature is the thermal diffusion of hot electrons from the laser excited area to unexcited cold regions within the material [18]. In general, the diffusion means that particles from the regions with their high concentration penetrate into the regions of their lower concentration to create a uniform carrier distribution. In physics of semiconductors, the Einstein approach, originally applied to gases, is widely used to describe electronic diffusion. According to it, the diffusion coefficient, defining essentially the speed of the diffusion process, is obtained from the carrier mobility which accounts for the response of the system to a small perturbation [19].

## 2.4 Optical properties

XTANT model (X-ray induced thermal and non-thermal phase transitions) proved itself to be an efficient tool for investigating a non-equilibrium evolution of electronic and atomic subsystems in XUV and soft X-ray irradiated solids [5, 20, 21]. Such important parameters as band gap width, potential and kinetic energies of electronic and atomic subsystems, electron and atomic temperatures, number of electrons in the conduction band can be estimated with XTANT. Also, atomic snapshots can be recorded. However, in order to make direct comparisons of the model predictions with an experiment, we need some macroscopic experimental observables.

Optical coefficients of materials such as reflectivity and transmittance are widely measured in numerous experiments. The modern pump-probe techniques, where the optical probe follows the pump pulse with a certain time delay, allow to measure transient optical properties of irradiated materials. The time resolution of such pump-probe experiments can achieve a few femtoseconds [22–24]. Thus, the processes going on inside the materials on a femtosecond time scale can be detected, if these processes influence the optical properties. For example, electronic excitation and especially phase transitions lead to abrupt changes of optical properties within materials. By comparing transient optical coefficients, obtained in the experiment, with the theoretically modelled ones, we can get information on a presence and a time scale of the induced structural transformations and phase transitions.

Optical properties of a material can be expressed through a complex index of refraction  $\tilde{n}$  [25]:

$$\tilde{n}(\omega) = n(\omega) + ik(\omega). \quad (2.1)$$

Here  $n(\omega)$  and  $k(\omega)$  are correspondingly real and imaginary parts of the complex index of refraction, which are dependent on the frequency of the probe pulse.

The reflection coefficient (or reflectivity) of the material is a fraction of the incident light energy that was reflected by the surface of the material. Correspondingly, the transmission coefficient (or transmissivity) is a fraction of the incident light energy which was transmit-

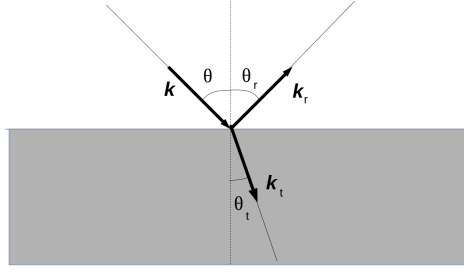


**Figure 2.3:** Schematic picture of the incident ray  $\mathbf{k}$ , reflected ray  $\mathbf{k}_r$  and the transmitted ray  $\mathbf{k}_t$  and the corresponding angles  $\theta$ ,  $\theta_r$ ,  $\theta_t$  on the border between two media.

ted through the material. Incident, reflected and transmitted rays are schematically shown in Fig. 2.3. They are determined by the boundary conditions for electromagnetic waves on the border of the materials. The reflectivity coefficient is defined by the Fresnel law as:

$$R = \left| \frac{\cos \theta - \tilde{n} \cos \theta_t}{\cos \theta + \tilde{n} \cos \theta_t} \right|^2, \quad (2.2)$$

where angle  $\theta$  is an angle of the ray propagation in respect to the normal in the vacuum ( $\tilde{n}_{vac} = 1$ ) and  $\theta_t$  is an angle to the normal in the material. According to the fundamental Snell's law  $n_{vac} \sin \theta = n \sin \theta_t$  one can rewrite the expression Eq. (2.2) for the reflectivity coefficient as:

$$R = \left| \frac{\cos \theta - \sqrt{\tilde{n}^2 - \sin^2 \theta}}{\cos \theta + \sqrt{\tilde{n}^2 - \sin^2 \theta}} \right|^2. \quad (2.3)$$

The transmission coefficient of the material also depends on the material thickness  $d$  and the wavelength of the incident probe pulse  $\lambda$ . As we usually deal with thick bulk material and femtosecond probe pulses, in most cases we can approximate our model to only first ray propagation with no interference effects included from multiple reflections on the material boundaries. In this case, the expression for the transmission coefficient can be written in the following form [26, 27]:

$$T = \left| \frac{4 \cos \theta \sqrt{\tilde{n}^2 - \sin^2 \theta} \cdot e^{-i \frac{2\pi d}{\lambda} \sqrt{\tilde{n}^2 - \sin^2 \theta}}}{(\cos \theta + \sqrt{\tilde{n}^2 - \sin^2 \theta})^2} \right|^2, \quad (2.4)$$

The absorption coefficient can be obtained from the normalization condition:

$$A = 1 - T - R. \quad (2.5)$$

The components of the complex index of refraction are connected with components of a complex dielectric function (CDF)  $\varepsilon(\omega) = \varepsilon' + i \cdot \varepsilon''$  by relations:

$$\begin{aligned} n^2 &= \frac{1}{2} \left( \sqrt{\varepsilon'^2 + \varepsilon''^2} + \varepsilon' \right), \\ k^2 &= \frac{1}{2} \left( \sqrt{\varepsilon'^2 + \varepsilon''^2} - \varepsilon' \right). \end{aligned} \quad (2.6)$$

The complex dielectric function is an essential property of the material which characterizes its response to an external electric field. CDF is tightly bound with the band structure of solids as its imaginary part is directly related to the probability of photoabsorption. It has electromagnetic origin and can be defined through Maxwell's equations:

$$\begin{aligned} \nabla \cdot \mathbf{D} &= \rho, \\ \nabla \times \mathbf{E} + \frac{\partial \mathbf{B}}{\partial t} &= 0, \\ \nabla \cdot \mathbf{B} &= 0, \\ \nabla \times \mathbf{H} - \frac{\partial \mathbf{D}}{\partial t} &= \mathbf{J}, \end{aligned} \quad (2.7)$$

where  $\mathbf{E}$  denotes the electric field,  $\mathbf{H}$  denotes the magnetic field,  $\rho$  is a free charge density,  $\mathbf{J}$  is a free current density,  $\mathbf{D}$  is a electric displacement,  $\mathbf{B}$  is a magnetic flux density. The first equation represents the Gauss's law and describes how the charge density  $\rho$  within the material is connected to the electric displacement  $\mathbf{D}$ . In turn, the electric displacement is connected with a vector of an electric field and an electric dipole polarization vector  $\mathbf{P}$ :

$$\mathbf{D} = \epsilon_0 \mathbf{E} + \mathbf{P}, \quad (2.8)$$

where  $\epsilon_0$  is the vacuum electric permittivity (which is a fundamental constant expressed in SI units). Considering the linear proportionality of the polarization to the magnitude of the applied field and isotropicity of the material in space, the polarization vector and the electric displacement can be written as follows [28]:

$$\begin{aligned} \mathbf{P} &= \epsilon_0 \chi_e \mathbf{E}, \\ \mathbf{D} &= \varepsilon \epsilon_0 \mathbf{E}, \end{aligned} \quad (2.9)$$

where  $\chi_e$  is the linear electric susceptibility. The dielectric constant  $\varepsilon$  is therefore defined as  $\varepsilon = 1 + \chi_e$ . In other words, this is the ratio of the electric permittivity in the material to the permittivity in vacuum. In an isotropic material the dielectric function is a scalar quantity. In a general case, this is a tensor relating each component of  $\mathbf{P}$  to all components of  $\mathbf{E}$ . It is dependent on many factors, characterizing the state of the material such as its temperature and pressure, the molecular and atomic structure, excitation level etc. [28]

The propagating electric field is described by the equation:

$$\mathbf{E} = \mathbf{E}_0 e^{i(\mathbf{k}\mathbf{x} - \omega t)}, \quad (2.10)$$

where the frequency  $\omega$  and the magnitude of the wave vector  $\mathbf{k}$  are related as [28]:

$$\omega(k) = \frac{1}{\sqrt{\varepsilon\epsilon_0\mu\mu_0}}k. \quad (2.11)$$

The coefficients  $\mu_0$  and  $\mu$  are magnetic permeability of vacuum and of the material correspondingly. The phase velocity of the wave is then determined from the known formula as:

$$v = \frac{\omega}{k} = \frac{1}{\sqrt{\varepsilon\epsilon_0\mu\mu_0}} = \frac{c}{\tilde{n}}, \quad (2.12)$$

where  $c = (\epsilon_0\mu_0)^{-1/2}$  is the phase velocity in vacuum, and  $\tilde{n} = \sqrt{\varepsilon\mu}$  is the refractive index of the medium. For frequencies in the optical part of the spectrum the magnetic permeability  $\mu = 1$ . Thus, we come to the relation that was first mentioned in Eq. (2.6).

Apart from well-known reflectivity and transmissivity, other optical parameters of the excited materials can be measured during the experiment. Let us briefly highlight these opportunities, although we do not investigate them later in this study.

An example of another optical property which can be measured in the regime of linear response is the light emittance or luminescence [28]. This effect is based on the spontaneous emission of radiation and can be explained only on the quantum level. Emission due to the luminescence has a non-thermal nature and occurs after light absorption. Luminescence is possible if the spectrum of the matter is discrete and its energy levels are separated - that is the reason why metals do not produce luminescence. After being excited to the high-lying state with energy  $E_2$ , the atom may spontaneously decay to a lower level with

energy  $E_1$ , releasing the photon with the energy  $E_2 - E_1 = \hbar\omega$ . The luminescence rate can be estimated as a ratio of the number of emitted photons  $N_e$  to the number of absorbed photons  $N_p$ . The frequency of the emitted light is usually different from the one of the absorbed light.

The experimental values of luminescence can be measured in a time-resolved way, or as a function of carrier density [28]. For sub-picosecond measurements, the up-conversion method described by Shah et al. [29] is widely used. The method has much in common with pump-probe techniques. The pump pulse excites the system, and the probe pulse follows it until some luminescent light has already been emitted. Then, a special interference filter selects a definite frequency which is in a focus of the experiment.

An example of the non-linear optical effect is the second-harmonic generation (SHG), when the sample converts the incident radiation of frequency  $\omega$  to the radiation of frequency  $2\omega$  [28]. This is a particular case of a sum frequency generation, and it is feasible only in media without inversion symmetry, i.e., if its crystal structure does not belong to the point group with the inversion center of symmetry. A non-linear bulk material gives a contribution to the second order of susceptibility  $\chi^{(2)}$ . This contribution depends on the orientation of molecules within the material, i.e., its structural order. The behaviour of  $\chi^{(2)}$  during a laser-induced phase transition in GaAs was considered, for instance, in [30]. In this case, the second-harmonic signal depends on the non-linear second-order susceptibility as well as on the linear dielectric functions  $\epsilon(\omega)$  and  $\epsilon(2\omega)$ . These dependencies have to be sorted out. By measuring the second-harmonic signal as a probe, the disordering of the crystalline lattice of GaAs can be detected, when the  $\chi^{(2)}$  goes to zero.

The more general case is a sum-frequency generation (SFG), when due to the annihilation of two incoming photons at different frequencies  $\omega_1$  and  $\omega_2$ , a photon at frequency  $\omega = \omega_1 + \omega_2$  is emitted. The signals at visible frequencies are very often generated from near-infrared and visible beams. There are also even more complicated techniques available such as four-wave mixing (FWM) [28, 31, 32], which we will not discuss here.

## 2.5 Electronic band structure

The basis for the models describing structural evolution of the atomic and molecular systems is an accurate determination of their electronic band structure. Here, we will introduce the various models used for this purpose and discuss their advantages and drawbacks.

### 2.5.1 Drude model

The Drude model for electrons was proposed by Paul Drude in 1900, and it was one of the first attempts to explain electro- and thermal conductivity in metals after discovery of an electron by Thomson. The model is based on the kinetic theory and assumes classical behaviour of free-electron gas in an external field of positively charged heavy stationary ions.

The electrons in the model are represented as ideal elastic spheres which float along straight trajectories and collide with ions, changing the direction of their floating after a collision. The duration of the collision  $\tau_c$  tends to zero, i.e. it is supposed to be instantaneous [33]. The long-range interactions between electrons or between an electron and ions are neglected except at the instant of the collision. The characteristic parameters of the electron behaviour are the relaxation time  $\tau$ , i.e., average time between two collisions for one propagating particle, and a mean free path of an electron,  $\lambda = v_0\tau$ , where  $v_0$  is the average speed of the electron.

Despite the simplicity of the Drude model and a number of approximations made (for electron collisions and scattering), for a long time it has been used for the estimation of thermal and electric properties in metals, and is still applied for their qualitative description. However, it has been known that the drawbacks of the Drude theory may lead to false predictions of optical properties in metals, first of all, because of the complicated frequency dependence which can not be taken into account by the Drude model. Even sodium, which is a metal of the first group in the periodic table, reveals the frequency dependence which is not reproduced by Drude-model predictions [33]. Moreover, the band structure of semiconductors and dielectrics cannot be properly treated with the Drude model, as some electrons

are bound there and the free-electron approximation is not applicable for them.

A complex dielectric function in the Drude model, which does not take interband transitions in the semiconductor into account, is defined as [34]:

$$\varepsilon(\omega) = \varepsilon_0 + \frac{i}{\omega} \frac{\omega_p^2 \tau}{1 - i\omega\tau}, \quad (2.13)$$

where  $\varepsilon_0$  is the unexcited material dielectric constant;  $\omega_p = \sqrt{n_e e^2 / m^* \varepsilon_0}$  is a plasma frequency, with  $n_e$  being the free-electron density (of electrons excited to the conduction band), and  $m^*$  is the effective electron mass;  $\tau$  is the relaxation time. The plasma frequency characterizes eigenfrequency of the free-electron gas in response to a small charge separation. So, it corresponds to the electron density oscillation in the conducting media.

The photoabsorption in a semiconductor can be interpreted as a promotion of an electron from the valence to the conduction band. An inverse process of an electron transfer from the conduction to the valence band is also possible. These processes are called interband transitions. Generally, the dielectric function contains a contribution from the Drude response of free carriers and a contribution from interband transitions [28]:

$$\varepsilon(\omega, t) = 1 + 4\pi(\xi_{interband}(\omega) + \xi_{Drude}(\omega)). \quad (2.14)$$

Approaching to the non-equilibrium excitation regime, the applicability of the Drude model is getting even more problematic. At high pump fluences (e.g., above 0.5 kJ/m<sup>2</sup> at  $\hbar\omega = 1.9$  eV for GaAs) the Drude model does not describe changes in the dielectric constant adequately [30] as the excitation causes significant changes in the electronic band structure. Thus, the term  $\xi_{interband}(\omega)$  begins to dominate in the contribution to the optical susceptibility over the term  $\xi_{Drude}(\omega)$  and reflects the response of the CDF to the excitation. It shows the necessity of estimating the interband contribution beyond the Drude model that we perform in Section 4.4. While on longer time scales (below the damage threshold and thermal melting), the Drude model is still capable of producing results close to the experimental ones, on short time scales after the excitation by ultrafast XUV or X-ray pulses, non-thermal effects may play a significant role, and some other modeling approach has to replace the inaccurate Drude model.

## 2.5.2 Ab initio approaches

In physics *ab initio* methods imply calculations from the first principles by employing established laws of nature without any approximations or fitting parameters. However, depending on the community, a term 'ab initio' is sometimes also applied to the methods that partially rely on approximate schemes, for example, to such as the well-known density functional theory (DFT).

DFT is widely used both in solid state physics and quantum chemistry. It has confirmed its potential in defining the electronic band structure in many-body systems. DFT is based on the principle that the ground state of the many-particle system is determined uniquely by the electron density (Hohenberg-Kohn theorem), which can be obtained from a Schrödinger equation [35]. The particle orbitals are defined by Kohn-Sham equations. For the solution of Kohn-Sham equations different basis sets are used [36, 37].

The most simple concept is to use plane waves which are not suitable for quickly varying potentials, unless a very large number of the waves is considered. More advanced approaches use augmented functions. They include, e.g., augmented plane wave (PAW), muffin tin orbital (MTO). These methods are designed to treat the energy dependence of the basis functions. The third type of methods uses localized orbitals, such as, for example, a linear combination of atomic orbitals (LCAO), which is a quantum superposition of atomic orbitals [38].

For studying the properties of many-body systems in non-equilibrium, evolving in the presence of time-dependent potentials, an extension of the conventional DFT, which is called time-dependent density functional theory (TDDFT) was performed. TDDFT relies on Runge-Gross (RG) theorem, which is basically an analogue of the Hohenberg-Kohn theorem for time-dependent systems. RG-theorem governs the relation between the time-dependent many particle state and the corresponding time-dependent density. Analogously to the stationary case, the characteristic Hamiltonian contains the kinetic energy operator  $\hat{T}$ , electron-electron Coulomb interaction energy operator  $\hat{W}$  and the potential energy

operator  $\hat{V}(t)$  of the electrons in the time-dependent potential  $V(\mathbf{r}, t)$  [35, 39]:

$$\hat{H} = \hat{T} + \hat{V}(t) + \hat{W}. \quad (2.15)$$

One of the widely used DFT methods in semiconductors studies is local density approximation (LDA) [35]. The main concept of LDA is to build the exchange-correlation energy  $E_{xc}$  from the exchange-correlation energy per particle  $\epsilon_{xc}$  of the homogeneous electron gas [35, 40]. The dependence on  $\epsilon_{xc}(n)$  can be computed by quantum Monte Carlo scheme. Generally, LDA describes well covalent, metallic and ionic bonds, but works inadequately for hydrogen and Van der Waals bonds.

The exchange-correlation hole  $P_{xc}(\mathbf{r}_1, \mathbf{r}_2)$  is the probability of finding an electron at  $\mathbf{r}_2$  given that there is an electron at  $\mathbf{r}_1$ . It must fulfill the normalization condition to yield exactly one electron. The reason why LDA works is that its accurate prediction of the xc-hole which is reasonably well reproduced in LDA [40]. In turn, the electron-electron interaction depends exclusively on the spherical average of the xc-hole. However, this approach does not work for the excited states and processes beyond Born-Oppenheimer approximation. Also, the calculation of the band gap width for various semiconductors [41] and bonding energies between atoms as a function of distance even for a simple  $H_2$  molecule [42] by LDA disagrees with the experiment.

In general, DFT methods reproduce band structure with a high accuracy. However, due to the high computational costs, they are inappropriate for investigations of highly-excited systems with high time resolution.

Another ab initio approach that can be implemented is based on the Hartree-Fock-Slater (HFS) method and realized, for example, in the XMOLECULE code [43]. It can calculate an electronic structure for molecules irradiated with high intensity X-rays. In this scheme, molecular orbitals are essentially linear combinations of atomic orbitals for molecular core-hole states (the LCAO scheme is employed). The atomic orbitals are calculated with the help of the numerical grid-based method. In such a way, grid parameters and truncation schemes can be iteratively adjusted. The scheme is capable of reproducing the configurations that appear after photoexcitation and removing of electrons from the

ground state, therefore, it can be applied for non-equilibrium dynamics.

In the HFS method molecular orbitals (MO) and orbital energies  $\epsilon_i$  are the result of solving a single-electron Schrödinger equation:

$$\left[ -\frac{1}{2}\nabla^2 + V_{\text{ext}}(\mathbf{r}) + V_H(\mathbf{r}) + V_X(\mathbf{r}) \right] \psi_i(\mathbf{r}) = \epsilon_i \psi_i(\mathbf{r}). \quad (2.16)$$

Here,  $V_{\text{ext}}(\mathbf{r})$  is the external nuclei potential,  $V_H(\mathbf{r})$  is the Hartree potential which describes the Coulomb interaction between the electrons, and  $V_X(\mathbf{r})$  represents the exchange interaction, approximated by the Slater exchange potential for zero temperature [43, 44]:

$$V_X(\mathbf{r}) = -\frac{3}{2} \left[ \frac{3}{\pi} \rho(\mathbf{r}) \right]^{\frac{1}{3}}, \quad (2.17)$$

where  $\rho(\mathbf{r})$  is the electronic density. The presence of the Slater exchange potential distinguishes the Hartree-Fock-Slater method from the Hartree-Fock method. Regarding the exchange potential at a finite temperature, different implementations have been proposed [44], e.g., in [45–47]

### 2.5.3 Tight-binding model

Tight-binding model is a well established semi-empirical method for the band structure computation in solids. The name 'tight-binding' implies that the electrons in the modeled solids are tightly bound to atoms and interact only with the nearest neighbours among all surrounding atoms. This definition already emphasizes the principal difference of the tight-binding model from the Drude model with its free-electron approximation.

The periodicity of atoms in the solid (crystal) can be taken into account in several ways, e.g. by using the dedicated Bloch electron wave functions, which are a good approximation for metals [38]. Otherwise, electrons can be described as slowly moving particles which are 'tightly bound' to a definite atom. Thus, the band structure of the crystal is based on the superposition of the localized wave functions for isolated atoms. This description is relevant for insulators and covalent semiconductors [38].

The formal mathematical basis of the method is a tight-binding Hamiltonian, which can be written as follows [5, 18]:

$$H_{\text{TB}} = \sum_{ij\eta\nu} H_{ij\eta\nu},$$

$$H_{ij\eta\nu} = \epsilon_{i\eta}\delta_{ij}\delta_{\eta\nu} + t_{ij}^{\eta\nu}(1 - \delta_{ij}). \quad (2.18)$$

Here  $i$  and  $j$  stand for the atoms,  $\eta$  and  $\nu$  stand for the atomic orbitals,  $t_{ij}^{\eta\nu}$  is the hopping matrix element, the coefficients  $\epsilon_{i\eta}$  include the on-site energy of atoms. Theoretically, any number of orbitals can be included in the second term of the Hamiltonian. However, in the approach proposed by Slater and Koster  $t_{ij}^{\eta\nu}$  plays rather a role of a set of fitting parameters for the band structure [48]. It is then not a sum or integral over all orbitals. Thus, coefficients  $t_{ij}^{\eta\nu}$  can be used for the interpolation between the energies obtained for definite  $k$ -points from the experiment or ab initio calculations [18]. For many materials, it is sufficient to choose just several orbitals for accurate description of the band structure and other material properties, and an *ansatz*<sup>1</sup> for the form of hopping parameters, which analytical expression may vary. The accuracy of a TB model depends on the particular choice of the set of the basis functions and the accuracy of their fitting.

Usually, tight-binding parameters are adjusted to the ground state of the material. TB is then efficient for band structure calculations in the static regime. However, TB can be also extended for the excited system, which can evolve with changing atomic geometry. This means that hopping parameters must be valid for different structures and such modification of TB is then named *transferable* tight-binding model. The transferable tight-binding approach is efficient in predicting repulsion between the bands which influences the size of the band gap [5]. Apart of this, tight-binding approach can describe accurately enough the chemical bonding, density of states, Fermi energy, and specific electron properties.

---

<sup>1</sup>The word *ansatz* can be translated from German as an assumption about the form of unknown function, which is made in order to facilitate solution of an equation or other problem (Oxford English Dictionary, Addition Series, Volume 3)

# Chapter 3

## Construction of the model

After sorting out the basic physical principles which are crucial to describe FEL excitation of solids and optical photons propagation, here we present the construction of the model based on these principles. As the main goal of the work is the determination of transient optical properties, first, we will discuss the methodology for calculating the complex dielectric function. While CDF is connected with the material band structure, at the second step we will review the XTANT model which allows to calculate it in connection with molecular dynamics calculations. Finally, we will show the predictions of XTANT for optical coefficients in systems under equilibrium.

### 3.1 Calculation of CDF in random phase approximation

In the pump-probe scheme we use optical pulses as probes, and this gives us an opportunity to use a number of approximations, because the response of the material in this case can be reduced with a good accuracy to the contribution of valence electrons only. For the analysis of the dielectric function from the microscopic point of view, we may apply a semi-classical picture, treating electrons quantum mechanically and by treating the external electric field classically. The Hamiltonian for a single electron reads as [28]:

$$H_0 = \frac{\mathbf{p}^2}{2m_e} + V(\mathbf{x}). \quad (3.1)$$

The Lorentz force which governs the motion of the particle in classical electromagnetic field is:

$$F = (-e)[\mathbf{E} + \mathbf{v} \times \mathbf{B}], \quad (3.2)$$

where  $\mathbf{v}$  is a velocity of the electron and  $\mathbf{B}$  is the magnetic field vector, and the both values are dependent on the electric field  $\mathbf{E}$ . It means that we can neglect the quadratic second term. The electron-radiation Hamiltonian then reads as [28]:

$$H_1(t) = +e\mathbf{x} \cdot \mathbf{E}(t) = -\mathbf{\Upsilon} \cdot \mathbf{E}(t). \quad (3.3)$$

Here  $\mathbf{\Upsilon} = -e\mathbf{x}$  is a dipole moment operator. Such an approximation is called the electric dipole approximation as the interaction Hamiltonian  $H_1$  corresponds to the Hamiltonian for a dipole in a static field  $E_0$ . As the electric field is also space-dependent, it is expressed as in Eq. (2.10):

$$\mathbf{E} = \mathbf{E}_0(\omega)e^{i(\mathbf{k}\mathbf{x} - \omega t)}. \quad (3.4)$$

The Fermi wave vector of the crystal lattice is much larger than the wave vector of optical photons. This implies that optical irradiation has a negligible effect on the momentum transfer to the lattice. Then we can expand the  $e^{i\mathbf{k}\mathbf{x}}$  from Eq. (2.10) as

$$e^{i\mathbf{k}\mathbf{x}} \approx 1 + i\mathbf{k} \cdot \mathbf{x} + \dots \quad (3.5)$$

and neglect all the  $\mathbf{k}$ -dependent terms [28]. Such an approximation in condensed matter physics is called the random phase approximation (RPA). For the pump-probe scheme, we can restrict ourselves to the RPA which implies  $\mathbf{q} = |\mathbf{k} - \mathbf{k}'| \rightarrow 0$ , where  $\mathbf{k}$  and  $\mathbf{k}'$  correspond to the crystal momentum in the initial and the final state after the optical transition [27].

The frequency-dependent CDF can be calculated by various DFT schemes. Among them, the methodologies based on, for example, the full-potential linearized augmented plane-wave [49] and the projector-augmented wave methodology [50], were presented. The accuracy of the DFT predictions for the frequency-dependent CDF is usually high. However, the high computational costs make them inappropriate for tracing the materials dynamically under non-equilibrium conditions.

The semi-empirical methods such as tight-binding model, based on a set of localized wave functions, are also able to provide reliable results for non-equilibrium state. As we consider a single frequency of the external field, the random phase approximation can be applied. Within the RPA [51–54] dielectric function can be expressed by a Lindhard formula, based on the first-order perturbation theory [27, 55, 56]:

$$\varepsilon^{\alpha\beta}(\omega) = \delta_{\alpha,\beta} + \frac{e^2 \hbar^2}{m_e^2 \Omega \epsilon_0} \sum_{\eta\nu} \frac{F_{\eta\nu}}{E_{\eta\nu}^2} \frac{f_\nu - f_\eta}{\hbar\omega - E_{\eta\nu} + i\gamma}. \quad (3.6)$$

In this equation  $\Omega$  is the volume of the simulation box;  $E_{\eta\nu} = E_\nu - E_\eta$  is the transition energy between two eigenstates  $|\eta\rangle$  and  $|\nu\rangle$ ,  $f_\eta$  and  $f_\nu$  are the transient occupation numbers of the corresponding states, which are normalized to 2 (taking into account the spin degeneracy);  $m_e$  is the mass of a free electron;  $e$  is the electron charge;  $\hbar$  is the Planck constant; and  $\epsilon_0$  is the vacuum permittivity in SI units. Parameter  $\gamma$  is an inverse electron relaxation time. In our calculations, we use a value  $\gamma = 1.5 \times 10^{13} \text{ s}^{-1}$ . The choice of  $\gamma$  does not affect the results beyond the broadening of peaks in the CDF [57]. Values of  $\gamma$  below  $10^{14} \text{ s}^{-1}$  lead to almost identical peaks in the optical coefficients.  $F_{\eta\nu}$  are the diagonal elements of the oscillator strength matrix and are defined as:

$$F_{\eta\nu} = |\langle \eta | \hat{p} | \nu \rangle|^2, \quad (3.7)$$

where  $\langle \eta | \hat{p} | \nu \rangle$  is a momentum matrix element between the two eigenstates:

$$\langle \eta | \hat{p} | \nu \rangle = \sum_{\mathbf{R}_a \mathbf{R}'_a, \sigma, \sigma'} B_{\sigma\eta}(\mathbf{R}_a) P(\mathbf{R}_a, \mathbf{R}'_a) B_{\sigma'\nu}(\mathbf{R}'_a). \quad (3.8)$$

In Eq. (3.8)  $\mathbf{R}_a$  denotes the coordinates of atoms, and  $\sigma$  labels the atomic orbitals.  $B_{\sigma\eta}$  and  $B_{\sigma'\nu}$  are the corresponding eigenvectors of the Hamiltonian.

Energy levels and occupation numbers are obtained from the calculation of the material band structure at each time step and from the temperature equation in a framework of a semi-empirical self-consistent model, which we will discuss in Section 3.3. On the other hand, the momentum matrix elements can not be obtained if the model does not contain explicit form of the wave functions. In order to extract them, we use the operator identity

$\hat{p} = \frac{m_e}{i\hbar}[\hat{r}, \hat{H}]$ . Thus, the momentum matrix elements can be defined, as in work by Trani et al. [56]:

$$P(\mathbf{R}_a, \mathbf{R}'_a) = \frac{m_e}{i\hbar}[\mathbf{R}_a - \mathbf{R}'_a]H(\mathbf{R}_a, \mathbf{R}'_a), \quad (3.9)$$

where  $H(\mathbf{R}_a, \mathbf{R}'_a)$  is the Hamiltonian matrix.

Average value of the CDF can be calculated from the diagonal elements of the dielectric function tensor:

$$\langle \varepsilon \rangle = \frac{1}{3}(\varepsilon_{xx} + \varepsilon_{yy} + \varepsilon_{zz}). \quad (3.10)$$

The final expressions for the real and imaginary part of CDF, which enter Eq. (2.6), can be written as follows [27]:

$$\begin{aligned} \text{Re}(\varepsilon) &= 1 + \frac{e^2 \hbar^2}{m_e^2 \Omega e_0} \sum_{\eta\nu} \frac{(f_\nu - f_\eta) F_{\eta\nu} (\hbar\omega - E_{\eta\nu})}{E_{\eta\nu}^2 ((\hbar\omega - E_{\eta\nu})^2 + \gamma^2)}, \\ \text{Im}(\varepsilon) &= -\frac{\gamma e^2 \hbar^2}{m_e^2 \Omega e_0} \sum_{\eta\nu} \frac{(f_\nu - f_\eta) F_{\eta\nu}}{E_{\eta\nu}^2 ((\hbar\omega - E_{\eta\nu})^2 + \gamma^2)}. \end{aligned} \quad (3.11)$$

In general case, the calculation of the electronic structure requires a number of different  $k$ -space integrals over the whole Brillouin zone or its irreducible part, obtained by averaging contributions from all  $k$ -points on a mesh in the reciprocal lattice. Hamiltonian in Eq. (3.9) can be replaced by a Fourier transform:

$$H(\mathbf{k}) = \sum_{\mathbf{R}} e^{i\mathbf{k}\cdot\mathbf{R}} H(\mathbf{R}). \quad (3.12)$$

There are different schemes existing of solving such integrals with different choice of 'special points'. One of the most prominent and accurate is Monkhorst-Pack scheme [58] for cubic lattices. Therein, the lattice is defined by three primitive translation vectors  $\mathbf{t}_1$ ,  $\mathbf{t}_2$  and  $\mathbf{t}_3$ , while the associated reciprocal-space vectors can be defined as:

$$\begin{aligned} \mathbf{b}_1 &= \frac{2\pi}{\Omega} \mathbf{t}_2 \times \mathbf{t}_3, \\ \mathbf{b}_2 &= \frac{2\pi}{\Omega} \mathbf{t}_3 \times \mathbf{t}_1, \\ \mathbf{b}_3 &= \frac{2\pi}{\Omega} \mathbf{t}_1 \times \mathbf{t}_2. \end{aligned} \quad (3.13)$$

Here  $\Omega$  is the unit cell volume. For a particular choice of the grid points we define a sequence of numbers [58]:

$$u_r = (2r - q - 1)/2q, \text{ at } r = 1, 2, \dots, q, \quad (3.14)$$

where  $q$  defines the number of special points in the set in one dimension. Thus  $\mathbf{k}$ -vector can be defined as:

$$\mathbf{k}_{\text{prs}} = u_p \mathbf{b}_1 + u_r \mathbf{b}_2 + u_s \mathbf{b}_3. \quad (3.15)$$

Therefore,  $q^3$  points in total can be found in the Brillouin zone.

## 3.2 CDF formalism for inelastic scattering cross sections

The essential part of any numerical treatment of XUV or X-ray irradiated system is an accurate calculation of the total cross sections for the electron impact ionization or excitation of atoms. There are several methods allowing for such calculations and using different collision theories. The quality of the used wave functions is especially important for the accuracy of the model. However, the ab initio calculations of the wave functions, especially for polyatomic molecules, necessary to obtain the ionization cross section, present difficulty. Thus, experimental data and semi-empirical theories are widely used for the purpose. Very often such methods have a good accuracy for high excitation energies but fail to describe the cross section properly at lower energies.

One of the most known models is based on atomic cross sections and is called Binary-Encounter-Bethe (BEB) model. It uses the Mott cross section [59, 60]. This model is used both for cross sections in atoms and in molecules, and it does not contain any empirical parameters. The analytic formula for the total impact ionization cross section per atomic or molecular orbital reads as follows:

$$\sigma_{BEB} = \frac{S}{t + (u + 1)} \left[ \frac{Q \ln t}{2} \left( \frac{1 - 1}{t^2} \right) + (2 - Q) \left( 1 - \frac{1}{t} - \frac{\ln t}{t + 1} \right) \right], \quad (3.16)$$

where  $t = T/b$ ,  $u = U/B$ ,  $S = 4\pi a_0^2 N (R/B)^2$ ,  $a_0 = 0.52918 \text{ \AA}$ , and  $R = 13.6057 \text{ eV}$ . Here  $B$  is the binding energy,  $U$  is the orbital kinetic energy,  $N$  is the electron occupation number,  $Q$  is a dipole constant.

Although the BEB model agrees with many experimental ionization cross sections for a variety of atoms and molecules even at near threshold energies, it may give unreliable results for carbon based materials as shown in [61]. In semiconductors the impact ionization rates are strongly dependent on the band structure, and the electron scattering cross sections are calculated with the usage of time-dependent perturbation expansions.

A quite accurate model for both high and low impact energies was proposed in [62]. An empirical formula proposed there for the mean free path takes into account the asymptotics at low and high energies [62]:

$$\lambda_{ii}(E) = \sqrt{E} / [a(E - E_{th})^b] + [E - E_0 \exp(-B/A)] / [A \ln(E/E_0) + B]. \quad (3.17)$$

Here  $E$  is the electron energy,  $E_0$  is the fitted dimensional coefficient,  $E_{th}$  is the ionization threshold energy;  $a$ ,  $A$  and  $B$  are material dependent constants. The Eq.(3.17) was then fitted to the known data for the impact ionization mean free path for several elements and compounds. Out of that, the total electron impact ionization cross sections can be obtained.

In our work, we implement the complex dielectric function formalism, which calculates the cross section for impact ionization by an electron or another charged particle, and the mean free path of the particle by using the known CDF spectra. It is important to note that the CDF we use here, is an experiment-based CDF fit to the ground-state of the material, and its role is different from the role of the transient CDF, that we defined in Section 3.1. We are not able to use the transient CDF at each time step for the calculation of the cross section because of the computational and functional complexities, as we will demonstrate further. The CDF formalism for inelastic scattering on a system of strongly bound electrons is combined with the Ritchie and Howie method [63]. Within the Born approximation, the cross section for the scattering on a such system reads as in [64, 65]:

$$\frac{d^2\sigma}{d\omega dq} = AS(\omega, \mathbf{q}), \quad A = \frac{m_e^2}{4\pi^2\hbar^5} \frac{k}{k_0} W(\mathbf{q}),$$

$$S(\omega, \mathbf{q}) = \sum_{n_0} p_{n_0} \sum_n \left| \left[ \sum_{j=1}^N \exp(i\mathbf{q}r_j) \right]_{n_0}^n \right|^2 \delta(\omega + (E_{n_0} - E_n)/\hbar). \quad (3.18)$$

In this equation  $\sigma$  is the total cross section for electron scattering,  $A$  is the probability of scattering on an electron,  $S(\omega, q)$  is the dynamic structure factor of electrons. Free-electron mass is denoted  $m_e$ ,  $k_0$  and  $k$  are the initial and final momentum vectors of the electron,  $r_j$  is the position vector of each of  $N$  particles within the scattering system, the initial and final states of this system are signed as  $n_0$  and  $n$  correspondingly, and  $E_{n_0}$  and  $E_n$  are their respective energies. Finally,  $p_{n_0}$  is the statistical weight of the initial state.

The link between the structure factor  $S(\omega, \mathbf{q})$  and the macroscopic dielectric function  $\varepsilon(\omega, \mathbf{q})$  is provided by the fluctuation-dissipation theorem [64, 66]:

$$S(\omega, \mathbf{q}) = \frac{\mathbf{q}^2}{4\pi^2 n_e} \text{Im} \left( \frac{1}{\varepsilon(\omega, \mathbf{q})} \right), \quad (3.19)$$

where  $n_e$  is the electron density. The cross section for scattering on a system of electrons within the Born approximation can be written as [64, 66]:

$$\frac{d^2\sigma}{d\omega dq} = \frac{2(Z_e e)^2}{\pi \hbar^2 \nu^2} \frac{1}{\mathbf{q}} \text{Im} \left( \frac{-1}{\varepsilon(\omega, \mathbf{q})} \right). \quad (3.20)$$

$Z_e$  is the effective charge of a particle in the electronic system, while  $e$  is the electron charge,  $\nu$  is the velocity of the incident particle. The mean free path is connected with the cross section as  $\lambda = \frac{1}{n_e \sigma}$ .

The algorithm, invented by Ritchie and Howie, constructs the approximated dielectric function from the experimentally available data on photon scattering in solids. The CDF parametrization in this method is the Drude-type fit for an ensemble of atomic oscillators, which contain three sets of adjustable coefficients [63, 64]:

$$\text{Im} \left[ \frac{-1}{\varepsilon(\omega, q=0)} \right] = \sum_i \frac{A_i \gamma_i \hbar \omega}{(\hbar^2 \omega^2 - E_{0i}^2)^2 + (\gamma_i \hbar \omega)^2}. \quad (3.21)$$

The coefficient  $E_{0i}$  is the characteristic energy of the oscillator  $i$ , the coefficient  $A_i$  is the fraction of electrons that have the specific energy  $E_{0i}$ , and  $\gamma_i$  is the  $i$ th energy damping coefficient. The summation is performed over all oscillators  $i$ .

The dipole approximation,  $q = 0$ , is assumed in the model, implying the absence of the momentum transfer for massless photons. By fitting the model functions from the Eq. (3.21) to the data, the missing coefficients can be obtained. The experimental data on

optical properties can be represented either by  $n$  and  $k$  refraction indices (typically for low photon energies below 30 eV) or by the attenuation coefficients for higher energies. The imaginary part of inverse CDF looks like [64, 67]:

$$\text{Im} \left[ \frac{-1}{\varepsilon(\omega, q=0)} \right] = \frac{c}{\lambda_{ph}\omega}, \quad (3.22)$$

where  $\lambda_{ph}$  is the mean free path till absorption, and  $c$  is the speed of light in vacuum. During the implementation, the quality of the fitting should be checked with the specific sum rules. First, *ps*-sum-rule (perfect screening sum rule) [63, 64, 67]:

$$P_{\text{eff}} = \frac{2}{\pi} \int_0^{\hbar\omega_{\text{max}}} \text{Im} \left[ \frac{-1}{\varepsilon(\omega, q=0)} \right] \frac{d(\hbar\omega)}{\hbar\omega}. \quad (3.23)$$

If  $\hbar\omega$  goes to infinity, the value of  $P_{\text{eff}}$  must tend to 1. The second rule is called the *f*-sum-rule [63, 64, 67]:

$$Z_{\text{eff}} = \frac{2}{\pi\Omega_p^2} \int_0^{\omega_{\text{max}}} \text{Im} \left[ \frac{-1}{\varepsilon(\omega, q=0)} \right] \omega d\omega, \quad (3.24)$$

where  $\Omega_p^2 = (4\pi n_m e^2 / m_e)^{1/2}$  is the plasma frequency and  $n_m$  is the density of molecules in the solid under consideration. If  $\hbar\omega_{\text{max}}$  tends to infinity, the  $Z_{\text{eff}}$  must tend to the total number of electrons per molecule of a target. Finally, in order to extend the approximation from the dipole limit  $q=0$  to massive particles (electrons), one should replace the coefficients  $E_{0i}$  by the expressions  $(E_{0i} + (\hbar q)^2 / (2m_e))$  [63, 64].

The cross section calculations with Ritchie and Howie method are based on the first Born approximation, so it should be implemented only for high-energy electrons. The estimations made in [68] show that the lower limit for electron energies, which can provide reliable results, is  $\sim 10$  eV. For lower electron energies, quantum effects of the band structure must be taken into account. The specific parameters entering into the model functions used for the determination of the inverse CDF in Eq. (3.21) are collected in Appendix D.

### 3.3 XTANT model

In order to study transient states of matter, a unified hybrid model XTANT was developed [5] by N. Medvedev. It traces both transient electronic excitation and the evolution of atomic structure and combines transferable tight-binding (TB) formalism, classical molecular dynamics (MD), Boltzmann equation and Monte Carlo scheme in a self-consistent manner. XTANT enables to calculate such parameters as a band gap width, potential and kinetic energies of atoms and electrons, their temperature and chemical potential, as well as optical coefficients, which are known to be sensitive experimental observables. The calculation of optical properties is based on the tight-binding approach and complex dielectric function (CDF) formalism in random phase approximation (RPA). A schematic picture of this model is shown in Fig. 3.1.

The core of the hybrid model is the semi-empirical transferable tight-binding scheme, which calculates the time evolved potential energy surface and the band structure of the material. In the previous Chapter, we discussed in detail the advantages of the TB model and its usefulness to describe the excited states of semiconductors. The atomic Hamiltonian looks as follows:

$$H = H_{\text{TB}} + E_{\text{rep}}(\{r_{ij}\}), H_{\text{TB}} = \sum_{ij\eta\nu} H_{ij\eta\nu},$$

$$H_{ij\eta\nu} = \epsilon_{i\eta}\delta_{ij}\delta_{\eta\nu} + t_{ij}^{\eta\nu}(1 - \delta_{ij}). \quad (3.25)$$

The Hamiltonian consists of two parts: the attractive tight-binding Hamiltonian  $H_{\text{TB}}$ , which has a form as in Eq. (2.18), and the repulsive term  $E_{\text{rep}}(\{r_{ij}\})$  which describes the repulsion of atomic cores. With this Hamiltonian we can calculate electronic energy levels  $E_i$  at every time. Then, knowing the occupation numbers, the potential energy surface  $\Phi(\{r_{i,j}\}, t)$  can be calculated. The hopping integrals  $t_{ij}$  are calculated with Slater and Koster approach [5, 48].

Slater and Koster approach is a parameterized tight-binding method based on the two-center approximation. The two-center approximation implies that overlap terms and Hamiltonian  $H_{\text{TB}}$  matrix elements include orbitals and potentials of only two atomic sites

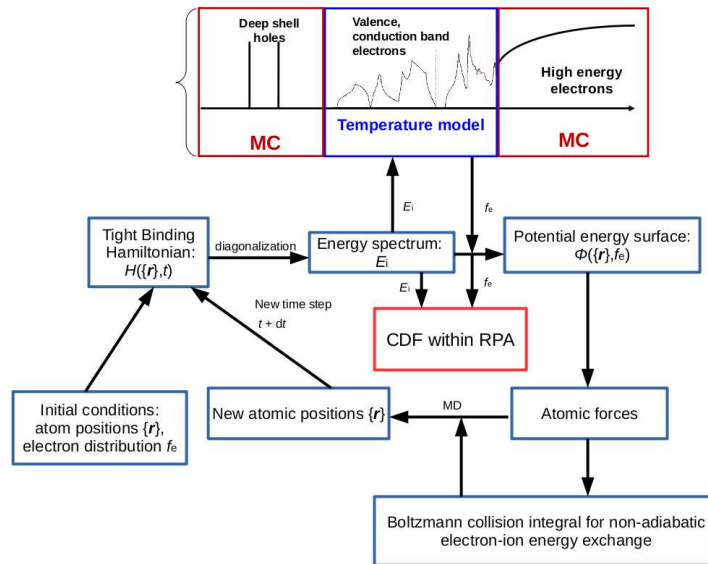


**Figure 3.1:** Schematic picture of the hybrid XTANT model realization. The high-energy electrons and deep shell holes are traced with MC method; the low-energy electrons are treated with temperature equation; MD technique is used for the calculations on atoms; the tight-binding approach is used for the definition of the potential energy surface and the electron band structure. The picture is partly adopted from [5].

$i$  and  $j$ . This approximation is valid for the off-diagonal Hamiltonian matrix elements. The involved potential  $V(r - R_n)$  accounts for all atoms in the system. Utilizing the assumption, that the atomic orbitals are orthogonal Wannier functions, the Hamiltonian can be written in a parameterized two-center form. Due to this fact, the dependence of the hopping integral on the distance can be expressed analytically. For carbon and silicon, this method takes into account only s,  $p_x$ ,  $p_y$  and  $p_z$  valence orbitals, which is enough for the accurate description of band structure in these materials. As we will deal with structural transformations, we use transferable tight-binding hopping integrals, which have to be functions of positions of all atoms in the simulation box.

The angular parametrization proposed by Slater and Koster looks as follows [48]:

$$\begin{aligned}
t_{ij}^{ss} &= V_{ss\sigma}, \\
t_{ij}^{sp_x} &= l_{ij}V_{sp\sigma}, \\
t_{ij}^{p_x p_y} &= l_{ij}m_{ij}(V_{pp\sigma} - V_{pp\pi}), \\
t_{ij}^{p_x p_z} &= l_{ij}n_{ij}(V_{pp\sigma} - V_{pp\pi}), \\
t_{ij}^{p_x p_x} &= l_{ij}^2V_{pp\sigma} + (1 - l_{ij}^2)V_{pp\pi},
\end{aligned} \tag{3.26}$$

where  $l_{ij}$ ,  $m_{ij}$ ,  $n_{ij}$  represent the cosines between the directions of the position vectors for the atoms  $i$  and  $j$ :

$$l_{ij} = \frac{r_{ij,1}}{r_{ij}}, m_{ij} = \frac{r_{ij,2}}{r_{ij}}, n_{ij} = \frac{r_{ij,3}}{r_{ij}}. \tag{3.27}$$

The distances between the atoms in directions  $x$ ,  $y$ ,  $z$  are calculated as:

$$\begin{aligned}
r_{ijx} &= x_i - x_j, \\
r_{ijy} &= y_i - y_j, \\
r_{ijz} &= z_i - z_j.
\end{aligned} \tag{3.28}$$

Together with periodic boundary conditions, the distances will be:

$$r_{ij\alpha} = \sum_{\beta} h_{\alpha\beta}(s_{i\beta} - s_{j\beta} + z_{\beta}), \alpha, \beta \in \{1, 2, 3\}. \tag{3.29}$$

All other hopping terms  $t_{ij}$  can be written analogously to Eq. (3.26). The transferability of the tight-binding method is determined namely by the distance-dependent functions  $V_\xi$  ( $\xi = \{ss\sigma, sp\sigma, pp\sigma, pp\pi\}$ ). Their form was proposed by Pettifor et al [18, 69]. The dependence on the interatomic distance for each pair of atoms within the box and from the neighbouring supercells is described by fitting functions as well as a repulsive potential energy:

$$\begin{aligned}
 V_\xi(r_{ij}) &= V_\xi^0 \left(\frac{r_0}{r_{ij}}\right)^n \exp \left[ n \left( -\left(\frac{r_{ij}}{r_c}\right)^{n_c} + \left(\frac{r_0}{r_c}\right)^{n_c} \right) \right], \\
 E_{\text{rep}}(\{r_{ij}\}) &= \sum_i F \left( \sum_j \phi(r_{ij}) \right), \\
 F(x) &= a_0 + a_1x + a_2x^2 + a_3x^3 + a_4x^4, \\
 \phi(r_{ij}) &= \phi_0 \left(\frac{r_0}{r_{ij}}\right)^m \exp \left[ m \left( -\left(\frac{r_{ij}}{d_c}\right)^{m_c} + \left(\frac{r_0}{d_c}\right)^{m_c} \right) \right].
 \end{aligned} \tag{3.30}$$

Here, the coefficient  $V_\xi^0$  characterizes the dependence of the hopping integral on the interatomic distance  $r_{ij}$ ,  $r_0$  is the nearest neighbour distance. The distance dependence is fixed by the exponent  $n$ ,  $r_c$  denotes the cut-off radius,  $n_c$  determines the range of hopping. The parameters  $m$ ,  $d_c$  and  $m_c$  analogously define the distance dependence of the repulsive potential,  $d_0$  scales the distances. The functional  $f$  for the repulsive potential includes coefficient from  $a_0$  to  $a_4$ . [18]. The electronic energy levels  $E_i$  are acquired by the diagonalization of the Hamiltonian matrix  $H_{\text{TB}}$ . The potential energy surface is thus defined by the occupation numbers  $f_e(E_i, t)$ , energy levels  $E_i$  and the repulsive potential energy  $E_{\text{rep}}$ :

$$\Phi(\{r_{ij}\}, t) = \sum_i f_e(E_i, t)E_i + E_{\text{rep}}(\{r_{ij}\}). \tag{3.31}$$

Such calculation of the potential energy surface implies using the Ehrenfest-like dynamics, the applicability of which for our case is explained in Appendix B. The particular form and values of the tight-binding parameters of carbon and silicon are given in Appendix C.

The tight-binding methodology for GaAs that we use was proposed by Molteni et al. in 1994 [70]. It is based on the fitting of the cohesion energy curves of a few crystalline phases to the results of the ab initio calculations. In order to keep the transferability of the method, the cohesive-energy phase diagram must be reproduced in three different phases

at zero temperature. Here, the Slater-Koster tight-binding Hamiltonian is used again with the orthogonalized, extended  $sp^3s^*$  set. For the crystalline phases, where all the bonds have the same length  $r$ , the total energy per atom can be written as in [70]:

$$E_{\text{tot}} = 2 \sum_i f_e(E_i) E_i + \frac{N_{nn}}{2} U(r), \quad (3.32)$$

where  $U(r)$  is a phenomenological pair potential,  $N_{nn}$  is the coordination number and the spin degeneracy is taken into account.

The scaling law for the fitting parameters has to be modified to enable to reproduce different ab initio calculations. The expression from Eq. (3.32) can be rewritten with a scaling function  $s(r)$  as follows:

$$E_{\text{tot}}[s(r)] = E_{\text{bs}}[s^2(r)] + N_{nn} \Phi(s(r))^m, \quad (3.33)$$

where  $E_{\text{bs}}$  is a band structure energy. To obtain the scaling law of the hopping term, the  $s(r)$  function is squared. In order to adjust the equilibrium volumes, a new scaling function  $s_2(r)$  is introduced, similarly to the Eq. (3.30) above:

$$s_2(r) = \frac{r_0}{r} \exp \left[ - \left( \frac{r}{r_c} \right)^{n_c} + \left( \frac{r}{r_c} \right)^{n_c} \right], \quad (3.34)$$

where  $r_c$  and  $n_c$  are parameters of the smoothed step function that represent the position and the sharpness of the step, respectively. The repulsive energy can be expressed as a sum of the pair potential. With the Harrison scaling rule [71] and the Born-Mayer potential [72], responsible for the overlap of the occupied orbitals, the interatomic distance-dependent term is added:

$$U(r) = \Phi_1 \exp[-(r - r_0)/\alpha] + \Phi_2 \left( \frac{r_0}{r} \right). \quad (3.35)$$

With the additional term  $\Phi_2 \left( \frac{r_0}{r} \right)$ , charge-transfer effects are approximately taken into account. The total set of TB parameters for GaAs is listed in Appendix C.

The atomic motion is traced by using the classical molecular dynamics (MD) technique. In [61] the applicability of the classical MD method towards highly single-ionized strongly bound systems with a large number of atoms was analyzed. The conclusion was that even

for such systems the classical MD gives results in a good agreement with the experimental data, while some discrepancy comes from the treatment of impact ionization cross sections. In our model, the forces between atoms are calculated with the help of semi-empirical tight-binding method which is essentially a basis of the XTANT model [5, 18].

As the number of atoms in the excited volume of the bulk is very high, a straightforward MD calculation is not possible. Thus, periodic boundary conditions have to be applied to a simulation box chosen within the laser spot and containing a few tens to a thousand of atoms [5]. The increase in the number of atoms in the simulation box slows down the calculation time, but at the same time it diminishes the statistical fluctuations of the values.

The two options for the periodic boundary conditions, implemented with the Parrinello-Rahman method, are included into XTANT: simulations with the constant volume ( $\Omega = \text{const}$ ) or with the constant pressure ( $P = \text{const}$ ). If the constant volume is chosen, then the simulation corresponds to the solution of the classical Newtonian equation of atomic motion. Otherwise, the Lagrangian of the supercell motion takes into account the changes of the geometry of the supercell. Thus, the external pressure can be fixed, while we allow the supercell volume to change, e.g., to expand due to heating [5]:

$$L = \sum_{i=1}^N \frac{M_i}{2} \dot{\mathbf{s}}_i^{\mathbf{T}} h^{\mathbf{T}} h \dot{\mathbf{s}}_i - \Phi(\{r_{ij}\}, t) + \frac{W_{PR}}{2} \text{Tr}(\dot{h}^{\mathbf{T}} \dot{h}) - P_{\text{ext}} \Omega, \quad \mathbf{r}_i = h(\mathbf{s}_i + \mathbf{z}). \quad (3.36)$$

The two first terms in the equation describe the atomic motion, and the two last ones describe the kinetics of the supercell. Here  $M_i$  is the atomic mass,  $\mathbf{r}_i$  is the coordinate of the atom  $i$ ,  $\mathbf{s}_i$  are the relative coordinates of the atoms within the simulation box, vectors  $\mathbf{z}$  are responsible for the periodic boundaries. The matrix  $h$  is constructed out of the three dimensional vectors  $\mathbf{a}$ ,  $\mathbf{b}$  and  $\mathbf{c}$ , that span the MD supercell [5, 18, 73]. By choosing linearly independent dimensional vectors, adjusting their lengths and orientations, the space can be filled with the repeated supercells formed by the vectors. Further,  $\Phi$  is the potential energy surface, the constant  $W_{PR}$  is the effective mass of the supercell. The last term was proposed by Parrinello and Raman to describe the external pressure on the supercell  $P_{\text{ext}}$

(atmospheric pressure in the standard case). The volume  $\Omega$  is the transient volume of the simulation box [5]. In case of simulations with the constant volume the last two terms will not enter the Lagrangian. The molecular dynamics modeling with constant pressure on the supercell yields larger numerical uncertainty than the MD simulations with a constant volume of the supercell, because in case of the constant volume apart from oscillations of atoms the volume supercell oscillates as well [5, 18]. The Verlet algorithm is used here to follow the time evolution of the atomic coordinates and velocities (for details see Appendix A) [5, 18, 74].

One of the key points of XTANT is a division of all electrons in the system into two fractions: low-energy and high-energy electrons. The chosen cut-off energy is initially equal to 10 eV, which is broader than a band gap width in semiconductors considered here. Low-energy electron system which is close to the equilibrium is treated with the Boltzmann equation for homogeneous systems [21, 75]:

$$\frac{df_e(E_i)}{dt} = I_{e-e} + I_{e-i}, \quad (3.37)$$

where  $f_e(E_i)$  is the transient electron distribution or an occupation number on the energy level  $E_i$ ,  $I_{e-e}$  is the electron-electron collision integral,  $I_{e-i}$  is the electron-ion collision integral. In our model, we use a more general electron-ion scattering picture instead of the electron-phonon coupling for electron-lattice thermalization. We assume that any atomic displacement from the equilibrium position induces changes in the population of the energy levels, and the excess energy is transferred to the atoms of the crystal lattice. In a phononic approach the interatomic potential is parabolically approximated to write the Hamiltonian as a set of harmonical oscillators, also the ideal crystal is assumed and the time scales are assumed to be long enough to treat collective motion of atoms [33, 76]. None of these assumptions is valid in case of strong electronic excitation on a femtosecond time scale [76]. The particular electron-ion coupling schemes and corresponding forms of the electron-ion collision terms are discussed in Subsection 4.3.3.

The instantaneous electron thermalization is assumed, meaning infinitely fast electron-electron scattering. The low-energy electrons are then assumed to form a Fermi-Dirac

distribution which describes a distribution of fermions in a system in a thermodynamical equilibrium. At each time step, the total number of low-energy electrons is calculated. It consists of the number of the electrons excited by the incoming photons of the laser pulse and the number of electrons removed from the high-energy electron fraction due to the secondary collisions. If the energy of the electron overcomes the cut-off, it joins the high-energy domain, and vice-versa, a sufficient loss of energy may lead a high-energy electron to fall into the low-energy domain. The total energy of all electrons in the system is conserved. Knowing it, the potential and kinetic energy of atoms can be calculated as well.

The temperature  $T_e$  and the chemical potential  $\mu_e$  of the low-energy electron subsystem can be found from Fermi-Dirac distribution by solving the inverse problem [5]. The factor 2 accounts for the electron spin. The values of chemical potential and temperature are calculated at each time step from the known values of the electron numbers and their energies:

$$\begin{aligned} N_e^{low} &= \sum_{E_{min}}^{E_{cut}} f_e(E_i) = \sum_{E_{min}}^{E_{cut}} \frac{2}{1 + \exp((E_i - \mu)/T_e)}, \\ E_e^{low} &= \sum_{E_{min}}^{E_{cut}} E_i f_e(E_i) = \sum_{E_{min}}^{E_{cut}} \frac{2E_i}{1 + \exp((E_i - \mu)/T_e)}. \end{aligned} \quad (3.38)$$

As shown in Eq. (3.31), the transient electronic distribution  $f_e(E_i, t)$  influences the potential energy surface from which atomic forces and new atomic positions can be determined. Then, the new tight-binding Hamiltonian is recalculated at every time step, and the new energy spectrum  $\{E_i\}$  is constructed.

The number of high-energy electrons is relatively low, therefore, together with the deep shell holes, they are treated individually with the asymptotic trajectory Monte Carlo scheme [77] event-by-event. The photoabsorption by the electron, secondary impact ionization by the electron, elastic scattering of electrons on ion target, elastic scattering of two free electrons and Auger processes involving free electrons and deep shell holes can be described with such a scheme. The calculation of inelastic scattering cross sections is based on the complex dielectric function formalism, and was discussed in detail in the previous

Section.

Now, let us discuss the limitations of our model. First, we assume that each photon excites only one electron which is a reliable approximation for XUV photons [27], as the probability of two-photon absorption at such energy range is approximately two orders of magnitude lower than the probability of one-photon absorption. Therefore, the fluences above  $50 \text{ J/cm}^2$  required for two-photon absorption cannot be considered in XTANT.

In our approach, the relocation of electrons to the high-energy domain naturally decreases their number in the low-energy domain. The attractive part of the inter-atomic potential is then lowered, and an effective charge non-neutrality is created. In case of high fluence irradiation, creating large electron density in the conduction band and large hole density in the valence band, a changed inter-atomic potential causes atomic displacement which may lead to Coulomb explosion of the affected part of the system [5]. The examples can be found, e.g. for finite systems (clusters) in [78, 79]. The Coulomb repulsion of ions can break the interatomic bonds, and the cluster fragmentizes or explodes. Generally, this restriction makes the theoretical scheme unapplicable for high irradiation fluences, when the number of high-energy electrons is relatively large. Analogously, we assume that the core-holes density should be relatively low comparing to the total electron density.

The tight-binding predetermined parameters are adjusted to the ground state and are not able to reproduce the electronic structure of highly excited systems. This limitation requires more universal *ab initio* techniques, such as HFS approach discussed above, and they could be included into the hybrid model as it has a modulous structure. For example, an *ab initio* model could produce potential energy surfaces and the corresponding forces, replacing the tight-binding. In Chapter 5 we discuss our efforts towards such implementation.

Let us emphasize again that tight-binding is a well established approach, especially in structural calculations of semiconductors. Comparing to many DFT methods, the tight-binding approach is computationally efficient. In principle, by adopting new sets of parameters and functional dependencies a noticeable variety of different materials, including compounds can be described. On the other hand, every new parametrization requires a

separate programming module, which is not convenient from the implementational point of view. In contrast, the DFT methods, in general, are more flexible towards the input material parameters.

### 3.4 Optical coefficients in equilibrium

First of all, we test our model for the frequency-dependent CDF in equilibrium materials. Only after such benchmarking the model, we may move to the analysis of non-equilibrium states. In the current version of XTANT, the spectrum of frequency-dependent optical parameters linked with CDF can be calculated for three materials: diamond, silicon and gallium arsenide. For instance, we may construct spectra of  $n(\omega)$  and  $k(\omega)$  refractive indices and compare them to the known experimental data [80].

Fig. 3.2 shows that for the energies below  $\sim 7$  eV, the agreement between the experimental data for diamond and XTANT predictions is good. However, at higher energies, the agreement is getting worse, and the broad peak at 12 eV is not described by XTANT. This is due to the fact that the TB model in XTANT describes only valence and the bottom of the conduction band, not accounting for high-lying states in the conduction band. But as long as optical irradiation is used for probing, the model accuracy achieved for the optical wavelengths is sufficient.

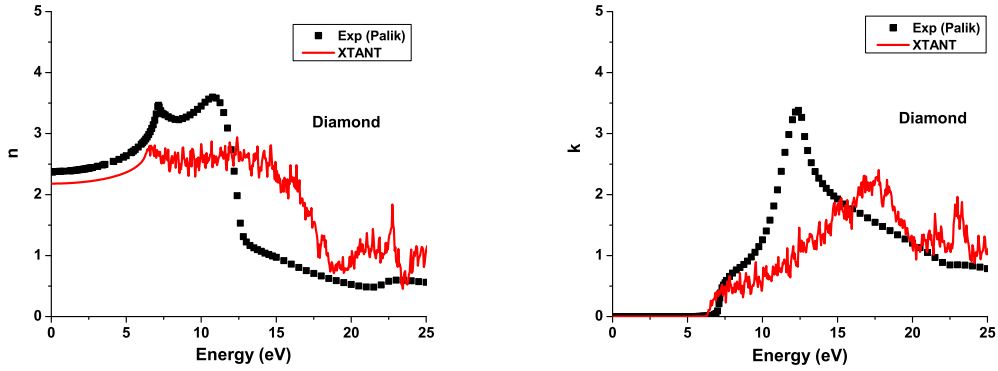


**Figure 3.2:** Optical refractive indices  $n(\omega)$  and  $k(\omega)$  of the equilibrium diamond. The dots are experimental data [80]; the solid line is XTANT prediction with TB model obtained, using 2197  $k$ -points.

The dependence of the spectra on the number of  $k$ -points and the number of atoms in the simulation box has been analyzed. An increase of both parameters diminishes statistical oscillations. However, an increase of only the number of atoms does not sufficiently improve the accuracy, as it is more sensitive to the number of  $k$ -points. The simulated results converge for the number of points greater than  $\sim 2000$ .

The spectra obtained for silicon show agreement for energies up to  $\sim 2$  eV (see Fig. 3.3), which is still sufficient for the description of pump-probe experiments with optical pulses. The convergence of spectra is reached with around 2000  $k$ -points.

This lower energy limit for silicon is caused by a more narrow band gap width. In both diamond and silicon maximal energies, under which the agreement is achieved, approximately correspond to band gap width values ( $\sim 6$  eV for diamond and  $\sim 1.1$  eV for silicon). As in case of diamond, the sharp peaks for  $n(\omega)$  and  $k(\omega)$  are also missing for silicon. An agreement with experiment at optical wavelengths for diamond and silicon is observed even with  $\Gamma$ -point (center of the Brillouin zone) calculation of the CDF, i.e. if  $\mathbf{k} = 0$ . Thus, we can perform simulations of optical coefficients at the  $\Gamma$ -point for these materials, in this way reducing the costs of the calculations, unless the values of other analyzed parameters demonstrate strong numerical oscillations.

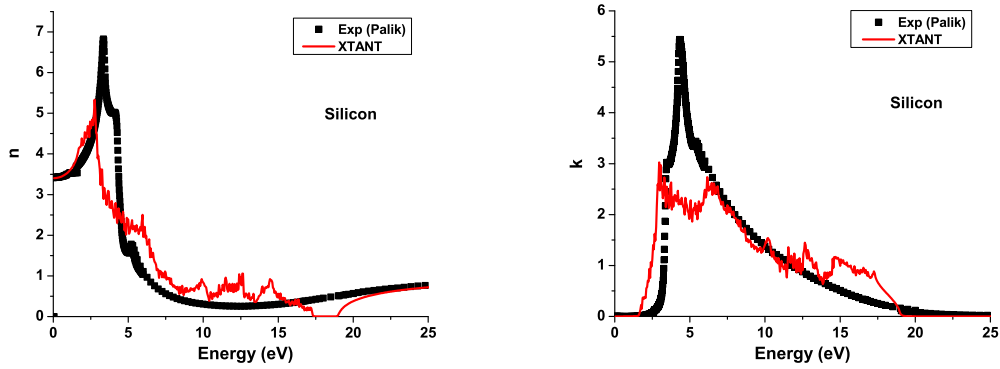


**Figure 3.3:** Optical refractive indices  $n(\omega)$  and  $k(\omega)$  of the equilibrium silicon. The dots are experimental data [80]; the solid line is XTANT prediction with TB model obtained, using 2197  $k$ -points

The last predictions were made for gallium arsenide (see Fig. 3.4). In this case the agreement is worse due to the complexity of the band structure of the material. The  $\Gamma$ -point calculation, even at optical energies, is insufficient for the description of the CDF in GaAs. Many  $k$ -points are needed to reach a reasonable agreement with the experimental data.

Out of all performed comparisons, we may conclude that the TB-based model is, in general, appropriate for the definition of CDF within optically irradiated materials. In order to investigate CDF at higher energies, an ab initio model is needed. Another option can be the application of TB model with a different set of fitted parameters. For instance, in Trani's work, the parameters from [81, 82] were used in TB, and they gave a better accuracy for silicon, reproducing the main peak on the curve. However, the crucial point of our research is studying CDF in non-equilibrium materials which may experience phase transitions. Thus, for these goals we need to apply a well established transferable tight-binding method, which is valid for changing structure of the material.

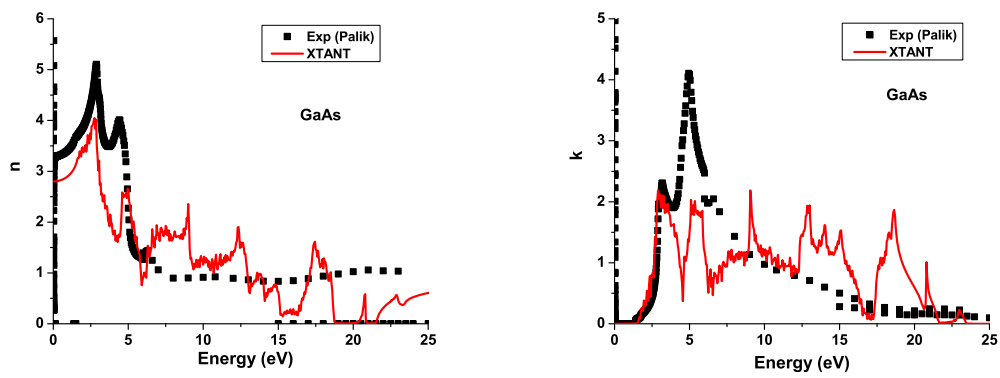


**Figure 3.4:** Optical refractive indices  $n(\omega)$  and  $k(\omega)$  of the equilibrium GaAs. The dots are experimental data [80]; the solid line is XTANT prediction with TB model obtained, using 2197  $k$ -points.

# Chapter 4

## Non-equilibrium dynamics of FEL irradiated solids

### 4.1 Phase transitions

In thermodynamics a phase transition is defined as a transition of matter from one thermodynamical phase to another under the change of external conditions like temperature or pressure. By looking at temperature-pressure phase diagrams of many materials, one may notice that they have many possible phases, so the phase transitions are not only transitions from one state of matter to another, like, e.g., from solid to liquid or from liquid to gas transitions, but also transitions within one state of matter (e.g., solid-to-solid).

The classification of phase transitions was proposed by Paul Ehrenfest [83]. He divided all of them into the phase transitions of the first order and phase transitions of the second order. The order here means the order of the derivative of thermodynamical potentials ( $F, G, \mu..$ ) over temperature or pressure in which this derivative exhibits discontinuity. The first-order transitions may happen between different states of matter (solid to liquid or gas to liquid) and also within one state of matter (disorder to order in solids). Such a phase transition always involves a latent heating  $L$  as it is determined by the rapid change of entropy  $S$ , as  $L = T\Delta S$  [84]. The second-order phase transitions have no latent heating

because the entropy (the first derivative of the Gibbs free energy  $G$ ) does not show any discontinuity. The examples of the second-order phase transitions are transitions of metals and alloys to superconductive state or transition of the liquid helium to superfluid state.

However, the picture of phase transitions given by Ehrenfest is incomplete as it uses thermodynamical approximation for systems with a large number of particles whose thermodynamic parameters are established [84, 85]. The striking example of the transition for which this approximation breaks down is a laser-induced non-equilibrium ultrafast phase transition [5, 86]. The change of interatomic potential which is the reason of the phase transition is caused by an electron excitation occurring on a femtosecond time scale when the phonon subsystem is not yet involved, and there is no thermal equilibrium between electrons and lattice.

The modern concept of thermodynamics proposed in [85] then distinguishes first-order phase transitions with latent heat and all other transitions without latent heat. Out of that, we conclude that, e.g., thermal (phonon-mediated) melting of silicon and GaAs can be referred to as the first-order phase transitions. At the same time non-thermal melting of silicon and ultrafast graphitization of diamond (due to radiation-triggered electron excitation) are examples of the first-order phase transitions either, as they go through absorption of the internal energy by the electronic subsystem on a very short time scale in terms of conventional thermodynamics.

## 4.2 Diamond

After establishing the validity of the TB-based model, we may start the analysis of the evolution of the optical parameters in irradiated materials. We begin our study with diamond. Diamond is a solid state form of carbon, its metastable allotrope. It has a face-centered cubic crystal lattice. Natural diamonds can be found in Earth's crust - they are formed under conditions of high temperature and pressure in deeper layers (Earth's mantle) and then brought to the surface through volcanic eruptions [87]. Several artificial types of diamond can be formed from graphite which undergoes temperature and pressure

exposure. Such technologies are known since long time [88, 89]. However, it can also be formed at low pressures as a metastable carbon phase [90, 91]. Diamond is widely applied in industry due to its exceptionally high hardness [92], thermal conductivity [92] and reflectance [93]. These properties make diamond a perfect material for usage in various optical systems, e.g., monochromators, refractive lenses and mirrors. With contemporary development of X-ray lasers diamond components are finding their application in X-ray diffractive optics. Therefore, any interaction of X-ray photons with diamond structures is very important from this perspective. For example, heating of diamond below melting temperature may cause sufficient changes in its diffractive properties [94]. One could expect that non-thermal damaging will cause changes in optical properties of diamond. Concerning its electric conductivity, unexcited diamond has a band gap of  $\sim 6$  eV, which places it between insulators and broad band semiconductors.

Phase diagram of carbon (Fig. 4.1) shows that with the increasing temperature, metastable diamond under atmospheric pressure converts into graphite, the stable structure of carbon [95]. However, in what follows, we will present the case in which the temperature increase is a consequence of a non-thermal transition of diamond to energetically favorable state of overdensed graphite due to the change of the interatomic potential.

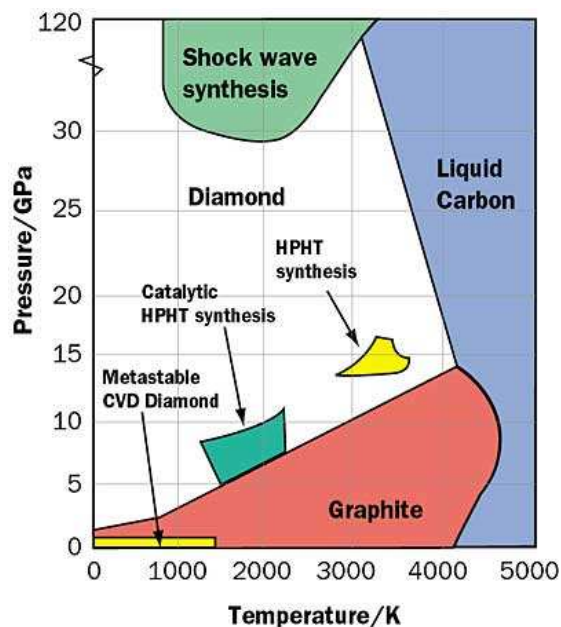


**Figure 4.1:** Basic phase diagram of carbon. The picture is taken from *www.electronics-cooling.com*.

### 4.2.1 Irradiation of diamond below and above graphitization threshold

Now we will perform the simulations to distinguish the cases when diamond is irradiated below the non-thermal graphitization threshold and above it to see how this affects its optical properties. For illustration, we will consider here a case with realistic pulse parameters which can be achieved with existing XUV FEL lasers. Let us then consider that diamond is irradiated with the 90 fs long Gaussian FEL single pulse which has the photon energy of 50 eV. In [86], it is shown that XUV and soft X-ray femtosecond laser pulses of any energy below the carbon K-edge ( $\hbar\omega = 285$  eV) may cause graphitization, and the graphitization process is more fluence-dependent than photon energy-dependent. At photon energies above the K-edge an additional impact to the non-equilibrium dynamics is given by photoexcitation of core level electrons and the consequent secondary processes, such as Auger-decay, and then such energies were not in focus of [86]. However, these

processes can be accounted by XTANT.

We also specify the constant volume of the supercell, and initial room temperature ( $T_0 = 300$  K) of electrons and atoms. The optical probe pulse, which is needed for the definition of optical properties, has a wavelength of 600 nm (photon energy  $\hbar\omega = 2.07$  eV) and arrives at the normal incidence to the diamond sample. We choose 216 atoms in the supercell ( $3 \times 3 \times 3$ ), as the simulations performed with 64 atoms in the box may be affected by statistical oscillations. On the other hand, simulations with 512 atoms in the supercell do not show any crucial difference of results when compared to 216 atoms case, but tend to be much more time-consuming [27]. As it was stated in Chapter 3, optical properties of diamond at optical probe wavelengths should be represented accurately enough at  $\Gamma$ -point approximation, which we will use here. The FEL pulse in our simulations is centered at zero on a time scale.

While keeping all these parameters unchanged, we vary the absorbed dose  $D_{\text{abs}}$  specified in eV/atom. It is tightly related to the pulse fluence  $F$  (in [J/cm<sup>2</sup>]) as:

$$D_{\text{abs}} = 6.24 \cdot 10^{18} \cdot F \cdot \left[ 1 - \exp\left(-\frac{d}{\lambda_{\text{att}}}\right) \right] \cdot \frac{M}{N_A \rho d N}, \quad (4.1)$$

where  $d$  [cm] is the thickness of the investigated sample,  $\lambda_{\text{att}}$  [cm] is an X-ray attenuation length for a given photon energy and material,  $M$  is a molar mass [g/mol] of the chemical elements or compounds forming the material,  $\rho$  is the material density [g/cm<sup>3</sup>],  $N$  is a number of atoms in a molecule, and  $N_A$  is the Avogadro number [mol<sup>-1</sup>]. If we consider a bulk material, we can assume that  $d = \lambda_{\text{att}}$  and most of the dose will be absorbed within the attenuation-length-thick layer. We can then rewrite Eq. (4.1) as:

$$D_{\text{abs}} = 3.94 \cdot 10^{18} \cdot F \cdot \frac{M}{N_A \rho \lambda_{\text{att}} N}. \quad (4.2)$$

A theoretically and experimentally established threshold dose which causes non-thermal graphitization of the diamond bulk is  $\sim 0.7$  eV/atom [5, 86] which is near its damage threshold ( $\sim 1$  eV/atom) [18, 96] and far below its ablation threshold ( $\sim 4$  eV/atom) [18, 97], depending on the X-ray pulse duration. The doses around this threshold will be studied below.

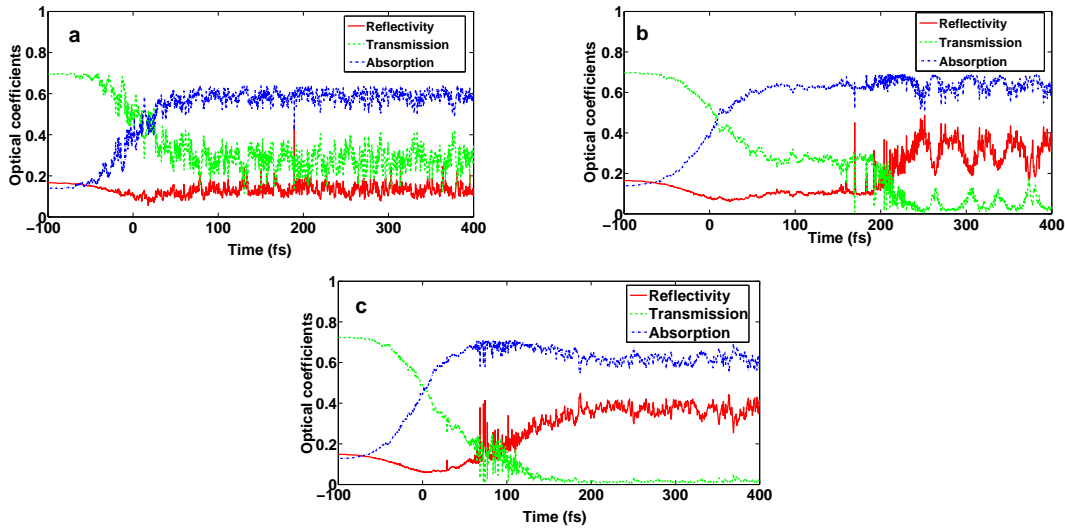


**Figure 4.2:** XTANT-modelled optical coefficients of diamond at different radiation doses absorbed: (a) 0.6 eV/atom, (b) 0.8 eV/atom and (c) 1.0 eV/atom. Solid red lines depict reflectivity coefficients, the dashed green lines are transmission coefficients, the dot-dashed blue lines show absorption coefficients. The FEL pulse energy  $\hbar\omega = 50$  eV, the pulse duration  $\tau = 90$  fs, the probe pulse wavelength  $\lambda = 600$  nm.

We start our simulation set with a dose of 0.6 eV/atom. This is below the graphitization threshold, but still sufficient to cause electronic excitation, which does not lead to significant atomic relocations. Material thickness is assumed to be  $d = \lambda_{\text{att}} = 100$  nm [27]. The transmission coefficient decreases from the initial value of  $\sim 0.7$  to  $\sim 0.3$ , never fully dropping to zero (Fig. 4.2). The absorption significantly rises up, while the reflectivity is slightly affected. On longer time scales ( $> 1$  ps) the optical coefficients must return to their original values. However, due to the use of periodic boundary conditions, our model does not include energy transport and carrier diffusion effect. As the result, we are not able to model this relaxation process here directly [27].

The simulation for the dose of 0.8 eV/atom (slightly above the damage threshold) yields the full decrease of the transmission coefficient to zero on a time scale of about 100 fs. The reflectivity coefficient rises up. This was not observed in case of the below threshold dose. The optical transmission decreases in two stages - first, it drops to an intermediate value

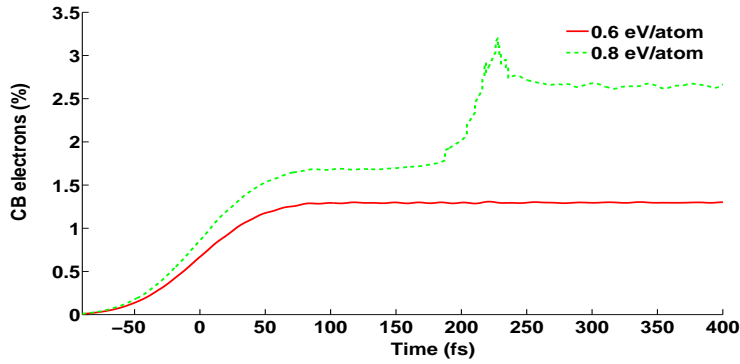


**Figure 4.3:** Relative number of the electrons in diamond excited to the conduction band (both in low- and high-energy domain) in respect to the total number of electrons in the system. For the absorbed dose of 0.6 eV/atom dose (solid red line), this ratio does not reach 1.5 %, while for the 0.8 eV/atom dose (dashed green line) it rises up to 1.5 %. After a plateau, it shows a sharp rise (peak).

(around 0.2 in represented case) in  $\sim 100$  fs after the pulse maximum, forming a plateau on the curve, and then finally decreases to zero within additional 100 fs. Such a complete vanishing of the transmission is a signature of graphitization of diamond, as graphite is optically intransparent material.

This behaviour can be explained with a detailed look at the stages of non-equilibrium dynamics. First, diamond absorbs energy from the photons of an incident laser pulse, and transmission coefficient begins to decrease because of the excitation of electrons from the valence to the conduction band. During the first  $\sim 50$  fs, the electronic band structure, as well as the atomic structure, remains practically unchanged. Only if the fraction of the conduction band electrons reaches a certain value ( $\sim 1.5\%$  of valence band electrons for diamond [5]) (Fig. 4.3), than the electronic band structure undergoes significant changes, including the band gap collapse. This leads to the relocation of atoms to new positions, that correspond to the graphite structure. As it takes some time for atoms to relax into a new equilibrium state, it explains the occurrence of the transient plateau on the transmission curve [98].

For the absorbed dose of 1.0 eV/atom, which is significantly above the damage thresh-

old, the transmission coefficient decreases directly to zero after  $\sim 100$  fs, without an intermediate plateau. This is due to the faster band gap collapse at the higher dose. In general, for all three cases, the decrease in transmittance corresponds to a decrease of the real part  $\text{Re}(\varepsilon)$  of CDF and a peak in the imaginary part  $\text{Im}(\varepsilon)$  of CDF (Fig. 4.4). The real part of the CDF gains eventually values around zero at  $t > 200$  fs in case of 0.8 eV/atom and 1.0 eV/atom absorbed doses, that corresponds to the CDF of graphite at optical wavelengths. The full spectrum of the CDF in carbon irradiated above graphitization threshold at 400 fs is represented in Fig. 4.4. It is compared with experimental data for the average CDF in graphite ( $\langle \varepsilon \rangle = \frac{2}{3}\varepsilon_{\perp} + \frac{1}{3}\varepsilon_{\parallel}$ ) from [99] and the experimental data for equilibrium diamond [80]. As graphite has a hexagonal crystal system, it can be characterized by two dielectric functions  $\varepsilon_{\perp}$  and  $\varepsilon_{\parallel}$  [80, 99], associated with the electric-field vector  $\mathbf{E}$  which is partly perpendicular ( $\varepsilon_{\perp}$ ) and partly parallel ( $\varepsilon_{\parallel}$ ) to the symmetry axis of the crystal ( $c$ -axis). The absorption spectra of the carbon state obtained after irradiation with dose over graphitization threshold are much closer to the spectra of the equilibrium graphite, rather than to diamond. However, due to the overdensified state [5] of such graphitized diamond and an inaccuracy of the TB model, the experimentally measured spectra of graphite and of graphitized diamond are still not in a perfect agreement.

Band gap shrinking promotes additional electrons to the conduction band. As a result, potential energy surface changes. The  $sp^3$  bonds of the cubic diamond break down and  $sp^2$  bonds of graphite start to form. We can trace the dynamics of the system by using VMD program<sup>1</sup>, which creates the snapshots of atomic positions at different time instants. (Fig. 4.5). The transformation of the cubic structure of diamond into individual parallel planes of graphite is clearly visible, and the vanishing of the transmission coincides with the occurrence of graphitization.

For quantitative interpretation of these snapshots, we apply the pair correlation function of carbon atoms at the same time instants. In thermodynamics and statistical physics, a

---

<sup>1</sup>VMD (Visual Molecular Dynamics) is a product of the University of Illinois, 'a molecular visualization program for displaying, animating, and analyzing large biomolecular systems using 3-D graphics and built-in scripting' (citation from <http://www.ks.uiuc.edu/Research/vmd/>)

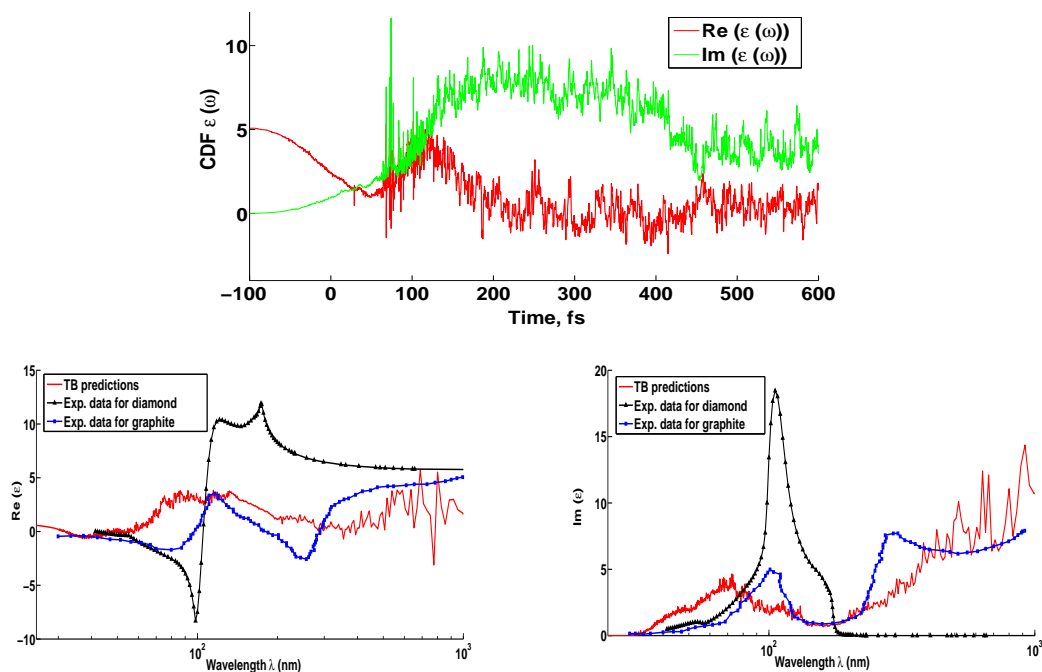


**Figure 4.4:** Time dependence of complex dielectric function in diamond irradiated with 50 eV FEL pulse, at 0.8 eV/atom absorbed dose (top); real (left, bottom) and imaginary (right, bottom) part of the complex dielectric function of equilibrium graphite (blue curves with squares) [99] and equilibrium diamond [80] (black curves with triangles) measured experimentally and of simulated graphitizing diamond (bold red line) at 400 fs after the FEL pulse. The absorbed dose is 0.8 eV per atom.

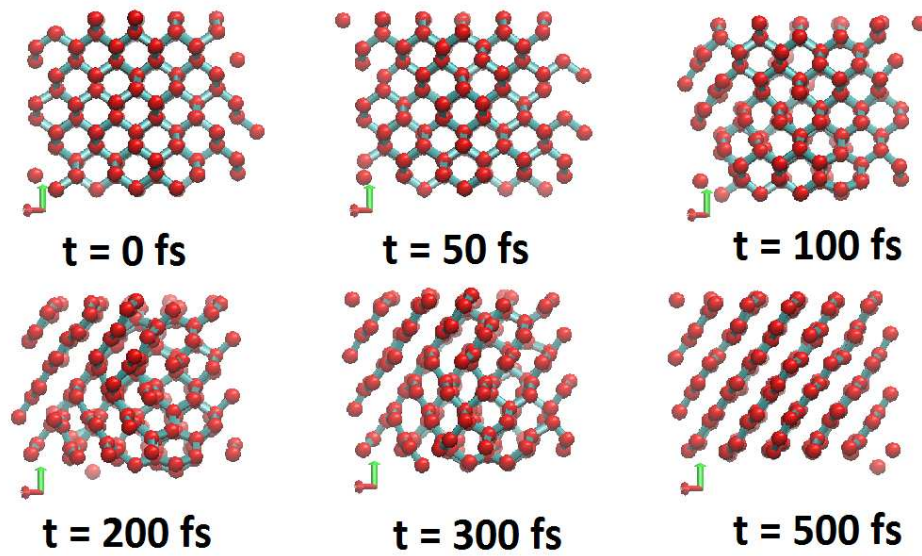


**Figure 4.5:** Snapshots of atomic positions in the irradiated diamond supercell at different time instants: 0 fs, 50 fs, 100 fs, 200 fs, 300 fs, 500 fs. The absorbed dose was 1.0 eV/atom,  $\hbar\omega = 50$  eV, pulse duration  $\tau = 90$  fs. Pulse maximum is at  $t = 0$  fs.

pair correlation function  $g(r)$  defines the probability to find one particle at a distance  $r$  from another particle within a certain system of particles. Let us define a system with  $N$  particles in a volume  $\Omega$ . The coordinates of the particles are  $(\mathbf{r}_1 \dots \mathbf{r}_N)$ , their temperature  $T$  and the potential energy of interaction between the particles:  $U(\mathbf{r}_1 \dots \mathbf{r}_N)$ . The configuration integral  $Z_N$  then describes all possible configurations of the system of particles in the canonical ensemble  $(N, \Omega, T)$ :

$$Z_N = \int \dots \int \exp\left(-\frac{U_N}{kT}\right) dr_1 \dots dr_N. \quad (4.3)$$

Then, the correlation function  $g^{(n)}(\mathbf{r}_1, \dots, \mathbf{r}_n)$  for  $n$  fixed particles, where  $n < N$  takes the form:

$$g^{(n)}(\mathbf{r}_1, \dots, \mathbf{r}_n) = \frac{\Omega^N N!}{N^n (N-n)!} \cdot \frac{1}{Z_N} \int \dots \int \exp\left(\frac{-U_N}{kT}\right) dr_{n+1} \dots dr_N. \quad (4.4)$$

The pair correlation function  $g^{(2)}(\mathbf{r}_1, \mathbf{r}_2)$  which depends only on the relative distance  $\mathbf{r}_{12} = \mathbf{r}_2 - \mathbf{r}_1$  can be determined as a particular case of Eq. (4.4), applying the ensemble average:

$$g(\mathbf{r}) = \Omega \frac{N-1}{N} \langle \delta(\mathbf{r} - \mathbf{r}_1) \rangle. \quad (4.5)$$

In Fig. 4.6, at  $t = 0$  fs one can see the peak in the pair correlation function of carbon at 1.53 Å which corresponds to the nearest-neighbour distance in diamond under the room temperature [5]. After graphitization, the peak shifts to 1.41 Å – the nearest-neighbour distance between atoms in graphite [5].

In order to claim that the abrupt changes of optical properties are explicitly connected with the phase transition, we also analyze other parameters calculated with XTANT. As it was said before, the entire atomic rearrangement happens due to the band gap shrinking. The band gap width decreases from the initial value of above 6 eV finally to zero. The steep decrease matches the start of the graphitization process (Fig. 4.7) in case of 1.0 eV/atom dose. The band gap shrinking typically occurs earlier than the graphitization because of the atomic relaxation into the new equilibrium state, which may take 50-100 fs on average. For the below threshold dose of 0.6 eV/atom, the average band gap width almost does not change after the pulse.

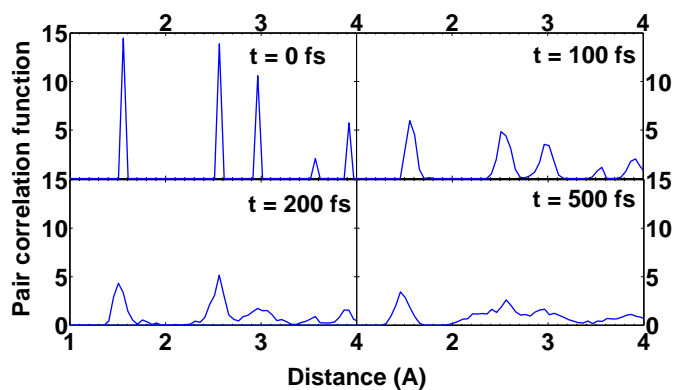


**Figure 4.6:** Pair correlation function of the carbon atoms which absorbed 1.0 eV dose at the following time instants: 1) 0 fs (before irradiation); 2) 100 fs; 3) 200 fs; 4) 500 fs (after the phase transition is completed).

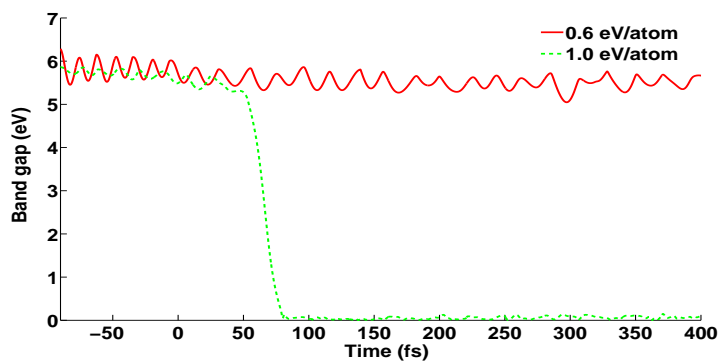


**Figure 4.7:** Band gap of diamond after irradiation with laser pulse at the absorbed dose of 0.6 eV/atom (solid red line) and 1.0 eV/atom (dashed green line), pulse energy  $\hbar\omega = 50$  eV, pulse duration  $\tau = 90$  fs.

Another important material property is the optical conductivity  $\sigma(\omega)$  which links the electric field and the current density:

$$\mathbf{J}(\omega) = \sigma(\omega)\mathbf{E}(\omega). \quad (4.6)$$

Following this definition, optical conductivity is connected to the dielectric function  $\varepsilon(\omega)$ :

$$\varepsilon(\omega) = \varepsilon_0 + i\frac{4\pi\sigma(\omega)}{\omega}. \quad (4.7)$$

Since the band gap is interconnected with the frequency dependent optical conductivity, it has an onset frequency that characterizes the interband electron transition [27]. The optical conductivity can be measured during the experiment (see e.g. [100–102]). In such a way the progress of the band gap shrinking and of a phase transition itself can be traced. Knowing the time and frequency dependent complex dielectric function values, we can also estimate an optical conductivity spectrum at different instants of time (Fig. 4.8). In unexcited diamond optical conductivity has non-zero values starting from the edge of a band gap as it can be expected from theory (Fig. 4.8, blue curve). After  $t = 70$  fs when the graphitization process is already advanced, we can observe that the first peak in the spectrum corresponds to the collapsing band gap value (Fig. 4.8, orange curve). When the sample is fully graphitized (Fig. 4.8, purple curve), there is no signature of a non-zero band gap, as it should be expected in semimetallic graphite. Since the optical conductivity can be measured in experiments, in such a way dynamics of the band gap shrinkage and thus the phase transition itself can be traced unambiguously.

Another, though less illustrative, signature of the phase transition and atomic relocation is the behaviour of the potential energy of the atoms. As it can be seen in the Fig. 4.9, shortly after the pulse (with above threshold dose delivered to atoms), the potential energy of atoms begins to oscillate exchanging with the kinetic energy of the moving atoms. Occurrence of this effect for the above threshold dose can be observed on a time scale corresponding to the transmission decrease. It is clearly seen that the oscillations in Fig. 4.9b are stronger and the average potential energy decreases as the phase transitions is going on. In Fig. 4.9a these oscillations are weak and the average potential energy does not change.

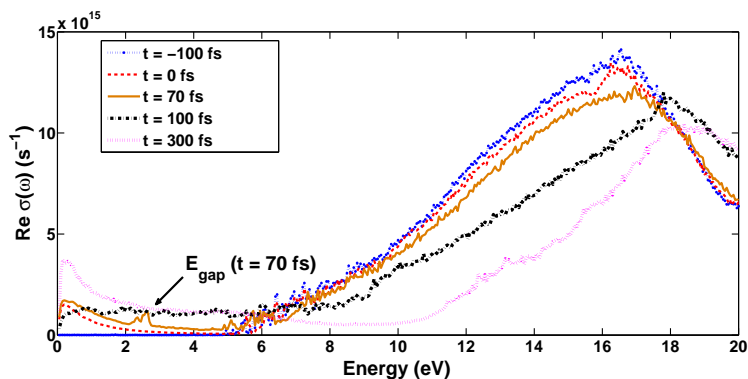


**Figure 4.8:** Frequency-dependent optical conductivity spectrum in diamond (graphite) at various time instants during graphitization:  $t = -100, 0, 70, 100, 300$  fs. The FEL pulse energy  $\hbar\omega = 50$  eV, the pulse duration  $\tau = 90$  fs, absorbed dose = 1.0 eV/atom.

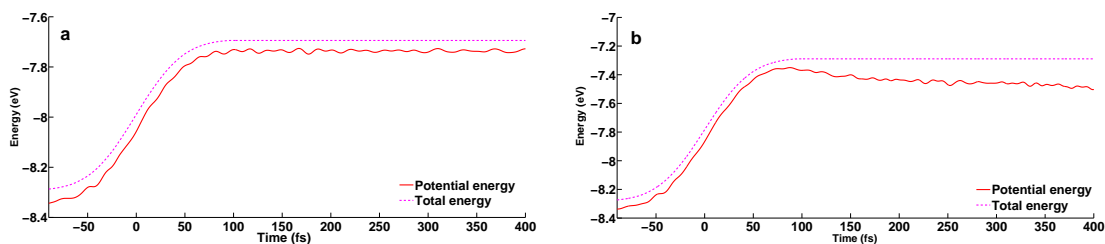


**Figure 4.9:** Potential energy of atoms (solid red line) and the total energy of the system (magenta dashed line) in diamond: a) irradiated below (at 0.6 eV/atom absorbed dose per atom) the graphitization threshold, b) irradiated above (at 1.0 eV absorbed dose per atom) the graphitization threshold.

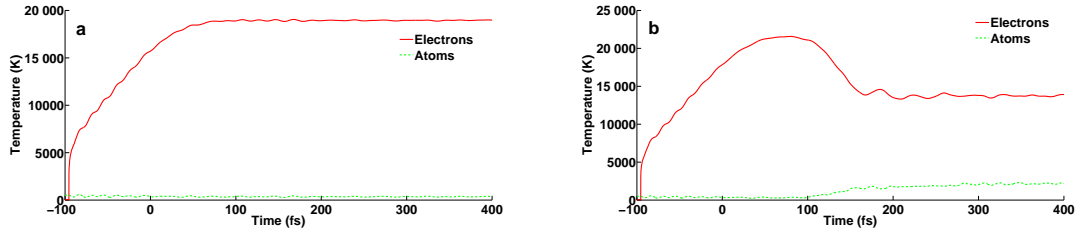


**Figure 4.10:** Transient electronic (solid red line) and atomic (dashed green line) temperatures in diamond: a) irradiated below the graphitization threshold at 0.6 eV/atom absorbed dose, b) irradiated above the graphitization threshold at 1.0 eV/atom absorbed dose.

The behaviour of the atomic and electronic transient temperatures also deserves attention. In Fig. 4.10b we observe that after the arrival of high fluence pulse, the low-energy electron temperature strongly increases up to the peak value within a few tens of femtoseconds when the electrons are promoted to the conduction band, and then it starts decreasing, whereas at the fluence below the threshold level (Fig. 4.10a), the temperature reaches a smaller value and then remains stable (unless diffusion processes start to play a role). The lattice temperature fluctuates, following the oscillation of kinetic energy. Before the end of the pulse it almost does not change, but then it raises rapidly (Fig. 4.10b). This corresponds to the decrease of the potential energy of the atoms. The final temperature of the lattice corresponds to the graphitization temperature (equivalent to the lattice temperature, sufficient for the thermal graphitization of diamond [95]), and the increase of the temperature up to this value occurs during the phase transition, that we can follow on the snapshots from Fig. 4.5. The increase of the temperature is a consequence of the phase transition, but not a reason. This is a characteristic feature of a non-thermal transition. If graphitization does not occur, the lattice temperature practically does not change (Fig. 4.10a).

We are able to vary pulse and sample parameters in our supercell and estimate their influence on the values of optical properties. It was found out that the FEL pulse duration  $\tau$  does not significantly affect the non-equilibrium evolution of the system and, consequently, the values of optical properties. If a diffusion effect is not taken into account, the graphiti-

zation threshold dose is not sensitive to the pulse duration either. As shorter pulses deliver the same amount of energy and dose faster, the saturation of electrons in the conduction band up to the critical density, band gap shrinking and graphitization will also occur faster. For pulses with  $\tau < 20$  fs the different pulse duration should not contribute to the changes of the time scale of non-equilibrium processes, as the minimal time to reach the threshold density of the excited electrons is  $t \sim 20$  fs at photon energies below 2 keV [103]. The influence of the FEL pulse shape was also analyzed on examples of the rectangular pulse, Gaussian pulse and a SASE pulse [103]. All observable parameters proved themselves to be practically unaffected by the pulse shape. The tiny difference was only observed in the slope of the total energy decrease at the beginning of pulse propagation, which follows the pulse temporal shape [103].

The analysis of the dependence of graphitization progress on the FEL photon energy was also performed. Such criteria as the ratio of the conduction band electrons (1.5%) needed for band gap shrinking does not change for FEL energies in a range from a few tens of eV to a few tens of keV [20, 86]. The graphitization threshold dose of 0.7 eV/atom corresponds to this value and it also remains the same even in the region above the K-edge of diamond, although the transient electron kinetics in this case is different. More energetic photons from the FEL pulse produce photoionized electrons with higher energies and, thus, subsequently, the number of secondary ionization events is higher. As a result, the photoelectrons lose their energy below the high-energy cut-off and thermalize slower, which leads to a slower phase transition. Therefore, for hard X-rays graphitization can be significantly delayed in time [103].

To summarize, we got a number of convincing evidences that the changes of optical properties in irradiated carbon are tightly connected with ultrafast damage processes progressing within the material. The solid-to-solid and order-to-order phase transition from diamond to graphite can be detected, as the equilibrium optical properties of both of these carbon phases are well known, and the observed change of the transient optical properties indicates diamond-to-graphite transition. In next Subsections we will compare our results with the experimental ones to check the accuracy of our model and to validate its

theoretical basis.

### 4.2.2 Effect of non-equilibrium electron kinetics on optical properties

In previous Subsection we saw that the changes of optical properties in carbon correlated, on the one hand, with the microscopic changes in the electronic subsystem (rise of the conduction band and high-energy electron number, rise of the electronic temperature), and, on the other hand, with the changes in the atomic subsystem (decrease of the potential energy of atoms, changes in the atomic pair-correlation function). Naturally, all these changes are parts of one unified process, but the question arises: what has the more impact on optical coefficients - electrons or atoms? What is the trigger of the changes?

Thus, we study here how the changes in optical coefficients are connected with the phase transition and atomic relocations by artificial decoupling of electron excitation and atomic dynamics within the model. We 'switch off' the transient atomic dynamics by 'freezing' the atoms, i.e., their positions remain fixed during the simulation. In such a way, we can estimate the exclusive contribution of FEL excited electrons to the optical properties [98]. The preliminary assumption that electron kinetics with unaffected band structure predominantly determines the evolution of optical properties can be checked.

Fig. 4.11 shows that even for the above-threshold dose of 1.0 eV/atom, the optical coefficients do not change after the pulse propagation and electron cascades. This is in contrast with the predictions from Fig. 4.2c. This indicates clearly that the impact of structural transformation within the material on optical coefficients is much more significant than the contribution from electronic excitation. Therefore, it explains why the models that do not take into account the effect of atomic structure, such as, e.g., Drude model, are not able to produce reliable predictions of optical properties in the materials under femtosecond X-ray irradiation at the new above damage threshold doses.

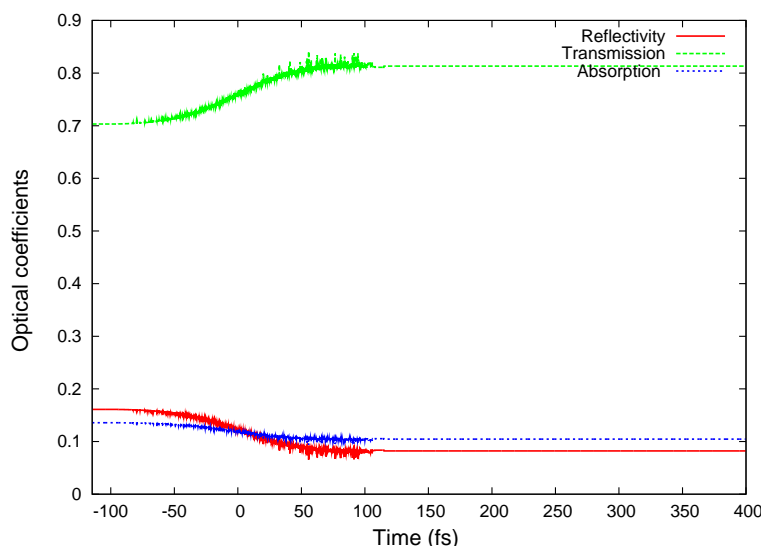


**Figure 4.11:** Optical reflectivity (solid red line), transmission (dashed green line) and absorption (dot-dashed blue line) coefficients of diamond with 'frozen atoms and active electrons' (as in Drude model) irradiated by FEL pulse with photon energy  $\hbar\omega = 50$  eV, pulse duration  $\tau = 90$  fs. The absorbed dose is 1.0 eV/atom.

### 4.2.3 Optically induced radiation damage in diamond

We now present the comparison of our results with the available experimental data. Due to the constant improvement of FEL facilities in the recent years and opening the new ones, the number of experiments with FELs is increasing rapidly. However, strict requirements on the time resolution and pulse fluences hindered so far preparation of experiments on X-ray FEL-induced diamond graphitization. Only within the last couple of years, such an experiment could be performed at the FERMI@Elettra facility. It will be discussed in the next Subsection.

Here, we make a qualitative comparison of our predictions with the results of an experiment in which optical pumping was used. As it was mentioned above, XTANT code is not capable of modelling optical pulses directly. It assumes solely single-photon absorption, thus being limited to energies above  $\sim 30$  eV [27]. Also, soft X-ray pulses induce fast electron cascading and their fast relaxation. In Fig. 4.12 the relative number of the excited

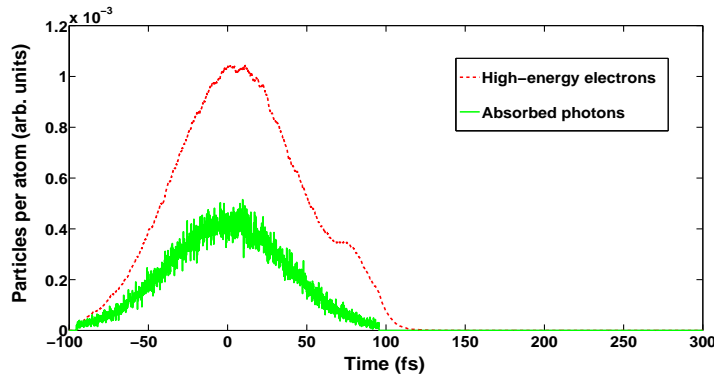


**Figure 4.12:** The number of high-energy electrons (with energies above 10 eV) and the absorbed photons in excited diamond (in arbitrary units). FEL photon energy  $\hbar\omega = 50$  eV, pulse duration  $\tau = 90$  fs, absorbed dose = 1.0 eV/atom.

high-energy electrons is plotted. Already during the pulse propagation, it decreases drastically and shortly after the pulse the electronic dynamics in the system becomes equivalent to that one in the case of optical pumping. Therefore, approximate modeling of the pump pulse with photon energy in XUV range is not expected to produce much different results, when compared to a direct optical pulse modelling.

In the work by Reitze et al. [96] transient reflectivity of diamond IIa type<sup>2</sup> (100) and graphite for the optical probe pulses was measured above the critical melting fluences  $F_m$  with the resolution up to 100 fs. For diamond, the probe was incident at the angle of  $\sim 20^\circ$  to avoid the back surface reflection and leaving only the front surface reflection. The pump and probe pulses had the same duration of 90 fs and wavelength of 620 nm. For comparison, we consider a set of measurements with the absorbed optical fluence 9 times higher than the  $F_m$  fluence [96], which approximately corresponds to the absorbed dose of 6.3 eV/atom. The highest time resolution was used for such fluence. Such high irradiation led to ultrafast thermal melting of diamond to a liquid phase equivalent to a liquid phase formed after graphite melting with the same fluence [96].

The agreement between the TB-based theory and experiment can be seen in Fig. 4.13. A discrepancy during the pulse can be explained by a contribution from a small fraction

---

<sup>2</sup>Rare type of diamond, which does not contain measurable nitrogen and boron impurities.

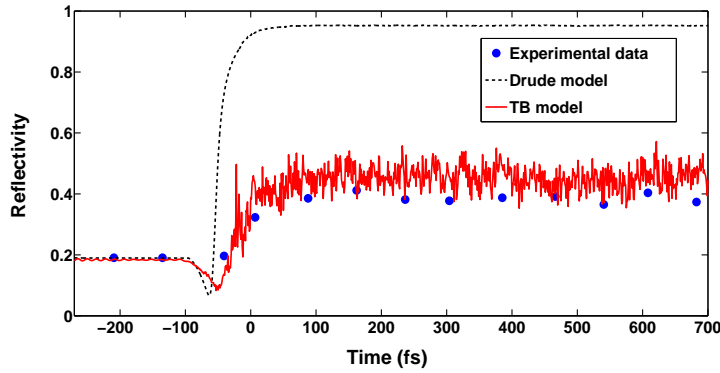


**Figure 4.13:** Reflectivity coefficient of diamond irradiated with the absorbed dose of 6.3 eV/atom. Probe pulse of 620 nm wavelength, 90 fs duration and angle of incidence of  $20^\circ$  is used. The pump is normally incident, of  $\lambda = 620$  nm wavelength, and  $\tau = 90$  fs duration. The dots are experimental data [96], the solid line represents the TB calculations, the dashed line represents the results predicted by the Drude model.

of the remaining high-energy electrons. The results obtained with the Drude model with fixed relaxation time and electron-hole masses are also shown for the illustration. The Drude model fails to predict the reflectivity in case of the over-threshold excitation, as it does not take into account interband transitions and the changing electronic and atomic structure of the material.

In order to test the applicability of the Drude model to calculate the optical properties in FEL-irradiated diamond, we compared the curves obtained with the Drude model to the curves obtained with the TB-model for different absorbed doses. It turns out that at the absorbed doses larger than  $\sim 0.1$  eV/atom (see Fig. 4.14) a disagreement between the results from two models can be observed. The Drude model is then capable of reproducing the electron contribution into the optical properties accurately.

Drude model with the constant values of electron-hole masses and scattering times is still often applied for interpretation of experimental results on transmission and reflection changes during pump-probe experiments, e.g., in [75, 104]. Essentially, Fig. 4.11 with optical coefficients obtained in the 'artificial frozen-electrons' case, analyzed before, shows that the Drude model results follow closely the TB-model calculations in this regime. This

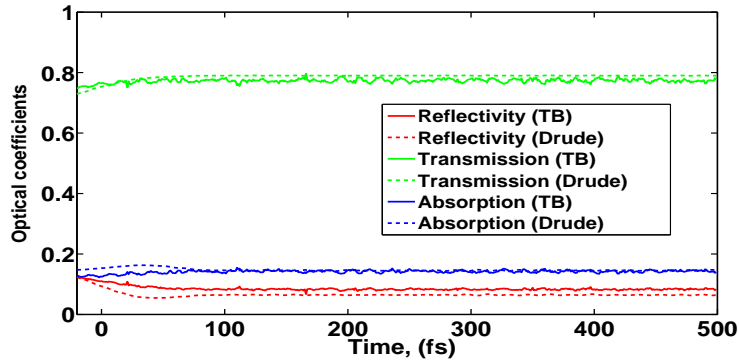


**Figure 4.14:** Transient optical coefficients (reflectivity (red lines), transmission (green lines), absorption (blue lines)) of diamond irradiated at the absorbed dose of 0.1 eV/atom, obtained with the tight-binding model (solid lines) and Drude model (dashed lines).

shows that the Drude model can be employed for tracing changes in optical properties induced solely by electron excitation, and it breaks down as soon as atomic contribution becomes non-negligible. Simply speaking, Drude model can be reliable approach for fluences far below the damage threshold.

#### 4.2.4 Measured X-ray induced graphitization of diamond

In general, transformations from diamond to graphite structure are known for a long time. In such experiments high temperature [105], annealing [106] or high pressure [107, 108] were used. Forming of graphite was observed both on the surface and within the bulk.

In the previous Subsection, the experiment by Reitze et al. on irradiation of diamond above the damage threshold was discussed. However, this experiment and another experiment by Sokolowski-Tinten et al. with silicon [109], which we will discuss in Subsection 4.3.2, were performed by using optical irradiation in a pump-probe scheme. The related simulations showed that the XTANT code is able to describe time evolution of optical properties in the materials with good accuracy, albeit being limited to the XUV photon energies [27, 98]. In these experiments only a reflectivity coefficient of the materials was measured. The transmission coefficient is more sensitive to the ongoing transformation in

diamond, as it was discussed before.

Recent experiments performed with XUV and soft X-rays are described in [86]. First, the SPring-8 facility in Japan was used for generating 24 eV photon energy pulses and second, a set of higher photon energies from 91 to 275 eV was used at FLASH free-electron laser in Hamburg. On both facilities, the pulse duration was between 30 and 80 fs, and diamond samples were exposed to single pulses at a normal incidence. The *ex situ* analysis of the irradiated samples was made by using optical microscopy and Raman spectroscopy techniques. Thus, changes in optical refractive index were fixed and graphitization energy threshold of  $\sim 0.7$  eV/atom was estimated. The analysis of Raman spectra peaks indicated a completed solid-to-solid phase transition and forming of graphite crystallites [86]. These experiments proved the capability of soft X-rays to graphitize diamond, but did not follow the dynamics of the process in time.

Later, despite many complexities, an experiment on soft X-rays induced graphitization of diamond was performed at FERMI@Elettra facility near Trieste, Italy by Franz Tavella, Sven Toileikis et al. [110] This experiment seems to be the first one where the non-thermal ultrafast graphitization of poly-crystalline diamond induced by X-ray irradiation was observed in a time-resolved manner. In the experiment, soft X-ray pulses of 47.4 eV photon energy and 52.5 fs duration were used, cross-correlated by optical probe pulse of 32.8 fs duration. A direct simulation of an experiment with such parameters is feasible for the XTANT code.

The experimental method was based on the solid-state target EUV/optical cross-correlation [110]. The wavefront of the FEL is tilted with respect to the target. The FEL fluence is spatially and temporarily encoded into the surface of the target. The evolution of the structural transformation was probed by the laser with a wavefront parallel to the target. In the experiment, a polished poly-crystalline CVD diamond (a product of the chemical vapour deposition (CVD), which allows to produce solid materials with high purity) of 300  $\mu\text{m}$  was used.

The incident angle of the FEL pulse was  $20^\circ$  with respect to the surface, while the probe pulse propagated under normal incidence to the surface. The center wavelength of

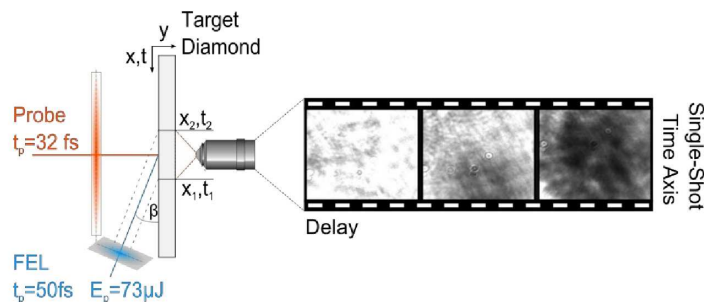


**Figure 4.15:** Schematic picture of the experimental setup reproduced from [110]. The  $\beta$  is an angle between FEL beam propagation and the sample surface. During a single shot a spatial-temporal encoding was performed. An optical probe pulse for the measurement of transmission signal was oriented at the normal incidence to the surface. Additional time scanning of the delay between the FEL pulse and the probe pulse was also provided.

the probe pulse was 630 nm and the center photon energy of a pump FEL pulse was  $\sim 47.4$  eV. With the spatially encoded measurements an access to different fluences was available, among which the highest one exceeded at least  $10 \text{ J/cm}^2$  [110]. In Fig. 4.15 a schematic sketch of the experiment is presented.

After the samples were irradiated, the post-mortem analysis of them was made. It showed a presence of a graphitized layer on the surface of the poly-crystalline diamond substrate [110]. In the experiment the transmitted signal was measured. Signal intensities were dependent on the transmission of post-mortem samples which was equivalent to the graphitized layer thickness.

For the post-mortem analysis, also the atomic force microscopy (AFM) was used to map the sample surface morphology. Confocal Raman spectroscopy, sensitive to the sample microstructure, was performed. It identified the peaks which are characteristic for nanocrystalline graphite (nc-C). Finally, X-ray photoelectron spectroscopy defined the graphite-like electronic configuration (i.e., with  $sp^2$  bonds). With time-resolved tool applied during the graphitization phase, the transmission signal was measured at different time instants

with a resolution of  $\sim 10$  fs, and in such a way the transient transmission curves for the graphitization process were obtained [110].

As we know from the previous sections, for soft X-ray photon energies, as used in the experiment, graphitization process can occur already during the pulse exposure, specifically because a sufficient number of electrons can be promoted to the conduction band very fast. The band gap collapse due to the weakening of interatomic bonds occurs within  $\sim 50$  fs after the pulse maximum, i.e. as well during the pulse exposure. After forming  $sp^2$  bonds instead of  $sp^3$  bonds the graphitization process is completed within additional 50-100 fs.

Due to the small attenuation length of photons under experimental conditions ( $\lambda_{\text{att}} \sim 26$  nm for diamond irradiated with FEL-photons of 47.4 eV at  $20^\circ$  incident angle; meaning that a pulse intensity is  $I = I_0/e$  at this depth, where  $I_0$  is the initial pulse intensity) [111], a diffusion effect has an important impact on the experimental results. The treatment of diffusion will be discussed in detail in the next Subsection. Here, we will concentrate on the changing affected layer, which is connected with the heat diffusion and hot-carrier transport. In addition to our usual model assumptions for the calculation of transient optical properties in XTANT, we assume that the thickness of the affected layer evolves from the attenuation length  $\lambda_{\text{att}}$  to a transient graphite thickness estimated from data at  $t = 400$  fs. We assume that affected layer thickness  $\lambda \sim (t/\tau)^{1/2}$ , where  $\tau = 1500$  fs which corresponds to a time scale where transport and relaxation effects must play a role. Additional study showed that a particular choice of  $\tau$  does not significantly affect the transmission curve. If we choose  $\tau = 500$  fs, the change in the shape of the curve would be noticeable only at much longer times, i.e., after graphitization took place (Fig. 4.16).

The transmission coefficients are convolved with the finite-duration probe pulse which led to the smoothing of the curves. The theoretical transmission curve was also shifted along the time axis to match the position of the pulse maximum. It was then normalized to the initial transmission of non-irradiated diamond.

The comparison of experimental and theoretical plots for 0.8 eV/atom absorbed dose shows a very good agreement (Fig. 4.17). As a comparison, theoretical predictions for 0.6 eV/atom dose are shown.

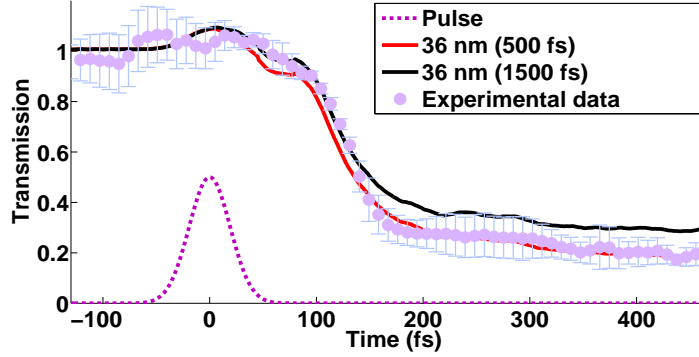


**Figure 4.16:** Experimentally observed [110] transient optical transmission signal from X-ray irradiated diamond (purple points with errorbars) for 630 nm probe pulse and theoretically predicted transmittance assuming the evolution of the affected layer of 36 nm transient thickness at 400 fs with: (i) the time constant  $\tau = 500$  fs (solid red line), and (ii)  $\tau = 1500$  fs (solid black line). FEL photon energy  $\hbar\omega = 47.4$  eV, pulse duration  $\tau = 52.5$  fs (FWHM, dashed violet line).

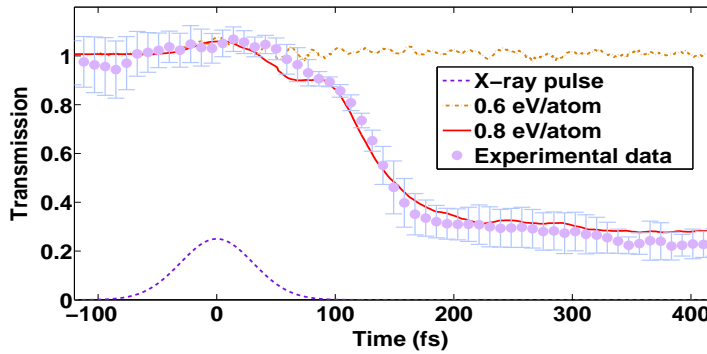


**Figure 4.17:** Experimentally observed [110] transient optical transmission signal from X-ray irradiated diamond (purple points with errorbars) and theoretically predicted transmittance for absorbed dose of 0.6 eV/atom (below threshold; dot-dashed orange line) and 0.8 eV/atom (above threshold; red solid line), 630 nm probe pulse. FEL photon energy  $\hbar\omega = 47.4$  eV, pulse duration  $\tau = 52.5$  fs (FWHM, dashed violet line). Predicted transient graphite layer thickness at 400 fs is 38 nm.

There are three stages of the graphitization process that can be distinguished with the experimental and theoretical curves. During the first stage, initial electronic excitation occurs during the FEL pulse. Due to secondary cascading processes, photoelectrons relax to the bottom of the conduction band within a few femtoseconds. This stimulates an initial increase of the transmission coefficient, which is seen on the plots, and a simultaneous decrease of the reflectivity coefficient. The first stage lasts several tens of fs, in case of the pulse duration of  $\sim 50$  fs, approximately until the maximum of the FEL pulse.

The second stage corresponds to the band gap collapse and lasts  $\sim 50$  fs after the maximum of the pulse. It is reflected in the slight decrease of transmission which precedes a short-lived plateau. Duration of this plateau characterizes a time delay between the final band gap collapse and the atomic relocation to the new equilibrium positions.

The steep decrease of the transmission occurs during the third stage of the graphitization and is connected with an atomic rearrangement and breaking of bonds between atoms. This stage starts at 80-150 fs after the maximum of the FEL pulse and lasts 50-100 fs. All three stages are clearly visible in Fig. 4.17. The graphitization occurs within  $\sim 150$  fs in total. The transmission coefficient does not fully drop to zero, as in the simulations discussed in Section 4.2.1, because we assume a different photon attenuation length in the experiment ( $\lambda_{att} \sim 26$  nm in FERMI experiment versus  $\lambda_{att} \sim 100$  nm considered before). As a result, a thin layer of graphite is formed which is partly transparent to the light of 800 nm wavelength. The transmission curve generated for 0.6 eV/atom dose has only a very slight decrease of transmission. For any under-damage threshold dose the transmission curve does not decrease below  $\sim 0.9$  [110]. In case of above-damage threshold dose the second major decrease is presented and can be assigned as an evidence of graphitization.

For all fluences used in the experiment, graphitization occurs on the same time scale of 150-200 fs. Various fluences produced different transient graphite layers. The higher fluences gave the thicker graphite layers which lowered the transparency of the layers to the optical pulses (see Fig. 4.18). From these plots we may also conclude that the finite value of transmittance after the FEL pulse propagation is lower at thicker graphitized layers.

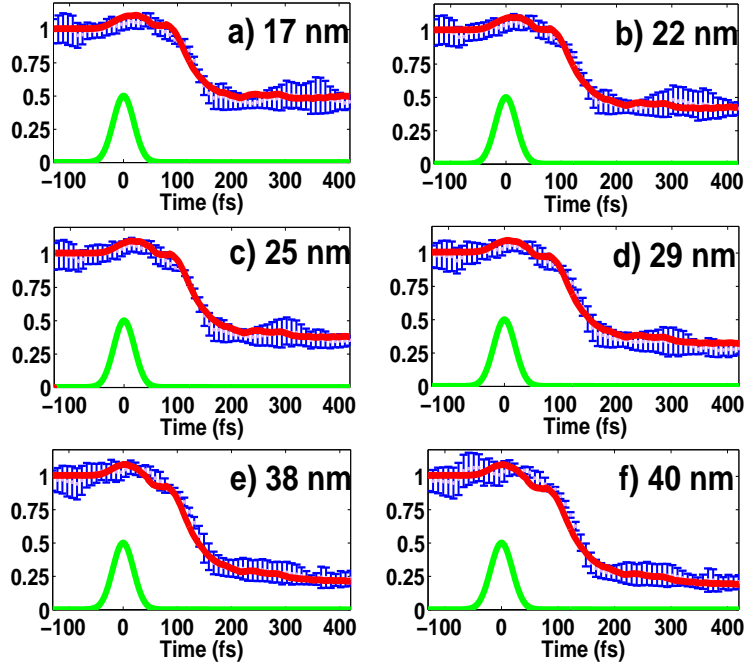


**Figure 4.18:** Experimentally observed (blue errorbars) [110] and simulated (red line) transient optical transmission signal from X-ray irradiated diamond for 630 nm probe pulse. Different pulse fluences produced various transient graphite layers at 400 fs: a) 17 nm; b) 22 nm; c) 25 nm; d) 29 nm; e) 38 nm; f) 40 nm. FEL photon energy  $\hbar\omega = 47.4$  eV, pulse duration  $\tau = 52.5$  fs (FWHM, green line).

Simulations with different transient layer thicknesses (central value of  $38 \pm 4$  nm) are shown in 4.19. All of the transient layer thicknesses between 34 and 42 nm are within the experimental errorbars. The simulations are compared to the experimental results shown in Fig. 4.18e. This comparison gives an estimate for a 'fit' error during adjusting the transient layer thickness in the simulation to the experimental data.

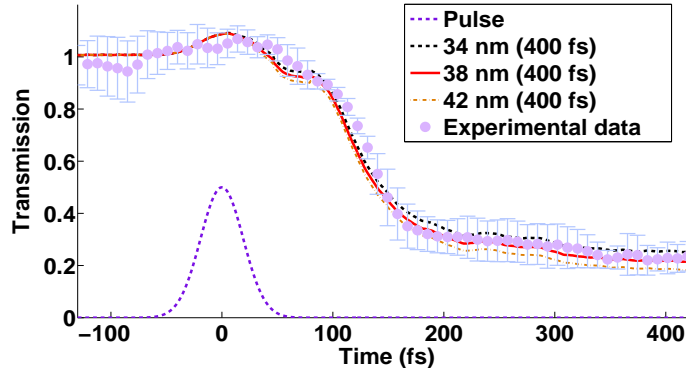


**Figure 4.19:** Experimentally observed [110] transient optical transmission signal from X-ray irradiated diamond (purple points with errorbars) for 630 nm probe pulse and theoretically predicted transmittance for various absorbed doses and correspondingly for different predicted transient graphite layers at 400 fs: 34 nm (dot-dashed orange line), 38 nm (solid red central line), 42 nm (black dashed line). FEL photon energy was  $\hbar\omega = 47.4$  eV, pulse duration  $\tau = 52.5$  fs (FWHM, dashed violet line).

The simulated total number of electrons in the conduction band (both in high- and low-energy domain) are shown in Fig. 4.20. During the FEL pulse the number of conduction band electrons rises up. For the above damage threshold case, there is a second increase of the conduction band electron density, which takes place at around 70 fs, while the band gap collapse is going on. In the below threshold case the number of conduction band electrons stays the same after the pulse. The cooling down of electrons and the recombination process take place on a time scale of  $\sim 200$  ps [112] and is not accounted in the model.

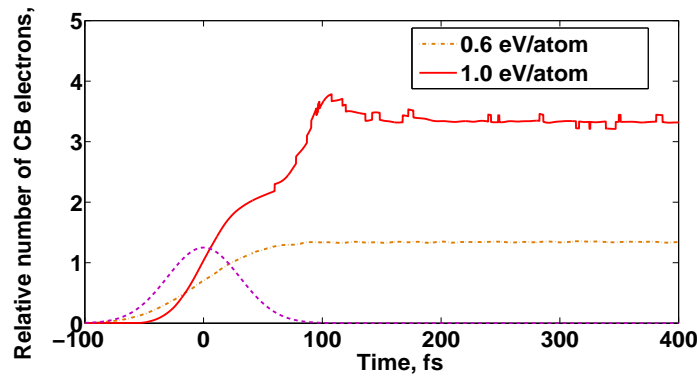


**Figure 4.20:** Theoretically predicted relative numbers of conduction band electrons in FEL irradiated diamond as a function of time for absorbed doses of 0.6 eV/atom (dot-dashed orange line) and 0.8 eV/atom (solid red line). FEL pulse photon energy was  $\hbar\omega = 47.4$  eV, pulse duration  $\tau = 52.5$  fs (FWHM, dashed violet line), as in the experiment.

#### 4.2.5 Diffusion processes

For a simple diffusion study, we added the rate equations for the electron and atomic temperatures into the XTANT, representing cooling via interaction with the bath (unexcited parts of the crystal) [113]:

$$dT_{e,a}(t)/dt = -(T_{e,a}(t) - T_{\text{bath}})/\tau. \quad (4.8)$$

They represent heat transport out of the electronic and atomic systems, similar to the relaxation time approximation presented in [18];  $T_{e,a}(t)$  are the transient temperatures of electrons and atoms;  $T_{\text{bath}}$  is the temperature of the bath equal to the room temperature;  $\tau$  is the relaxation time, for this study case chosen to be 500 fs. This time corresponds to the characteristic relaxation time of the affected layer which was introduced above.

The heat diffusion plays a significant role for the absorption of the dose below the damage threshold. For the above threshold doses the material excitation and structural transformation are too fast to be affected by the diffusion effects [110]. However, by including the cooling of the simulation box, the damage threshold has slightly changed. In the simulation with the chosen parameters, and for 64 atoms in the simulation box,

the threshold appeared to be around 1.1 eV/atom [110], higher than in the case without transport effects. This was expected, because a part of the energy got lost. For the below threshold dose, the band gap transiently shrinks and then restores, preventing proper graphitization. The optical transmission coefficient shows similar behavior, with an initial slight drop and then restoration at longer time scales. Let us note that the relaxation time approximation for heat diffusion is too simplistic and does not reflect the whole complexity of the process.

A more sophisticated way to account for the diffusion effect is to imply conventional diffusion equations – these are partial differential equations (PDE). Such type of equations is widely used in mathematical physics, e.g. for calculations of thermal heat transport or string oscillations - the time-resolved processes that have a source, distributing them in space. Depending on the process, these equations can be of parabolic, hyperbolic or elliptic type, and have different boundary conditions [114].

The diffusion equation can also be either stationary or non-stationary. Non-stationary diffusion equation is classified as a parabolic differential equation which describes the distribution of a diffusing substance. If the distribution is time-independent, the equation becomes stationary and elliptic. The solution of the diffusion equation assumes finding a dependence of material concentration on spatial coordinates and time. In our case we estimate electron heat diffusion within the irradiated bulk. As the laser spot size ( $\sim 6.2 \times 128.1 \mu\text{m}^2$  [110]) is much greater than the attenuation length, we can assume a single-dimensional spread of hot electrons into the depth of the bulk, i.e. in the direction of the pulse propagation [28]. Thus, the diffusion equation will take the form [114]:

$$\frac{\partial}{\partial t}F(x, t) = \frac{\partial}{\partial x}D\frac{\partial}{\partial x}F(x, t) + f(x, t), \quad (4.9)$$

where  $F(x, t)$  is a space- and time-dependent absorbed dose in eV/atom,  $f(x, t)$  is a function describing the source behaviour and the inhomogeneity of the process. The diffusion coefficient  $D$ , in case of cubic semiconductor under nondegeneracy condition in the thermal equilibrium, can be defined by the classical Einstein relation [19]:

$$D = \frac{\mu_e k_B T}{e}, \quad (4.10)$$

where  $\mu_e$  is the mobility or the ratio of the particle drift velocity to an applied force.

The evaluation of the coefficient  $D$  in the case of excited diamond represents a bottleneck for the implementation of this PDE-based diffusion model, as the diffusion coefficient  $D(x, t)$  must have been both space- and time-dependent. Such parameterization cannot be presently achieved. The constant values of hot electron diffusion coefficients in laser-irradiated diamond during the relaxation were then used from [115].

The source function  $f(x, t)$  [114, 116], describing the dose brought by the incoming pulse and spread within the material, can be qualitatively represented as:

$$f(x, t) = F_0 \cdot \exp(-x/\mu) \cdot \exp(-t^2/\tau^2). \quad (4.11)$$

Here  $F_0$  is the total absorbed dose (or fluence),  $x$  is a layer thickness of the material (spatial coordinate),  $\lambda_{\text{att}}$  is an attenuation length for XUV photons ( $\lambda_{\text{att}} = 26$  nm under experimental conditions),  $\tau$  is an incident FEL pulse duration. Thus, the source function contains a spatial part, which describes how far the affected layer is located from the attenuation length, and a temporal part, which represents the Gaussian FEL pulse.

We impose Neumann boundary condition  $\partial F(x, t)/\partial x = 0$  [114] to the solution of the equation, meaning that there is no flux over the surface of the bulk. The solution of the PDE with Neumann boundary conditions is well known [116] and with presented source function looks as:

$$F(x, t) = \iint_{\xi, \tau'} \frac{F_0}{\sqrt{4\pi D(t - \tau')}} \left[ \exp\left(-\frac{(x - \xi)^2}{4D(t - \tau')}\right) + \exp\left(-\frac{(x + \xi)^2}{4D(t - \tau')}\right) \right] \times \quad (4.12) \\ \times \exp\left(-\frac{\xi}{\lambda_{\text{att}}}\right) \cdot \exp\left(-\frac{\tau'^2}{\tau^2}\right) d\xi, d\tau'.$$

In Fig. 4.21 time-dependent dose distribution at discrete layers is shown. The diffusion coefficient  $D$  is equal to  $100 \text{ cm}^2/\text{s}$  or  $(10 \text{ nm}^2/\text{fs})$  which corresponds to the estimates made in [115, 117]. The estimates were made for the minimal ( $4.7 \text{ J}/\text{cm}^2$ ) [110] and maximal<sup>3</sup>

---

<sup>3</sup>Here the lower estimate of the peak fluence is taken, which is calculated from the transmission measurements [110].

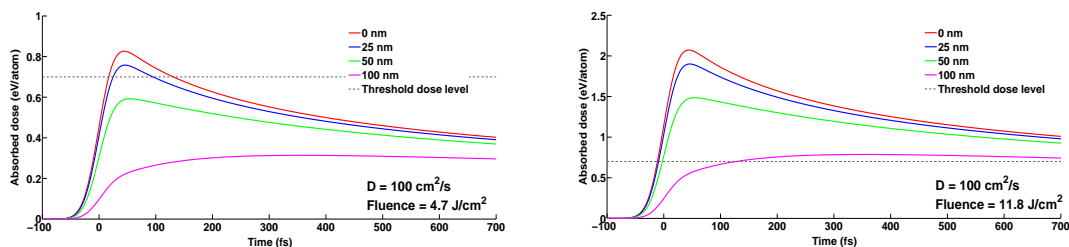


**Figure 4.21:** Distribution of energy doses absorbed by diamond sample at its surface (solid red lines), layer depths of 25 nm (solid blue lines), 50 nm (solid green lines) and 100 nm (solid magenta lines) for FEL pulse fluences of  $4.7 \text{ J/cm}^2$  (left) and  $11.8 \text{ J/cm}^2$  (right). The dashed black lines denote graphitization threshold of  $0.7 \text{ eV/atom}$ . The diffusion coefficient  $D = 100 \text{ cm}^2/\text{s}$ .

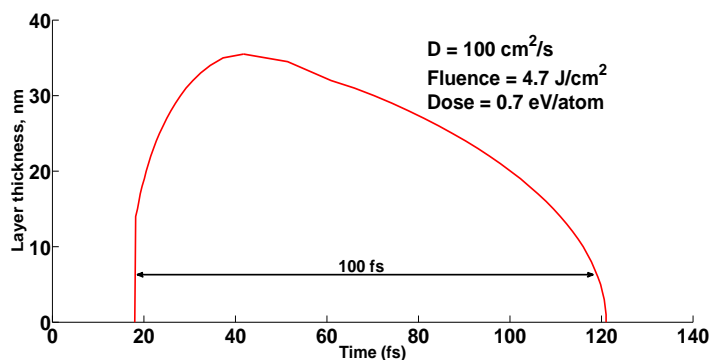


**Figure 4.22:** Distribution of  $0.7 \text{ eV/atom}$  threshold absorbed dose within the diamond sample as a function of time for FEL pulse fluence of  $4.7 \text{ J/cm}^2$ . The diffusion coefficient  $D = 100 \text{ cm}^2/\text{s}$ . The length of the line segment (black double arrow as an example) at a certain layer thickness value denotes the time during which the threshold dose of  $0.7 \text{ eV/atom}$  or higher is kept within the layer. Within  $\sim 7 \text{ nm}$  thick layer such dose is captured for 100 fs which is sufficient for graphitization.

(11.8 J/cm<sup>2</sup>) [110] fluences used in the FERMI experiment. They confirmed that the minimal fluence was sufficient to overcome the graphitization threshold dose of 0.7 eV/atom to the subsurface layer and the maximal one could deliver such dose down to 50 nm depth. The delivered threshold dose should be maintained for at least 100 fs within the layer to cause graphitization [5]. In Fig. 4.22 we see for how long the threshold dose stays within the layer at the minimal fluence. For layers up to  $\sim 7$  nm it keeps for more than 100 fs. The maximal fluence gives the maximum absorbed dose of over 1 eV/atom and then relaxes to lower values. The minimal fluence gives nearly homogeneous electron density within the layer, with thickness up to few tens of nm. This leads us to the conclusion that the choice of one particular dose in our simulations was justified.

## 4.3 Silicon

Let us now analyze silicon, another example of a semiconductor whose transformations and related optical properties were studied with XTANT. It is a non-organic indirect semiconductor, and its band gap width of  $\sim 1.1$  eV at room temperature [118] is used as a benchmark to separate narrow and broad band gap semiconductors. Silicon is extensively used in industry and electronics due to its high abundance on Earth and inexpensive technological applications. The indirect band gap implies that the electron momentum ( $\mathbf{k}$ -vector), at which the energy of the top of the valence band has its maximum, does not coincide with the momentum, at which the bottom of the conduction band has its minimum.

### 4.3.1 Modelling of phase transitions in silicon

The two mechanisms of amorphization of silicon are thermal and non-thermal melting [21, 119–121]. Thermal melting is a result of the lattice heating due to electron-phonon coupling. In the experiments without an ultrafast laser excitation this type of melting is usually observed. Non-thermal melting has the same features as non-thermal graphitiza-

tion of diamond: when a density of electrons excited to the conduction band overcomes a certain threshold, the interatomic potential significantly changes. However, the dose needed to trigger the thermal amorphization of diamond is higher than the dose needed for its non-thermal graphitization [21]. For silicon the situation is the opposite: the deposited dose for non-thermal melting must be higher than for thermal melting. Moreover, in silicon we may also observe an interplay of these two processes, when both of them affect the optical properties [21].

Depending on the absorbed dose, solid-state silicon can also form low-density liquid (LDL) or high-density liquid (HDL), while being amorphized. The estimated threshold dose for a solid-LDL phase transition is  $\sim 0.65$  eV/atom, and for a solid-HDL phase transition (full amorphization) is  $\sim 0.9$  eV/atom, which corresponds to  $\sim 5\%$  of electrons excited from the valence to the conduction band [21, 98]. The transition from an ordered state of silicon to a disordered LDL state, after the atomic system is exposed to the FEL pulse and absorbs dose of 0.66 eV/atom, is presented in snapshots in Fig. 4.23. The cubic symmetric structure of silicon undergoes disordering, however, preserving local order. In Fig. 4.24 the transition of a solid silicon to HDL phase at 1.78 eV/atom absorbed dose is shown. Here we can already see a highly disordered state which corresponds to a high-density liquid phase.

For the description of non-thermal effects the Born-Oppenheimer approximation could be used as presented in [5, 20]. If we want to address the thermal melting, we have to go beyond this approximation [122], otherwise the electrons are insensitive to nuclei motion, i.e., atomic motion does not affect electron transition between the levels. Let us rewrite the Boltzmann collision integral, describing the evolution of the electron distribution function on the energy levels, from the Eq. (3.37):

$$\frac{df_i}{dt} = \sum_j I_{i,j}^{e-e} + \sum_j I_{i,j}^{e-at}, \quad (4.13)$$

where  $I_{i,j}^{e-e}$  is an electron-electron collision integral,  $I_{i,j}^{e-at}$  is an electron-atom collision integral. In the Born-Oppenheimer approximation the  $I_{i,j}^{e-at} \equiv 0$  as there is no electron-atom energy exchange. Therefore, the model should be extended with addition of the

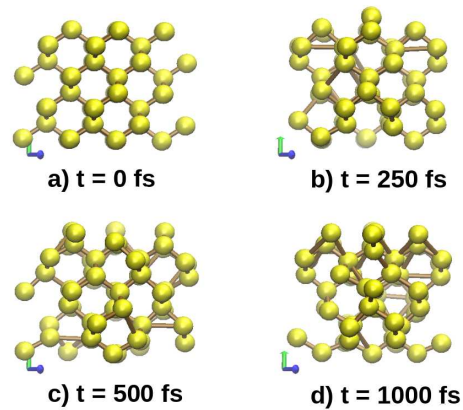


**Figure 4.23:** Snapshots of atomic positions in silicon irradiated with a dose of 0.66 eV/atom at different time instants: a) 0 fs; b) 250 fs; c) 500 fs; d) 1000 fs.

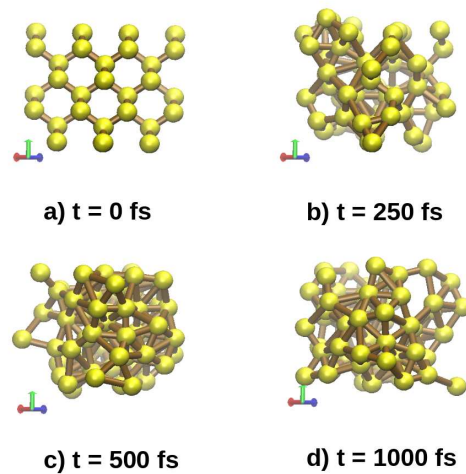


**Figure 4.24:** Snapshots of atomic positions in silicon irradiated with a dose of 1.78 eV/atom at different time instants: a) 0 fs; b) 250 fs; c) 500 fs; d) 1000 fs.

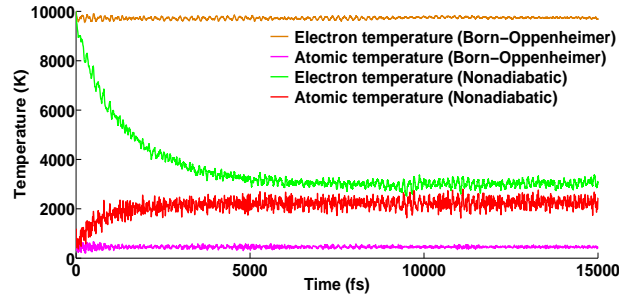


**Figure 4.25:** Simulated temperatures of atoms and electrons of silicon in Born-Oppenheimer approximation and nonadiabatic scheme. Initial electron temperature  $T_e = 10\,000$  K, initial atomic temperature  $T_a = 300$  K. A supercell with  $N = 64$  atoms and constant volume is used in the simulation.

nonadiabatic coupling between the electrons and the lattice. The full form of the collision integral  $I_{i,j}^{e-at}$  can be found in Subsection 4.3.3.

A comparison of the Born-Oppenheimer model and the nonadiabatic model is made in Fig. 4.25 on a time scale of 15 ps, showing the relaxation of electronic and atomic subsystems, where electrons have an initial temperature  $T_e = 10\,000$  K and atoms have the room temperature  $T_a = 300$  K. The Born-Oppenheimer scheme does not exhibit any energy exchange between electronic and atomic subsystems, while the nonadiabatic scheme predicts electron-lattice thermalization.

Now we will employ extended XTANT model with nonadiabatic extension for the calculation of optical properties of silicon which undergoes a phase transition. The characteristic behaviour of the optical coefficients turns out to be similar to the case of diamond-graphite phase transition with well pronounced increase of the reflectivity and a decrease of the transmission to zero. However, in case of silicon, both thermal and non-thermal melting contribute to the amorphization simultaneously. That results in some qualitative differences with the graphitization scheme, where the thermal melting starts to play a noticeable role only on a time scale of 1 ps.

We may decouple these two processes by selecting either the dose which is slightly above the threshold for solid-LDL transition or which is far above solid-HDL transition

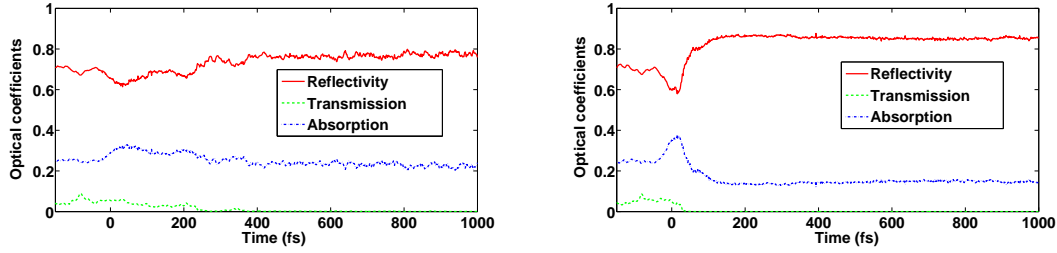


**Figure 4.26:** Simulated optical coefficients of silicon (reflectivity - solid red line, transmission - dashed green line, absorption - dot-dashed blue line) irradiated with a dose of 0.66 eV/atom (left) and with a dose of 1.78 eV/atom (right). FEL pulse photon energy  $\hbar\omega = 50$  eV, pulse duration  $\tau = 90$  fs, probe wavelength  $\lambda = 625$  nm, layer thickness  $d = 100$  nm.

threshold [98]. In the first case, the thermal melting would dominate, while in the second case the non-thermal melting would be more significant.

In Fig. 4.26 one can see that for the lower dose (0.66 eV/atom) reflectivity is increasing slowly and saturates only on a time scale of 1 ps. Thermal melting dominates there. At the higher dose (1.78 eV/atom), we observe a quick reflectivity overshooting on a time scale of 100 fs. It was also occurring for diamond, as the non-thermal process dominates there as well. The drop of transmission also occurs more rapidly, when compared to the lower dose case – for the latter case it takes  $\sim 400$  fs.

The occurrence of an ultrafast non-thermal melting in silicon is indicated by the analysis of diffraction patterns in [123]. Therein, the thermal and non-thermal melting are also qualified as processes competing in time, and both occur within 1 ps after irradiation. For the thermally melted silicon, the pattern is expected to be a superposition of the solid state part and a part that is already melted at 100 fs. However, the pattern depicted at 100 fs after femtosecond irradiation cannot be defined as such a superposition, therefore, it represents a signature of the non-thermal transition on an ultrafast time scale [123].

### 4.3.2 Optically induced radiation damage in silicon

The experiment on silicon amorphization was performed by Sokolowski-Tinten et al [109]. The standard femtosecond pump-probe technique was applied, and the probe pulse was extracted from the pump pulse by separating a small fraction of it. The pump beam angle of incidence was  $56^\circ$ , while the probe pulse angle of incidence was  $70.5^\circ$ . The experiment was similar to Reitze's experiment with diamond [96] in terms of the pulse parameters, as both the pump and probe pulses had the same optical wavelength ( $\lambda = 625$  nm in [109]). The measurements of the reflectivity were done for different fluences.

To simulate the experiment, we again used soft X-ray photon energy (50 eV) for the pump pulse. In Fig. 4.27 optical coefficients of silicon at the absorbed dose of 1.0 eV/atom are shown. The modeled reflectivity coefficient is in a good agreement with experimental results [109]. For this specific dose, the rise of reflectivity is relatively slow, and saturation is reached on a time scale of 500-600 fs. That supports an assumption of two contributing melting processes for such doses - thermal and non-thermal.

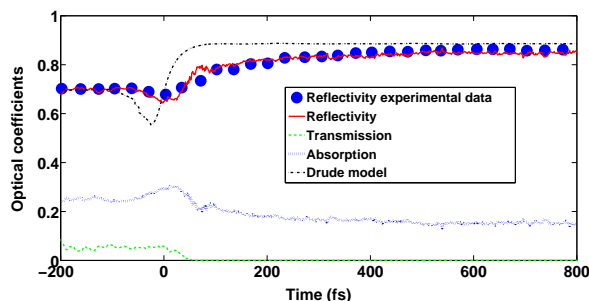


**Figure 4.27:** Modeled optical coefficients of non-equilibrium silicon irradiated above the damage threshold, at the absorbed dose = 1.0 eV/atom, photon energy  $\hbar\omega = 50$  eV, pulse duration  $\tau = 100$  fs. Angle of the pump pulse incidence is  $56^\circ$ , of the probe pulse incidence is  $70.5^\circ$ ; probe wavelength is  $\lambda = 625$  nm. The dots represent experimental data for the reflectivity coefficient [109], the solid line represents the calculated reflectivity coefficient, the dashed line is the calculated transmission coefficient, the dotted line is the calculated absorption coefficient obtained within TB model, and the dot-dashed line is the reflectivity coefficient obtained with Drude model.

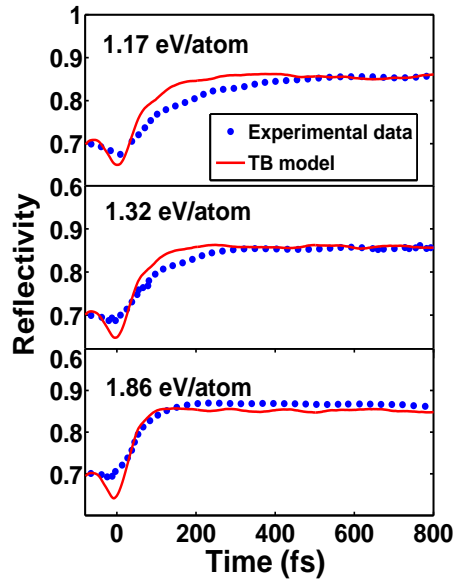


**Figure 4.28:** Transient reflectivity of silicon measured in the experiment [109] in comparison with TB model predictions for the absorbed doses of 1.17 eV/atom ( $1.8F_m$ ), 1.32 eV/atom ( $2.2F_m$ ) and 1.86 eV/atom ( $3.1F_m$ ).

The simulations performed for other above-threshold doses, as in Sokolowski-Tinten’s experiments for high fluences (above  $1.8F_m$ ) [109], give results close to the experimental ones (Fig. 4.28). The discrepancy between experiment and theory during the pulse was already explained for the case of diamond. The discrepancy with the experimental results for fluences slightly above the threshold (below  $1.8F_m$ ) will be explained in the next Subsection.

An example of silicon once again confirms that the optical properties are strongly linked with the atomic structure. Abrupt changes of optical properties occur together with non-thermal phase transitions. Their time scale matches very well the experimental observation of non-thermal melting. The HDL phase is reached after an intermediate LDL phase which may be not observed in case of higher deposited doses. Thermal melting, for the case of smaller doses, is a consequence of atomic heating, and its time scale is governed by the electron-phonon coupling. The electron-lattice thermalization time for silicon typically exceeds 1 ps [124].

### 4.3.3 Effect of electron-ion coupling on optical properties

After the excitation, photoelectrons start to relax and exchange their energies with ions via electron-phonon coupling, typically on picosecond time scales. The Fermi's Golden Rule (FGR) is widely used for the observation of electron kinetics in irradiated solids on a femtosecond time scale [76, 125–127]. However, the applicability of the FGR in plasma is disputed, for example, in [128]. For the case of femtosecond laser pulses with a subsequent change of the potential energy surface and phase transitions, FGR assumptions are violated. The periodic harmonic motion of atoms, necessary for FGR, cannot be assumed after atomic relocations and breaking of the crystal symmetry. Moreover, electron-phonon scattering event time ( $t_{ph} \sim 1/\omega_{ph}$ ) [65, 129, 130], which can be estimated by the inverse phonon frequency, can reach a value from a few tens up to a hundred of femtoseconds, i.e., can be on the same order of magnitude as ultrafast processes in the material we deal with. Regarding these FGR limitations, in [76] we proposed to use a more general dynamical coupling (DC) model [131].

In XTANT, the nonadiabatic electron-ion coupling is introduced, using the Boltzmann collision integral,  $I_{i,j}^{e-at}$  [21, 76, 132]:

$$I_{i,j}^{e-at} = w_{i,j} \begin{cases} f_e(E_i)(2 - f_e(E_j)) - f_e(E_j)(2 - f_e(E_i))G_{at}(E_i - E_j), & \text{for } i > j, \\ f_e(E_i)(2 - f_e(E_j))G_{at}(E_j - E_i) - f_e(E_j)(2 - f_e(E_i)), & \text{for } i < j, \end{cases} \quad (4.14)$$

where  $w_{i,j}$  is the rate for an electron transition between the energy levels  $i$  and  $j$ ; here  $f_e(E_i)$ , a transient electron distribution function, is assumed to yield the Fermi-Dirac distribution. It defines electron population on the energy level  $E_i$  (eigenstate of the transient TB Hamiltonian). The function  $G_{at}(E)$  is the integrated Maxwellian function for atoms.

The scattering rate, assuming an instant scattering event (Markovian process) and periodic atomic motion, is defined by the FGR as [131]:

$$w_{ij} = \frac{2\pi}{\hbar^2} |M_{e-at}(E_i, E_j)|^2 \delta(\omega_{ij} - \omega_{ph}), \quad (4.15)$$

where  $\omega_{ph}$  is a phonon frequency,  $\omega_{ij} = (E_i - E_j)/\hbar$ , and the matrix element for electron-ion scattering  $M_{e-at}(E_i, E_j) = (\langle i(t)|j(t + \delta t)\rangle - \langle j(t)|i(t + \delta t)\rangle) (E_j - E_i)/2$  [133].

The dynamic coupling model estimates the scattering rate taking into account its time dependence without an assumption of the harmonic atomic oscillations or long time scales [76, 131]:

$$w_{i,j} = |(\langle i(t)|j(t + \delta t)\rangle - \langle i(t + \delta t)|j(t)\rangle) / 2|^2 \frac{1}{\delta t}, \quad (4.16)$$

where  $\langle i(t)|$  and  $|j(t + \delta t)\rangle$  are the  $i$ -th and  $j$ -th eigenfunctions of the Hamiltonian at the time instants  $t$  and  $t + \delta t$ . Therefore, the dynamical coupling takes into account the system evolution during an ongoing time individual 'collision' and the induced energy exchange [76].

Electron transitions through the band gap for broad-band gap materials, such as diamond, are excluded from the collision integral (in XTANT, already the transitions across 5 eV are excluded). The particular choice of the acceptance window width between  $\sim 3$  eV and  $\sim 6$  eV does not change the simulation results noticeably [76].

The convergence study performed with XTANT for silicon showed that the usage of FGR produces divergent results, and the resulting heating rate is then strongly dependent on the MD time step. In contrast, the calculations made with the DC scheme employed, showed the convergence for the electronic temperature in silicon with the MD time step  $\Delta t \sim 0.01$  fs. With a longer time step, the coupling rate becomes overestimated [76].

To compare the DC and Born-Oppenheimer schemes (FGR cannot be compared as it produces non-convergent results), we performed a set of simulations with the same pulse and material parameters. In Fig. 4.29 the calculated reflectivity of silicon exposed to the dose of  $1.3F_m$  is in a reasonable agreement with the experiment [109] in case of the DC model applied. Without any coupling scheme applied (Born-Oppenheimer approximation), reflectivity decreases without overshooting. The behaviour of reflectivity on both graphs strictly depends on the band gap width. Noticeable shrinkage appears only when the dynamical coupling scheme is used.

In Fig. 4.28 we showed the reflectivity coefficients for different over-threshold fluences. Now let us look at these results, from the perspective of the electron-ion coupling schemes. For doses above  $1.8F_m$ , silicon undergoes significant non-thermal melting. The results we

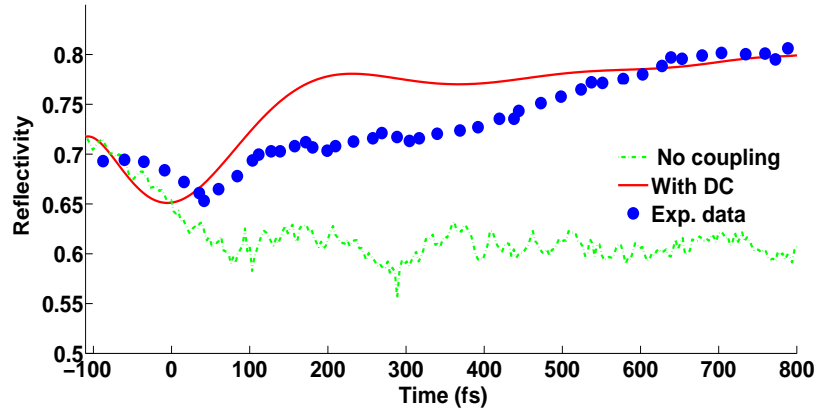


**Figure 4.29:** Transient optical reflectivity of silicon at 625 nm probe wavelength under  $70.5^\circ$  incidence, absorbed dose is  $1.3F_m$ , where  $F_m$  is a critical melting dose. The experimentally measured coefficients from [109] are marked by the blue dots; the coefficients obtained with XTANT model: (i) by using Born-Oppenheimer approximation (no coupling) are marked by the dot-dashed green line; (ii) by using dynamical coupling - by solid red line.

obtained for the reflectivity show that the agreement with the experiment is poorer at lower doses (Fig. 4.29), and at doses above  $1.8F_m$  the agreement is almost perfect. The reasons for that can be found, while analyzing the assumptions of the XTANT model. First, valence and conduction band electrons are supposed to follow a unified Fermi-Dirac distribution and to be in thermal equilibrium. However, at lower irradiation fluences, a distribution of electrons can be non-equilibrium on longer times [126]. As a result, XTANT model can overestimate ion heating. Second, due to the periodic boundary conditions used, all absorbed energy is stored within the supercell, while in experimental conditions a part of it can leave the irradiated area because of the heat diffusion. For diamond, the influence of electron-ion coupling on the threshold dose is less significant than for silicon. Both for silicon and for carbon, the threshold dose is lowered, when compared to the results obtained with the Born-Oppenheimer approximation. Non-thermal transition time scales for diamond are similar in both approaches (from 80 to 150 fs), and for silicon they can be different (up to 500 fs with FGR and up to 1 000 fs with DC) [76]. The best level of agreement with the experiment in terms of the threshold dose and non-

thermal transition time scales is achieved by using the DC approach both for silicon and diamond [76]. Therefore, it should be used in XTANT to properly trace the electron-ion coupling effect.

## 4.4 Gallium arsenide

Gallium arsenide is a semiconductor actively used in industry, e.g., in electronics and solar cells fabrication. It is composed of the elements gallium and arsenic. GaAs is a direct semiconductor. It means that it has the same crystal momentum both at the bottom of the conduction and at the top of the valence band. The band gap width of GaAs is 1.42 eV at the room temperature [118] which is larger than the one of silicon. Such a band gap width is comparable with the optical wavelengths. Thus, optical photons can trigger electron excitation from the valence band to the conduction band. The band gap width, dependent on the lattice temperature, defines the rate of such interband excitations.

Here, we will discuss transient optical properties of irradiated GaAs, starting with a simpler model based on the rate equations and the Drude theory. Afterwards, we will analyze the applicability of the XTANT model for GaAs and discuss arising problems.

### 4.4.1 Electron-lattice thermalization in GaAs

As it was mentioned previously on an example of diamond (Fig. 4.12), the thermalization of conduction band electrons is fast: at a few tens of femtoseconds corresponding to a typical FEL pulse duration, the electron thermalization time scale is  $\leq 200$  fs. The same experimentally established time scale in GaAs was reported in [134, 135]. The electron thermalization time scale is mainly determined by the secondary electron cascading following a FEL irradiation [103]. The cascading duration increases with the increasing photon energy. Due to the ultrafast laser excitation, while electrons of the valence band are being transferred to the conduction band, holes are created in the valence band. The holes can be treated as quasi-particles with a positive charge and an effective mass [33]. The effective

masses of holes and electrons in semiconductors depend on the specific band structure of the material. The dispersion relation at the bottom/top of a band can be approximated in many semiconductors as parabolic [136]:

$$E(k) = E_{edge} + \hbar^2 k^2 / 2m^*, \quad (4.17)$$

where  $E(k)$  is the energy of an electron with a wave vector  $\mathbf{k}$  in the band,  $E_{edge}$  is a constant which stands for the value of the edge of the band, and  $m^*$  is the effective mass. The effective mass is then directly connected to the curvature of the energy band at a specified  $\mathbf{k}$ -vector  $\mathbf{k}_0$ :

$$1/m^* = d^2 E(k) / \hbar^2 (dk)^2 |_{k=k_0}. \quad (4.18)$$

With a decrease of the second derivative of  $E(k)$ , the mass of the corresponding carrier increases. If the top of the valence band is 'flatter' than the bottom of the conduction band, the effective hole masses exceed electron masses in the same material. In GaAs holes are about 10 times heavier than electrons [137, 138]. This means that energy transfer to the heavy holes will be relatively slow while light electrons will exchange energy in the conduction band much faster. Such mutual (interband) thermalization between the valence and the conduction band may take significantly longer time than the carrier thermalization within the individual bands (intraband thermalizations). The interband thermalization is driven by collisional interband processes: collisional ionization and Auger recombination. Such transitions require both energy and wave vector conservation. Band structure has a strong effect on the rate of such processes [139]. Since GaAs is a direct band gap semiconductor, direct interband transitions between the valence and the bottom of the conduction band are suppressed as they cannot maintain both the conservation laws. Generally, phonon-assisted transitions give second-order contribution to collisional processes when compared to the first-order direct transitions [140]. I.e., they have much lower rates than the direct transitions [140], if the direct transitions are allowed. As the result, collisional interband transitions are strongly suppressed in the case of direct semiconductors with band gap widths larger than  $\sim 1$  eV [139], in which fast direct interband transitions are not allowed and only slow phonon-assisted interband transitions can occur. Consequently,

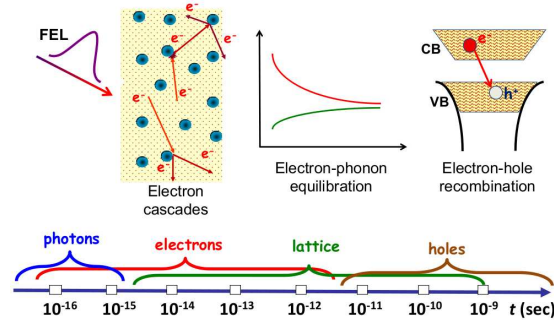


**Figure 4.30:** Schematic picture of excitation and relaxation process in irradiated GaAs involving electrons, holes and phonons, and their time scales.

the distributions of carriers in the conduction and valence band remain for some time strongly non-isothermal. Similar carrier non-isothermality has been observed in [141–143].

The band gap shrinks due to the increase of the lattice temperature. Many sources indicate that characteristic times of electron-phonon relaxation  $\tau_{e-h-latt}$  in GaAs are around 1-5 ps — as shown in ab initio simulations [144, 145], and experiments [146, 147]. After full thermalization, recombination processes start to play a role. In GaAs both radiative and non-radiative recombination occur [148]. The electron-hole recombination time  $\tau_{rec}$  has the order of  $\sim 100$  ns [148], this is by several orders of magnitude longer than the electron-lattice thermalization time. Therefore such radiative recombination cannot influence the electron-lattice equilibration. The schematic picture of all excitation and relaxation processes and their outcomes with time scales is shown in Fig. 4.30.

Having experimental data on the transient reflectivity in hand, we can follow the relaxation of FEL-irradiated GaAs and create a model which uses experimental data as fitting parameters. Optical properties reflect the changes of an atomic structure, their measurements can provide the information on electron-phonon coupling rates and electron-hole thermalization time. In considered experiments, the pump-probe scheme with X-ray pumps and optical probes was used, and relative changes of the transient optical reflectivity were measured. The experiment by Gahl et al. [134] was undertaken at FLASH laser facility

with an XUV pulse (energy of 40 eV) while Krupin's group [135] used a soft X-ray pulse (energy of 800 eV) at LCLS. The probe pulse durations were:  $\sim 100$  fs at FLASH, between 120 and 150 fs at LCLS. The probe pulse wavelengths  $\lambda_{probe}$  were 800 nm ( $\sim 1.55$  eV) in Krupin's experiment and were 800 nm and 400 nm ( $\sim 3.1$  eV) in Gahl's experiment. Both wavelengths are comparable with the band gap, moreover, 1.55 eV is just slightly above the band gap width of 1.42 eV.

Our initially proposed theoretical framework for the interpretation of experimental data [134, 135] used rate equations to describe temporal evolution of the electron distribution [138]. The rate equations were coupled with the two-temperature model [149], describing the equilibration of the electron-lattice temperature. The Drude model was applied to follow the transient reflectivity as a function of free-carrier density. It was extended beyond the free-carrier absorption framework [150] to account for the contribution from optically induced interband transitions, predominant in this regime.

As a first step, we estimated the maximal electron-hole density after FEL irradiation, knowing the pulse fluence and the photoabsorption cross section at a given photon energy. We then used this value to reproduce the increase of the electron-hole density until the maximal density was reached by an approximate linear equation [138, 151]:

$$dn_{e-h}(t)/dt = \gamma_{e-h}(t), \quad (4.19)$$

where the coefficient  $\gamma_{e-h}(t)$  here depends on the pulse fluence and was fitted to obtain the maximal value of  $n_{e-h}$  corresponding to the number of absorbed X-ray photons divided by the average electron-hole pair creation energy  $E_{e-h}$  which equals to 4.2 eV for GaAs [152]. Such increase is typical for FEL irradiated semiconductors as described, e.g., in [151, 153]. The minimum of the  $\Delta R/R$  curve corresponds to the maximal electron-density in the sample [23, 154], which in turn corresponds to the end of the excitation stage. After the maximal electron-hole density was reached, the system started to relax. Electron-lattice thermalization and electron-hole recombination were the predominant relaxation channels. In GaAs, the latter one contributes much less significantly, as it was stated above. Electron-lattice thermalization in GaAs acts on picosecond time scales [146]. Assuming thermal free-

carrier distribution and taking electron-hole recombination into account, a rate equation for electron-hole density can be written as [138]:

$$dn_{e-h}(t)/dt = -\gamma_{rec} \cdot n_{e-h}(t), \quad (4.20)$$

where  $\gamma_{rec}$  is a recombination rate, which includes radiative and non-radiative coefficients for GaAs [148].

At the beginning of the excitation stage, the electron temperature decreases and then reaches some stable value. However, electron-lattice thermalization is insignificant on this stage and the number of the excited electrons is insignificant as well for fluences used in the experiments. Therefore, we assume the linear growth of the temperature with time from the initial atomic room temperature to the temperature  $T_e^{init}$  at the minimum of the  $\Delta R/R$  curve [138].

To describe how electron-hole temperature and lattice temperature change with time we apply the temperature equations [138]:

$$dT_{latt}(t)/dt = +G_{latt}(T_{e-h}(t) - T_{latt}(t)), \quad (4.21)$$

$$dT_{e-h}(t)/dt = -G_{e-h}(T_{e-h}(t) - T_{latt}(t)), \quad (4.22)$$

where the coefficients  $G_{latt}$  and  $G_{e-h}$  are related to heat capacities of the system as [138]:  $G_{latt(e-h)} = G/C_{latt(e-h)}$ . The free carrier – lattice thermalization time is then defined as:

$$\tau_{e-h-latt} = 1/(G_{latt} + G_{e-h}). \quad (4.23)$$

The heat capacities for lattice  $C_{latt}$  and free carriers  $C_{e-h}$  are taken from [33] correspondingly. Coefficient  $G$  is the free carrier – lattice coupling factor. The free carrier – lattice thermalization time  $\tau_{e-h-latt}$  is adjusted to the minimum of  $\Delta R/R$  curve in order to obtain the best fit to the experimental curve [138].

The initial value of the lattice temperature is 300 K. Lattice temperature does not change much during the first 100 – 200 fs after the FEL irradiation (during the electron thermalization) and so the band gap width does not change either. The resulting lattice heating should lead to a shrinkage of the band gap  $E_{gap}$  [155], when compared with its initial

width of 1.42 eV at 300 K. This could result in the experimentally observed 'overshooting' of the transient reflectivity, i.e., its increase above the initial value.

We proceeded in the following steps. The extended Drude model taking into account the interband contribution was used to calculate the transient reflectivity changes from the dielectric function  $\epsilon$ . The dielectric function is parametrized in the same way as in [150]:

$$\epsilon \equiv (n + ik)^2 = \epsilon_{core} - \sum_{j=e,h} \frac{\omega_{p,j}^2}{\omega_\gamma^2} \frac{(\omega_\gamma \tau_j)^2}{(\omega_\gamma \tau_j)^2 + 1} + \sum_{j=e,h} i \frac{\omega_{p,j}^2}{\omega_\gamma^2} \frac{\omega_\gamma \tau_j}{(\omega_\gamma \tau_j)^2 + 1}, \quad (4.24)$$

where  $\epsilon_{core}$  describes all contributions to the dielectric function beyond the free-carrier absorption. Here,  $\epsilon_{core} = (n_{core} + ik_{interband})^2$ , where  $k_{interband} = \alpha \lambda_\gamma / 4\pi$  describes the contribution from the transition between the valence and the conduction bands, using the interband absorption coefficient for a direct interband transition  $\alpha$ , parameterized as in [150]. The frequency  $\omega_\gamma$  is the photon frequency and  $\lambda_\gamma$  is its corresponding wavelength. The absorption coefficient scales with the photon energy  $E_{phot}$ , as  $\alpha \sim \sqrt{E_{phot} - E_{gap}} / E_{phot}$ . Band gap shrinkage is described with the phenomenological relation from [155]. The interband absorption coefficient also contains the matrix element  $\langle v|p|c \rangle$ , which couples the states with the same electron wave vector in the valence and the conduction bands. We parametrized it, using the measured absorption coefficients for GaAs from [156]. The time  $\tau_{e(h)}$  is the electron (hole) collision time and the frequency  $\omega_{p,e(h)}$  is the plasma frequency for electrons (holes). The latter one is estimated with the carrier density  $n_{e-h}$  as  $\omega_{p(e,h)} \sim \sqrt{n_{e-h}}$  [138].

Transient reflectivity can be obtained directly from knowing the transient refraction index  $k_{interband}$  and  $n_{core}$  value. The average electron collision time  $\tau_e$  was fitted in order to match the minimum of the experimental  $\Delta R/R$  curve from [134, 135]. The accuracy of the fit depends on the resolution at which the minimum reflectivity was experimentally measured. The average hole collision time  $\tau_h$  can be estimated from the electron one, using mass scaling relation for electron and hole collision frequencies [33].

The fast drop and rise of the reflectivity is a result of the electron-hole pairs creation in the irradiated GaAs. Both electrons and holes contribute to its optical parameters and their contribution is described by the Drude model. In Fig. 4.31 theoretically predicted

and measured transient reflectivity changes are shown for Krupin's and Gahl's experiments. Three different fluences used in Krupin's experiment were chosen - 10 mJ/cm<sup>2</sup>, 20 mJ/cm<sup>2</sup> and 40 mJ/cm<sup>2</sup> [135, 138] (Fig. 4.31a). A single fluence  $F = 4.1$  mJ/cm<sup>2</sup> [134, 138] for Gahl's experiment was chosen. By iteratively comparing results to experimental data we achieve a good agreement with both experiments.

In Fig. 4.31a with increasing fluence the minimum of the reflectivity curve is lower due to the higher free-electron density and the overshooting effect is stronger as the lattice temperature is increasing correspondingly. The dose  $D_{\text{abs}}$  calculated from the fluence  $F = 4.1$  mJ/cm<sup>2</sup> at FLASH experiment is equal to 0.08 eV/atom<sup>4</sup> which corresponds to the fluence of 40 mJ/cm<sup>2</sup> at LCLS experiment, as at 800 eV the photon attenuation length is around 10 times larger than at 40 eV [111]. Indeed, the minimum of reflectivity of a red curve in Fig. 4.31b matches a minimum of the red curve in Fig. 4.31a [138]. However, the final reflectivity value of the red curve in Fig. 4.31b matches already the final value of a curve for  $F = 10$  mJ/cm<sup>2</sup>,  $\lambda_{\text{probe}} = 800$  nm in Fig. 4.31a (magenta line). Such relative lack of dose in Gahl's experiment is an effect of hot electron diffusion from the interaction volume at picosecond time scales due to the small penetration depth ( $\sim 60$  nm) – so the heat gradients are larger in case of XUV.

The optical coefficients are sensitive to the value of absorption coefficient which, according to various estimates, may differ by a factor of 2 – 3 [152, 156]. This strongly influences the accuracy of the theory predictions (Fig. 4.31b). At a 400 nm probe-pulse the interband absorption coefficient is about 100 times larger than at 800 nm [152, 156]. The reflectivity overshooting does not occur at 400 nm as the large absorption coefficient is then not sensitive to the small change caused by the energy shift due to the band gap shrinking ( $\alpha \sim \sqrt{E_{\text{phot}} - E_{\text{gap}}}/E_{\text{phot}}$ ).

Table 4.1 lists the parameters obtained through an iterative model adjustment to the

---

<sup>4</sup>The calculation of experimental fluence  $F$  in [134] and [135] already took the FEL incident angle  $\theta$  into account. Then the dose, calculated with Eq. (4.2), which gives  $\approx 0.06$  eV/atom for both experiments, must be divided by  $\sin \theta$ . In [134]  $\theta = 48.5^\circ$ , in [135]  $\theta = 45^\circ$ , which gives the final dose  $D \approx 0.08$  eV/atom for both experiments.

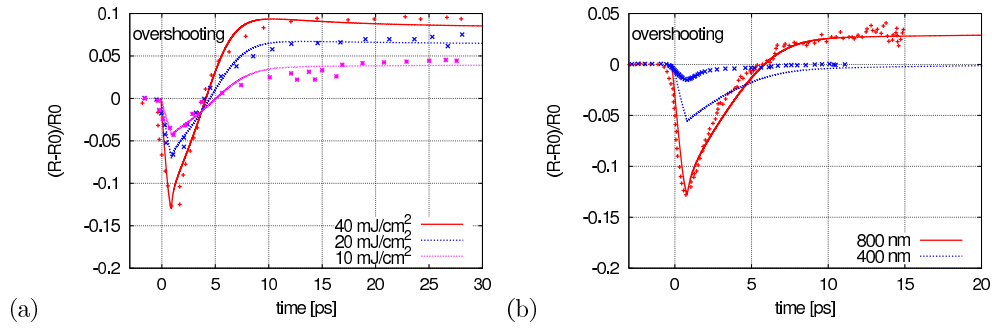


**Figure 4.31:** Time dependence of the relative change of transient reflectivity in irradiated GaAs measured in: a) the experiment on LCLS by Krupin et al. (FEL photon energy  $\hbar\omega = 800$  eV, optical probe wavelength  $\lambda = 800$  nm); b) the experiment by Gahl et al. at FLASH (FEL photon energy  $\hbar\omega = 40$  eV, optical probe wavelengths  $\lambda_1 = 800$  nm and  $\lambda_2 = 400$  nm). The comparisons are made for FEL pulse fluences: a)  $F = 10, 20$  and  $40$  mJ/cm<sup>2</sup>; b)  $F = 4.1$  mJ/cm<sup>2</sup>.

experimental curves in Fig. 4.31a: the thermalization time  $\tau_{el-latt}$  and the free electron temperature at the minimum of  $\Delta R/R$  curve  $T_e^{init}$ . These values lay within the range reported in [146]. Note the expected increase of  $T_e^{init}$  with fluence, and the corresponding decrease of the thermalization time with the electron temperature [146]. The values of  $\tau_{el-latt}$  and  $T_e^{init}$  for Fig. 4.31b at the pulse fluence of  $F = 4.1$  mJ/cm<sup>2</sup> are 2.8 ps and 1.6 eV, respectively, for both 800 nm and 400 nm<sup>5</sup>.

The minimum of the  $\Delta R/R$  curve corresponds to the electron temperature at the end of electron thermalization, which is approximately 5 times higher than the assumed temperature after full thermalization of valence and conduction bands at this time instant [138, 152]. This can be explained by a significant difference between the electron and the hole effective masses  $m_h/m_e \sim 10$  and delayed electron-hole thermalization as a result.

This methodology allowing to trace overshooting on a picosecond time scale can be used further to study other narrow or near-narrow band gap semiconductors (Si, PbSe, PbTe, InAs). These materials must also satisfy the relation between thermalization and

<sup>5</sup>The predictions for 400 nm were obtained for the same FEL pulse parameters. Note that they cannot be directly compared to the experimental curve from Fig. 2b in [134]: according to Fig. 3a therein, it corresponds to a different set of FEL pump parameters.

| $F[\text{mJ}/\text{cm}^2]$ | $\tau_{el-latt}[\text{ps}]$ | $T_e^{init}[\text{eV}]$ |
|----------------------------|-----------------------------|-------------------------|
| 40                         | 2.0                         | 2.8                     |
| 20                         | 2.5                         | 2.2                     |
| 10                         | 3.0                         | 1.6                     |

**Table 4.1:** Model parameters iteratively adjusted to obtain predictions in Fig. 4.31a: thermalization time ( $\tau_{el-latt}$ ) and the free electron temperature at the minimum of  $\Delta R/R$  curve ( $T_e^{init}$ ). Table is reproduced from [138].

relaxation times:  $\tau_{el} \ll \tau_{e-h-latt} \ll \tau_{rec}$ .

Further reflectivity overshooting dynamics was observed and linked with band gap shrinkage in [157]. In the experiment made at the T-REX laboratory at Elettra (Trieste) silicon surfaces were highly excited below the melting transition by sapphire laser with a pump pulse at 800 nm. The estimate damage threshold in the experiment was  $F_{th} = 0.03 \text{ J}/\text{cm}^2$ . The characteristic overshooting was detected on a time scale of a few picoseconds, however with increasing fluence it took earlier to reach the overshooting. The reflectivity increase was linked with temperature increase also via rate equations while the decrease in dielectric constant due to an increased number of carriers was explained by the Drude model.

#### 4.4.2 Band separation in semiconductors

After the extension of the tight-binding based XTANT code towards electron-ion thermalization, we got an opportunity to observe transient reflectivity of GaAs on a picosecond time scale with this tool. In [98] the code has been for the first time applied to describe time evolution of X-ray excited GaAs. Fig. 4.32 shows the predictions obtained for GaAs at the absorbed dose of  $\sim 0.2 \text{ eV}/\text{atom}$ . This dose is much higher than the absorbed dose that we considered in the experiments by Gahl and Krupin ( $\sim 0.08 \text{ eV}/\text{atom}$ ). Yet, the timescale of the reflectivity overshooting  $\sim 15 \text{ ps}$  is much larger than that one observed in

both experiments at the lower dose.

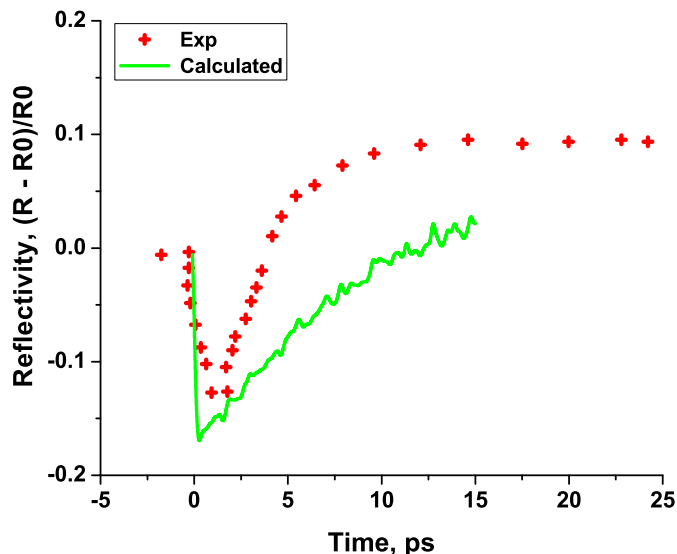


**Figure 4.32:** Transient reflectivity change of X-ray irradiated GaAs sample at 800 nm probe: (i) simulated by XTANT (solid green line) at photon energy  $\hbar\omega = 800$  eV, the absorbed dose = 0.2 eV/atom; (ii) measured experimentally in [135] (red points).

According to XTANT, the temperature of electrons at the end of cascading, i.e., at the minimum of the reflectivity curve, in experiments by Gahl (with fluence  $F = 4.1$  mJ/cm<sup>2</sup>) [134] and Krupin (with fluence  $F = 40$  mJ/cm<sup>2</sup>) [135], is  $\sim 0.4$  eV, whereas the one predicted with the Drude model is 2 – 3 eV. The crude estimate of the electronic temperature can be obtained from the average kinetic energy of a free electron within the conduction band  $E_{el}$ , neglecting the hole energy, with the relation:

$$E_{el} = E_{e-h} - E_{gap}, \quad (4.25)$$

where  $E_{e-h}$  is the average pair creation energy and  $E_{gap}$  is the band gap width. In GaAs  $E_{gap} = 1.42$  eV and  $E_{e-h} = 4.2$  eV, which gives a universal value of  $E_{el} = 2.78$  eV, and from the relation  $E_{el} = 3/2 k_B T_{el}$  it follows that  $T_{el} = 1.85$  eV.

The disagreement of the electronic temperatures can be explained by recalling the

specific band structure of GaAs. The direct band gap leads to the suppression of collisional interband processes as discussed above. However, the XTANT model intrinsically assumes an instantaneous mutual thermalization of electrons both in the conduction and in the valence band. The entire electronic system in low energy domain is then represented by a single Fermi-Dirac distribution with a global chemical potential and a global electron temperature which are updated with the simulation progress at each time step [5]. This assumption does not hold in case of GaAs. In this case the model has to be extended in order to account for the suppressed collisional exchange between the bands.

The simple approach to account for delayed interband thermalization is to equilibrate the bands separately by assuming independent thermalization of electrons in the conduction band with a specific electronic temperature  $T_c$  and chemical potential  $\mu_c$  and in the valence band with the temperature  $T_v$  and chemical potential  $\mu_v$  respectively. Such kind of approach was introduced, e.g., by van Driel [158] for silicon. Electrons in the conduction band and holes in the valence band were treated there with separate Fermi-Dirac distributions of different chemical potentials  $\mu_e$  and  $\mu_h$  respectively, but with a global temperature  $T_e$  and carrier density  $n$  [84, 158].

In order to separate interband thermalization in the framework of the XTANT model, we use a scheme analogous to the case of Fermi-Dirac distribution with a global chemical potential and a global electron temperature. At the first time step (before irradiation) we assume that the sample is in equilibrium, and calculate a global distribution function from the initial input parameters. Later, we follow separate Fermi-Dirac distributions for each band. Namely, we calculate Fermi distribution function for electrons in each band, by solving an inverse problem for a given number and energy of carriers within each band

as in Eq. (3.38), but with different energy levels boundaries:

$$\begin{aligned}
N_v^{low} &= \sum_{E_{min}}^{E_{bg}} f_v(E_i) = \sum_{E_{min}}^{E_{bg}} \frac{2}{1 + \exp((E_i - \mu_v)/T_v)}, \\
N_c^{low} &= \sum_{E_{bg+1}}^{E_{cut}} f_c(E_i) = \sum_{E_{bg+1}}^{E_{cut}} \frac{2}{1 + \exp((E_i - \mu_c)/T_c)}, \\
E_v^{low} &= \sum_{E_{min}}^{E_{bg}} E_i f_v(E_i) = \sum_{E_{min}}^{E_{bg}} \frac{2E_i}{1 + \exp((E_i - \mu_v)/T_v)}, \\
E_c^{low} &= \sum_{E_{bg+1}}^{E_{cut}} E_i f_c(E_i) = \sum_{E_{bg+1}}^{E_{cut}} \frac{2E_i}{1 + \exp((E_i - \mu_c)/T_c)}, \tag{4.26}
\end{aligned}$$

where  $E_{min}$  is the energy at the bottom of the valence band,  $E_{bg}$  is the energy at the top of the valence band, and  $E_{bg+1}$  is the energy at the bottom of the conduction band,  $E_{cut}$  is the high-energy cut-off ( $\sim 10$  eV). At each time step the XTANT code updates the information on the number of carriers and their energy in both bands. Using them, we calculate with the bisection method, applied for each band, the values of  $T_c$  and chemical potential  $\mu_c$  in the conduction band, and, in the valence band, the temperature  $T_v$  and the chemical potential  $\mu_v$  respectively at each time step.

With new values of distribution functions, we determine the global potential energy surface and then initiate a molecular dynamics calculation. The energy coming with the laser pulse is then redistributed between the bands. In case of inelastic scattering and energy loss by a high-energy electron we trace whether it remains in the high-energy domain or falls to the low-energy part of the conduction band. In this way, we trace the changes of carrier numbers and their energy in each band independently. Interband transitions are then naturally suppressed within the low-energy domain.

Similar to our earlier finding for silicon, the dynamical electron-phonon coupling scheme for GaAs starts being convergent at the MD time step  $\Delta t$  not longer than 0.01-0.02 fs, and such time step must be valid for the two-equilibrated-bands model as well. By employing the new model, we can trace the behaviour of temperatures and chemical potentials in both bands. Similarly, as in case of the global Fermi distribution model, after the peak of the pulse, a sharp increase in valence and conduction band electron temperatures is observed.

The peak value of the CB electron temperature  $T_c$  exceeds 2 eV both in simulations of Krupin's and Gahl's experiments (Fig. 4.33a, Fig. 4.33b), which is close to the value 1.85 eV estimated theoretically by Eq. (4.25). At the same time, the peak value of the VB electron temperature  $T_v$  is around 0.4 eV which is close to the global electron temperature estimate  $T_e = 0.42 - 0.43$  eV for the same simulation parameters, as there are much more electrons in the valence band and they provide the predominant contribution into the global electron temperature. The peak number of the created electron-hole pairs  $n_{e-h}$  per atom exceeds 2% which is also in agreement with the value  $n_{e-h}$  estimated by Eq. (4.19), which is about 2.2% in both experimental cases. This confirms that the extended XTANT model provides reliable results on the electron density and temperature.

During the electron-lattice thermalization process the CB electron temperature  $T_c$  decreases significantly on a time scale of 10-15 ps, in contrast to the VB electron temperature  $T_v$  which decreases very slowly. At the same time, the atomic temperature  $T_a$  rises from the initial value of 300 K only up to 600-700 K. As a result, the reflectivity coefficient decreases by  $\approx 10\%$  from the initial value at the temperature maximum which is as well in the agreement with the experiment, but later the reflectivity rises up very slowly and does not achieve overshooting in 10 ps (Fig. 4.34). However, knowing the energy absorbed from the pulse we can predict a final atomic temperature that the system would reach after the accomplished electron-lattice equilibration. In our case it would be 919 K for the conditions of Krupin's and Gahl's experiments. The predicted final value of the reflectivity change in both cases  $\Delta R/R$  is  $\sim 0.08$ , which is in agreement with Krupin's experiment as diffusion only slightly affects its results in contrast to Gahl's experiment.

These findings indicate that the proposed dynamical scheme for electron-phonon coupling, although successful for silicon and diamond, is not reliable in case of GaAs. As a result, our model underestimates the electron-ion coupling rate in GaAs which appears to be much smaller than in diamond and silicon. The reason for that might be the specific band structure of this material (with direct band gap). A possible improvement would require to go beyond the  $\Gamma$ -point approximation and to include multiple  $k$ -points in the evaluation of the coupling as it was performed, e.g., in [159].

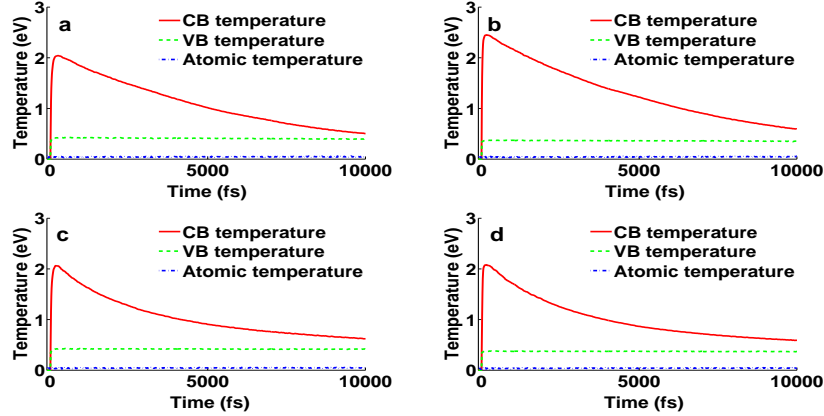


**Figure 4.33:** Transient conduction band electron temperature (solid red line), valence band electron temperature (dashed green line) and atomic temperature (dot-dashed blue line) simulated with  $\Delta t = 0.02$  fs MD time step for: a) Gahl’s experiment, dynamical coupling; b) Krupin’s experiment, dynamical coupling; c) Gahl’s experiment, FGR coupling; d) Krupin’s experiment, FGR coupling. The pulse fluence  $F = 4.1$  mJ/cm<sup>2</sup> for Gahl’s experiment,  $F = 40$  mJ/cm<sup>2</sup> for Krupin’s experiment.

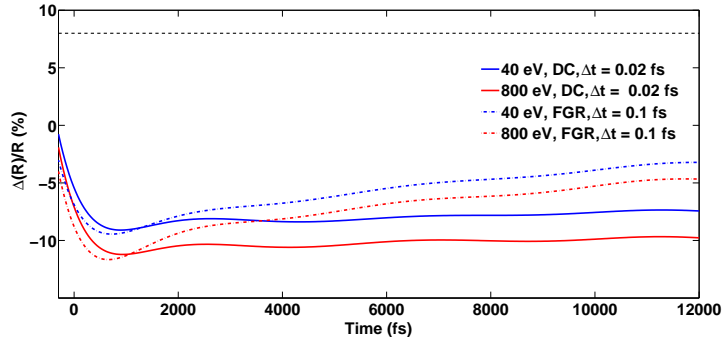


**Figure 4.34:** Time dependence of the reflectivity change simulated with dynamical coupling (solid lines) at  $\Delta t = 0.02$  fs MD time step and with FGR (dot-dashed lines) at  $\Delta t = 0.1$  fs for Gahl’s experiment ( $\hbar\omega = 40$  eV, blue lines) and Krupin’s experiment ( $\hbar\omega = 800$  eV, red lines). The pulse fluence  $F = 4.1$  mJ/cm<sup>2</sup> for Gahl’s experiment,  $F = 40$  mJ/cm<sup>2</sup> for Krupin’s experiment. The black dashed line denotes the reflectivity coefficient, which must be observed after full electron-lattice equilibration.

To illustrate that the electron-lattice equilibration and the reflectivity overshooting are principally achievable in a framework of the current model under condition of a correct electron-phonon coupling treatment, we performed simulations at the larger MD time step  $\Delta t = 0.1$  fs (Fig. 4.35a, Fig. 4.35b) which artificially increases the rate of electron-ion coupling. As we know from our previous studies, this time step is sufficient for MD convergence but too large for the convergence of electron-ion coupling rate. The increase of the coupling rate shortens the interband thermalization time scale.

After reaching the equilibrium temperature and equilibrium chemical potential in both bands, we switched back to the global Fermi distribution, assuming that the interband equilibration already occurred. Since the collisional electron transitions between the bands are then again permitted, the number of electrons in the conduction band starts to decrease. The larger time step affects the reflectivity coefficient, and, although the experimentally observed overshooting, starting after  $\sim 5$  ps and saturating at  $\sim 10$  ps, could not be reproduced, the reflectivity coefficient rises back to its initial value faster, when compared to the case of the MD time step  $\Delta t = 0.02$  fs with DC approach.

The FGR tested with  $\Delta t = 0.02$  fs (Fig. 4.33c, Fig. 4.33d) does not give the observable difference in the bands equilibration time scale compared with the DC at the same time step. However, at  $\Delta t = 0.1$  fs the FGR (Fig. 4.35c, Fig. 4.35d) provides significantly faster bands equilibration compared with the DC, as was discussed in Subsection 4.3.3. The overshooting with FGR at  $\Delta t = 0.1$  fs is still not observed in both cases at 10 ps, although the growth of the reflectivity by  $\sim 5\%$  from the minimum value can be detected (Fig. 4.34). Let us note that the FGR scheme is inherently divergent in this regime (i.e., for any time step chosen) [76]. We show the predictions obtained with Fermi's Golden Rule scheme for purely illustrative purpose.

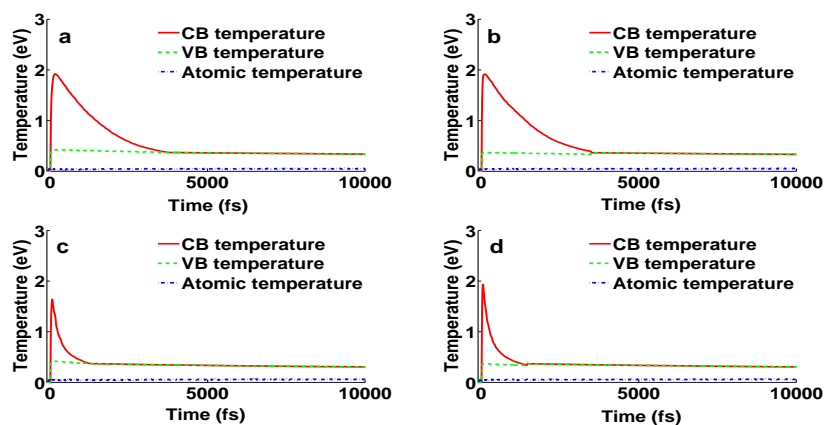


**Figure 4.35:** Transient conduction band electron temperature (solid red line), valence band electron temperature (dashed green line) and atomic temperature (dot-dashed blue line) simulated with  $\Delta t = 0.1$  fs MD time step for: a) Gahl's experiment ( $\hbar\omega = 40$  eV), dynamical coupling; b) Krupin's experiment ( $\hbar\omega = 800$  eV), dynamical coupling; c) Gahl's experiment, FGR coupling; d) Krupin's experiment, FGR coupling. The pulse fluence  $F = 4.1$  mJ/cm<sup>2</sup> for Gahl's experiment,  $F = 40$  mJ/cm<sup>2</sup> for Krupin's experiment.

# Chapter 5

## Conclusions and outlook

### 5.1 Conclusions

In this work, we studied the interplay between transient structural modifications and optical properties in several FEL-excited semiconductors. It gave us an opportunity to follow the transient optical coefficients related to the non-equilibrium dynamics within the irradiated materials. Thus, we can compare our theoretical predictions with the results of the modern time-resolved experiments at FEL facilities that often involve measurements of optical coefficients. Two models have been used: an extension of the hybrid calculation tool XTANT for C, Si and GaAs, and a unified model based on rate equations and Drude theory which was only used for GaAs to estimate the electron-lattice thermalization effects in it. The molecular dynamics calculations with XTANT are based on the transferable tight-binding method, and thus, the model takes an intermediate place between *ab initio* approaches and empirical methods, as a 'compromise' solution fulfilling the accuracy and the computational efficiency requirements. The model also employs Monte Carlo scheme in the part treating kinetics of high-energy electrons in the conduction band and deep shell holes in the valence band whose density is relatively small in case of XUV and soft X-ray pulses. The rest (low-energy) electrons are distributed on the tight-binding energy levels and their occupation numbers are determined by the Boltzmann equation. This set of

approaches makes the model self-consistent. Typically, electron excitation and thermalization occur within a few hundred femtoseconds. At later times, we trace the electron-lattice equilibration via nonadiabatic approach until the diffusion and transport effects start to dominate. Thus, we are able to describe the response of semiconductors to the irradiation in terms of optical properties accurately enough on a time scale of  $\sim 10$  ps. The calculation of the dielectric function and transient optical properties is based on the Lindhard theory within the random phase approximation, where the necessary momentum matrix elements are taken from the tight-binding Hamiltonian.

The results of our simulations indicate that optical properties reflect the changes of the atomic structure of the materials. As optical properties (such as transmission and reflectivity) are standard experimental observables, it makes them good indicators of phase transformations. Thus, from the available experimental results, we can retrieve information on the phase transitions in irradiated materials. Our method described the following phenomena: ultrafast non-thermal graphitization of diamond, thermal and non-thermal melting of silicon. In addition, the connection of the reflectivity overshooting in GaAs with the band gap shrinking, caused by the electron-lattice thermalization, was demonstrated by the XTANT model together with the unified model from [138]. The simulation indicated a novel opportunity to measure the electron-phonon coupling rate in semiconductors from the optical properties.

The studied ultrafast non-thermal graphitization of diamond is one of the fastest known phase transition which may occur within 100-150 fs, i.e., still during the action of the ultrashort FEL pulses. The validity of our model for the description of optical coefficients in non-equilibrium carbon was established by comparing the simulation results for reflectivity with the results acquired in the experiment by Reitze et al [96]. We also proved the inapplicability of the ordinary Drude model (without interband transitions) to describe the optical properties in non-equilibrium systems excited above the damage threshold. A previously established graphitization threshold dose of 0.7 eV/atom was confirmed. Finally, the results produced by our model were found to be in an excellent agreement with the experimental results from a recent time-resolved non-thermal graphitization experiment on

FERMI@Elettra facility, in which time-resolved transmission was utilized as the signature of the transition.

Melting of silicon has two possible transition channels dependent on the absorbed dose: thermal and non-thermal. In the case of a dose over the non-thermal threshold, both channels may be involved. When the thermal melting dominates, optical properties relax on a longer time scale ( $\sim 1$  ps), than in case when non-thermal effects dominate ( $\sim 100$  fs). In other words, the changes of the optical properties are smoother during thermal melting. We analyzed the melting of silicon for different doses and found that the formation of the high-density liquid phase (HDL) is predominantly connected with the non-thermal melting, while the low-density liquid phase (LDL) can be an outcome of solely thermal melting. The estimated doses of 0.65 eV/atom and 0.9 eV/atom for LDL and HDL phases found their confirmation in an experiment. The model was tested against the reflectivity data from the Sokolowski-Tinten's et al. experiment [109] and showed a good agreement with it.

Gallium arsenide is a popular and widely studied compound nowadays. It has applications for FEL pulse diagnostics as a timing tool [134]. The transient changes of reflectivity were measured in experiments by Gahl et al. [134] with XUV photons and by Krupin et al. [135] with soft X-ray photons. In both experiments, the transient optical reflectivity showed an ultrafast drop in less than 1 ps and a subsequent recovery to its initial value, with an eventual overshooting of its initial value within a few picoseconds. After reaching the maximum of electron-hole density at the minimum of the reflectivity curve the system starts to relax predominantly by electron-lattice thermalization, increasing the lattice temperature. The evolution of the electron temperature and the lattice temperature was treated by two-temperature model which is coupled with rate equations and the Drude model that follows the transient reflectivity. The combination of schemes forms a unified model [138] that we used for tracing the evolution of optical properties in irradiated semiconductors. The model results reproduce the behaviour of the transient reflectivity curve within few tens of picoseconds. The model confirms that the reflectivity overshooting is a result of the band gap shrinking during the lattice heating. At the same time, the overshooting is a signature of electron lattice thermalization, and the time scale of its

emergence is essentially a time scale of the electron-lattice thermalization. Independently, we also used the XTANT model, which did not reproduce the overshooting effect on a time scale considered in the experiment. The evaluated temperature of the conduction band electrons  $T_c$  and the electron-hole density  $n_{e-h}$  at the end of the electron thermalization were far from the estimates made with the unified model. Further extension of the XTANT towards a separate treatment of valence and conduction bands was made in order to account for the specific properties of GaAs. It allowed to obtain the values of  $T_c$  and  $n_{e-h}$  which are close to the estimates of the unified model [138]. Furthermore, we identified the reason for the disagreement between XTANT predictions and experimental data on the reflectivity change of GaAs at picosecond time scales which is due to a too low electron-ion coupling rate implemented.

## 5.2 Outlook

The presented research emphasized the importance of optical properties based on the dielectric function as sensitive tools to detect structural transitions in semiconductors. Altogether, it is clear that in this field there is still a very large space for future developments. Let us make an outlook of future developments related to our work and to the simulations of ultrafast FEL induced processes in solids. First, we clearly see the necessity of employing more universal techniques with less fitted and preadjusted parameters for every single element or compound. It predetermines our way to ab initio modeling, such as, e.g., XMOLECULE which was described in Subsection 2.5.2. This does not mean that we should completely decline the semi-empirical tight-binding paradigm, – rather we should combine efficient features of both approaches. For example, in the current version, interatomic forces are calculated with the Hellmann-Feynman theorem [5, 18] by taking the derivatives of the potential energy surface. However, the Hellmann-Feynman theorem works accurately for self-consistent field (SCF) in the limit of a complete basis set [160]. In case of a finite number of basis set functions, Pulay forces [161] must be calculated as corrections to the Hellmann-Feynman forces. Then, the Hartree-Fock energy expression

should be derived in order to get the Hellmann-Feynman force together with the Pulay force, i.e., the explicit forms of wave functions are needed, and this leads to a usage of an ab initio approach.

The currently implemented scheme for the calculation of CDF and correspondingly the electron scattering cross sections is another issue that can be improved. The obvious way to do it implies again the adoption of first principles techniques. One of the possible routes includes a usage of the linear response and plasma density fluctuations theories. In this framework, the linear plasma susceptibility  $\chi(\mathbf{k}, \omega)$  can be determined by the Fourier components of an external potential  $\phi_{\text{ext}}(\mathbf{k}, \omega)$  and the ensemble averaged electron density fluctuation  $\langle n_{\text{ind}}(\mathbf{k}, \omega) \rangle$  [162, 163]:

$$\chi(\mathbf{k}, \omega) = \frac{\langle n_{\text{ind}}(\mathbf{k}, \omega) \rangle}{-e\phi_{\text{ext}}(\mathbf{k}, \omega)}. \quad (5.1)$$

Then with the complex dielectric function  $\varepsilon(\mathbf{k}, \omega)$ , which is linked with the susceptibility as

$$\frac{1}{\varepsilon(\mathbf{k}, \omega)} = 1 + \frac{4\pi e^2}{k^2} \chi(\mathbf{k}, \omega), \quad (5.2)$$

the dynamic structure factor  $S(\mathbf{k}, \omega)$  (which in turn is related to the scattering cross section) can be related via fluctuation-dissipation theorem as [66, 162, 163]:

$$S(\mathbf{k}, \omega) = -\frac{\hbar k^2 \Omega}{2\pi e^2 (1 - e^{-\beta\hbar\omega})} \text{Im} \frac{1}{\varepsilon(\mathbf{k}, \omega)}, \quad (5.3)$$

where  $\Omega$  is a plasma volume,  $\beta = 1/k_b T$ . The elastic ( $\omega = 0$ ) and inelastic ( $\omega \neq 0$ ) scattering cross sections can then be obtained for  $S(\mathbf{k}, \omega)$  with such a scheme. It means that one would not employ any fitting parameters and functions, as it is realized now with Ritchie and Howie method, and could obtain cross section estimates out of equilibrium.

Another possibility to extend the borders of the TB-based model implicates the usage of the Boltzmann transport equation for the description of statistical behaviour of the system in non-equilibrium state. This approach is intended to replace the Fermi distribution and temperature equation in the current scheme that assumes instant equilibration of electrons in the system by transient non-equilibrium electron distribution. So far, already electron-ion collision Boltzmann integral has been involved in the model.

In Section 3.3, we discussed, that the tight-binding based model does not work at high fluences, as TB parametrization describes only the lowest levels of the conduction band. At high irradiation doses, the electrons occupy the upper levels of the conduction band, but, according to the model, the electrons must be thermally distributed within the bands available within the model to form the Fermi distribution. The temperature and chemical potential which are arguments of the distributions are underestimated in such a model. Moreover, a large relative value of the conduction band electrons or core holes can lead to significant charge effects, not captured by the quasi-neutral TB approach.

In general, tracing of X-ray induced structural dynamics by means of optical properties has a great potential from both theoretical and experimental point of view. The currently existing experimental tools are continuously upgraded, and besides, new experimental developments such as tabletop X-ray lasers [164, 165] are very promising in terms of simplicity, efficiency and increase in number of experiments in the field. The commissioning of European XFEL will also open a door to experiments with extremely brilliant coherent short pulses with a high repetition rate (27 000 flashes per second [9]).

# Appendix A

## Verlet algorithm

One of the most popular methods of integrating the equations of motion in molecular dynamics was developed by Verlet [74, 166]. The second order equation of motion looks as follows:

$$\mathbf{f}_i = m_i \ddot{\mathbf{r}}_i, \quad (\text{A.1})$$

where  $m_i$  is a mass of a particle  $i$ ,  $\mathbf{r}_i$  is a Cartesian coordinate of a particle,  $\mathbf{f}_i$  is a total force acting on a particle. After the Taylor expansions, the coordinate functions  $\mathbf{r}$  at time instant  $t + \delta t$  and  $t - \delta t$  can be read as:

$$\begin{aligned} \mathbf{r}(t + \delta t) &= \mathbf{r}(t) + \delta t \dot{\mathbf{r}}(t) + (1/2) \delta t^2 \ddot{\mathbf{r}}(t) + \dots, \\ \mathbf{r}(t - \delta t) &= \mathbf{r}(t) - \delta t \dot{\mathbf{r}}(t) + (1/2) \delta t^2 \ddot{\mathbf{r}}(t) + \dots \end{aligned} \quad (\text{A.2})$$

Summation of these equations gives us:

$$\mathbf{r}(t + \delta t) = 2\mathbf{r}(t) - \mathbf{r}(t - \delta t) + \delta t^2 \ddot{\mathbf{r}}(t). \quad (\text{A.3})$$

The velocity  $\mathbf{v} = \dot{\mathbf{r}}(t)$  can then be expressed by deducting one of Eq. (A.2) from another and neglecting terms of order  $\delta t^4$ :

$$\mathbf{v}(t) = \frac{\mathbf{r}(t + \delta t) - \mathbf{r}(t - \delta t)}{2\delta t}. \quad (\text{A.4})$$

The modification of this algorithm made by Hockney and Potter [167, 168] includes the calculation of the mid-step velocity  $\mathbf{v}(t - 1/2\delta t)$ . Another, more stable option, which is

called Verlet-algorithm in the velocity form, is found by taking coordinate  $\mathbf{r}$  at the time step  $t + 2\delta t$  and velocity  $\mathbf{v}$  at the time step  $t + \delta t$ :

$$\mathbf{r}(t + 2\delta t) = 2\mathbf{r}(t + \delta t) - \mathbf{r}(t) + \delta t^2 \ddot{\mathbf{r}}(t), \quad (\text{A.5})$$

$$\mathbf{v}(t + \delta t) = \frac{\mathbf{r}(t + 2\delta t) - \mathbf{r}(t)}{2\delta t}. \quad (\text{A.6})$$

Then by inserting Eq. (A.5) and the first of Eqs. (A.2) into Eq. (A.6) we get:

$$\mathbf{v}(t + \delta t) = \mathbf{v}(t) + \delta t \frac{\ddot{\mathbf{r}}(t) + \ddot{\mathbf{r}}(t + \delta t)}{2}. \quad (\text{A.7})$$

The final expressions, after marking  $\ddot{\mathbf{r}}$  as the acceleration  $\mathbf{a}$ , take the following form:

$$\begin{aligned} \mathbf{r}(t + \delta t) &= \mathbf{r}(t) + \delta t \mathbf{v}(t) + 1/2 \delta t^2 \mathbf{a}(t), \\ \mathbf{v}(t + \delta t) &= \mathbf{v}(t) + 1/2 \delta t [\mathbf{a}(t) + \mathbf{a}(t + \delta t)]. \end{aligned} \quad (\text{A.8})$$

# Appendix B

## Ehrenfest approximation in calculation of potential energy surface

As it was stated in Chapter 3, knowing transient occupation numbers and energy levels of the irradiated material, we can calculate the potential energy surface (PES) as in Eq. (3.31) with an additional repulsion term. In our hybrid model we apply the Ehrenfest approximation which means that the electronic states are populated with an average electronic distribution and the PES is evaluated through averaging of all possible PES corresponding to the Fermi function [103]. The interatomic forces are calculated as the gradients of the PES. If the PES are parallel, then the forces are not sensitive to the electrons hopping between the different surfaces.

In order to check, whether the PES that we obtain fulfills the requirements of the Ehrenfest approximation, we constructed the PES (Fig. B.1) for different number of electrons in diamond promoted to the conduction band during its irradiation with a dose of 0.85 eV/atom, i.e. above the graphitization threshold. The photon energy  $\hbar\omega$  of the FEL pulse in the simulation was 10 keV, the pulse duration  $\tau$  was 10 fs and the supercell contained 64 atoms. The diamond turned into graphite on a time scale of 100-150 fs, and, until that, the PES were almost parallel to each other. The average Fermi distribution curve crossed all of them, according to the Ehrenfest-like dynamic assumption. On a later time scale,

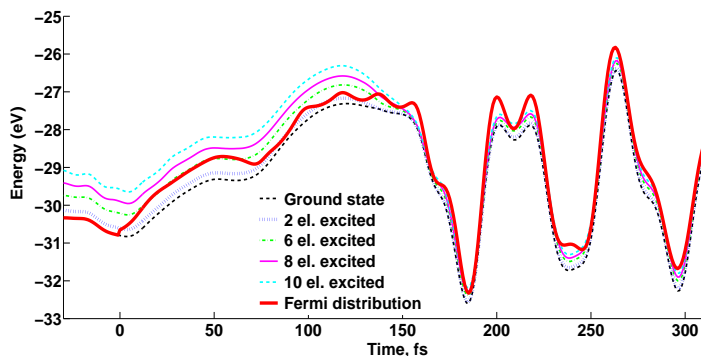


**Figure B.1:** Time evolution of the potential energy surfaces of diamond irradiated above the graphitization threshold. FEL pulse photon energy was  $\hbar\omega = 10$  keV, pulse duration  $\tau = 10$  fs, absorbed dose = 0.85 eV/atom. 64 atoms were in the simulated supercell. The curves represent potential energy surfaces for the ground state of diamond and for different numbers of electrons excited to the conduction band. The red bold curve stands for the transient potential energy surface calculated with Fermi distribution on the trajectory leading to graphitization.

some crossings between potential energy surfaces could be found, but, by that time, the system had already turned into graphite and the dynamical pathway for the system had been already chosen [103]. Thus, the Ehrenfest-like dynamics is applicable in our model and the averaging over the population of electronic states can be adopted.

# Appendix C

## Tight-binding parameters

The tight-binding parameters for carbon and silicon used in Eq. (3.25) and Eq. (3.30) are listed in the following Tables C.1 and C.2 respectively. The Hamiltonian from Eq. (3.25) is the symmetric matrix which consists of  $(4 \times 4)$ -matrix blocks, as there are 4 orbitals in  $sp^3$  basis set. The diagonal and off-diagonal blocks of Hamiltonian matrix look as follows:

$$H_{ii} = \begin{pmatrix} \epsilon_s & 0 & 0 & 0 \\ 0 & \epsilon_p & 0 & 0 \\ 0 & 0 & \epsilon_p & 0 \\ 0 & 0 & 0 & \epsilon_p \end{pmatrix}, \quad H_{ij} = \begin{pmatrix} t_{ij}^{ss} & t_{ij}^{sp_x} & t_{ij}^{sp_y} & t_{ij}^{sp_z} \\ -t_{ij}^{sp_x} & t_{ij}^{p_x p_x} & t_{ij}^{p_x p_y} & t_{ij}^{p_x p_z} \\ -t_{ij}^{sp_y} & t_{ij}^{p_x p_y} & t_{ij}^{p_y p_y} & t_{ij}^{p_y p_z} \\ -t_{ij}^{sp_z} & t_{ij}^{p_x p_z} & t_{ij}^{p_y p_z} & t_{ij}^{p_z p_z} \end{pmatrix}. \quad (\text{C.1})$$

For GaAs, the TB scheme with  $sp^3s^*$  basis set has been adopted. Therefore the Hamiltonian matrix will contain  $(5 \times 5)$ -blocks (Eq. C.2). The tight-binding parameters of GaAs are listed in Table C.3.

$$H_{ii} = \begin{pmatrix} \epsilon_s & 0 & 0 & 0 & 0 \\ 0 & \epsilon_p & 0 & 0 & 0 \\ 0 & 0 & \epsilon_p & 0 & 0 \\ 0 & 0 & 0 & \epsilon_p & 0 \\ 0 & 0 & 0 & 0 & \epsilon_{s^*} \end{pmatrix}, \quad H_{ij} = \begin{pmatrix} t_{ij}^{ss} & t_{ij}^{sp_x} & t_{ij}^{sp_y} & t_{ij}^{sp_z} & t_{ij}^{ss^*} \\ -t_{ij}^{sp_x} & t_{ij}^{p_x p_x} & t_{ij}^{p_x p_y} & t_{ij}^{p_x p_z} & t_{ij}^{p_x s^*} \\ -t_{ij}^{sp_y} & t_{ij}^{p_x p_y} & t_{ij}^{p_y p_y} & t_{ij}^{p_y p_z} & t_{ij}^{p_y s^*} \\ -t_{ij}^{sp_z} & t_{ij}^{p_x p_z} & t_{ij}^{p_y p_z} & t_{ij}^{p_z p_z} & t_{ij}^{p_z s^*} \\ t_{ij}^{ss^*} & t_{ij}^{p_x s^*} & t_{ij}^{p_y s^*} & t_{ij}^{p_z s^*} & t_{ij}^{s^* s^*} \end{pmatrix}. \quad (\text{C.2})$$

**Table C.1:** Tight-binding parameters of carbon used in the model taken from [169].  $r_0 = 1.536329 \text{ \AA}$ ,  $n = 2$ ,  $r_1 = 2.45 \text{ \AA}$ ,  $r_m = 2.6 \text{ \AA}$ . The on-site energies of the orbitals were:  $\epsilon_s = -2.99 \text{ eV}$ ,  $\epsilon_p = 3.71 \text{ eV}$ .

| Electronic parameters          |                               |            |            |         |
|--------------------------------|-------------------------------|------------|------------|---------|
| $\xi$                          | $ss\sigma$                    | $sp\sigma$ | $pp\sigma$ | $pp\pi$ |
| $r_c \text{ [\AA]}$            | 2.18                          | 2.18       | 2.18       | 2.18    |
| $n_c$                          | 6.5                           | 6.5        | 6.5        | 6.5     |
| $V_\xi^0 \text{ [eV]}$         | -5.0                          | 4.7        | 5.5        | -1.55   |
| Repulsive potential parameters |                               |            |            |         |
| $\phi_0 \text{ [eV]}$          | 8.18555                       |            |            |         |
| $m$                            | 3.30304                       |            |            |         |
| $m_c$                          | 8.6655                        |            |            |         |
| $d_0 \text{ [\AA]}$            | 1.64                          |            |            |         |
| $d_c \text{ [\AA]}$            | 2.1052                        |            |            |         |
| $a_0$                          | -2.590976512                  |            |            |         |
| $a_1 \text{ [eV]}$             | 0.573115150                   |            |            |         |
| $a_2 \text{ [eV]}$             | $-1.78963499 \times 10^{-3}$  |            |            |         |
| $a_3 \text{ [eV]}$             | $2.353922152 \times 10^{-5}$  |            |            |         |
| $a_4 \text{ [eV]}$             | $-1.242511696 \times 10^{-7}$ |            |            |         |

**Table C.2:** Tight-binding parameters of silicon used in the model taken from [170].  $r_0 = 2.360352$  Å,  $n = 2$ ,  $r_1 = 4.0$  Å,  $r_m = 4.16$  Å. The on-site energies of the orbitals were:  $\epsilon_s = -5.25$  eV,  $\epsilon_p = 1.20$  eV.

| Electronic parameters          |                             |             |             |          |
|--------------------------------|-----------------------------|-------------|-------------|----------|
| $\xi$                          | ss $\sigma$                 | sp $\sigma$ | pp $\sigma$ | pp $\pi$ |
| $r_c$ [Å]                      | 3.5                         | 3.55        | 3.7         | 3.7      |
| $n_c$                          | 9.5                         | 8.5         | 7.5         | 7.5      |
| $V_\xi^0$ [eV]                 | -2.038                      | 1.745       | 2.75        | -1.075   |
| Repulsive potential parameters |                             |             |             |          |
| $\phi_0$ [eV]                  | 1.0                         |             |             |          |
| $m$                            | 6.8755                      |             |             |          |
| $m_c$                          | 13.017                      |             |             |          |
| $d_0$ [Å]                      | 2.360352                    |             |             |          |
| $d_c$ [Å]                      | 3.66995                     |             |             |          |
| $a_0$                          | 0.0                         |             |             |          |
| $a_1$ [eV]                     | 2.1604385                   |             |             |          |
| $a_2$ [eV]                     | -0.1384393                  |             |             |          |
| $a_3$ [eV]                     | $5.8398423 \times 10^{-3}$  |             |             |          |
| $a_4$ [eV]                     | $-8.0263577 \times 10^{-5}$ |             |             |          |

**Table C.3:** Tight-binding parameters of GaAs used in the model taken from [70]. The on-site energies of the orbitals were:  $\epsilon_s = -2.657$  eV,  $\epsilon_p = 3.669$  eV,  $\epsilon_{s^*} = 6.739$  eV;  $r_c = 3.511$  Å,  $n_c = 13.0$ .

| Electronic parameters          |            |            |            |         |        |        |
|--------------------------------|------------|------------|------------|---------|--------|--------|
| $\xi$                          | $ss\sigma$ | $sp\sigma$ | $pp\sigma$ | $pp\pi$ | $s^*p$ | $ss^*$ |
| $V_\xi^0$ [eV]                 | -1.613     | 2.504      | 3.028      | -0.781  | 2.082  | 0      |
| Repulsive potential parameters |            |            |            |         |        |        |
| $\Phi_1$ [eV]                  | 2.3906     |            |            |         |        |        |
| $\Phi_2$ [eV]                  | 1.2347     |            |            |         |        |        |
| $\alpha$ [Å]                   | 0.3555     |            |            |         |        |        |

# Appendix D

## Cross sections for inelastic electron scattering

The parameters used in the model functions for the determination of the imaginary part of the inverse complex dielectric function (the so-called loss function) in Eq. (3.21) are listed in Tables D.1, D.2 and D.3.

**Table D.1:** Coefficients of the CDF for the electron inelastic scattering in carbon.

| Shell        | $i$ | $E_{0i}[\text{eV}]$ | $A_i$ | $\gamma_i$ |
|--------------|-----|---------------------|-------|------------|
| K            | 1   | 250.0               | 480   | 200        |
| Valence band | 1   | 22.3                | 17    | 2          |
|              | 2   | 24.5                | 25    | 4          |
|              | 3   | 29.2                | 185   | 5.5        |
|              | 4   | 32.0                | 29    | 4          |
|              | 5   | 35.0                | 221   | 11         |
|              | 6   | 47.0                | 505   | 37         |

**Table D.2:** Coefficients of the CDF for the electron inelastic scattering in silicon.

| Shell        | $i$ | $E_{0i}$ [eV] | $A_i$     | $\gamma_i$ |
|--------------|-----|---------------|-----------|------------|
| K            | 1   | 1579.84393    | 236.1525  | 1192.8108  |
| L1           | 1   | 219.31853     | 223.14459 | 199.22160  |
| L2           | 1   | 100           | 685       | 145        |
| Valence band | 1   | 15.9504       | 113.883   | 3.212      |
|              | 2   | 17.499583     | 135.1805  | 3.0291     |

**Table D.3:** Coefficients of the CDF for the electron inelastic scattering in GaAs.

| Shell     | $i$ | $E_{0i}$ [eV] | $A_i$ | $\gamma_i$ |
|-----------|-----|---------------|-------|------------|
| <b>Ga</b> |     |               |       |            |
| K         | 1   | 10000         | 60    | 7000       |
| L1        | 1   | 1200          | 55    | 1300       |
| L2        | 1   | 1000          | 105   | 750        |
| L3        | 1   | 1020          | 280   | 1200       |
| M1        | 1   | 225           | 20    | 210        |
| M2        | 1   | 230           | 32    | 320        |
|           | 2   | 105           | 5     | 1          |
|           | 3   | 550           | 5     | 550        |
| M3        | 1   | 235           | 75    | 320        |
|           | 2   | 105           | 1     | 1          |
| M4        | 1   | 250           | 50    | 500        |
|           | 2   | 80            | 160   | 110        |
| M5        | 1   | 76            | 217   | 100        |
|           | 2   | 200           | 140   | 500        |

| <b>As</b>    |   |       |      |      |
|--------------|---|-------|------|------|
| K            | 1 | 14000 | 50   | 8000 |
| L1           | 1 | 1300  | 110  | 3700 |
| L2           | 1 | 1000  | 105  | 750  |
| L3           | 1 | 1020  | 130  | 1300 |
| M1           | 1 | 240   | 28   | 300  |
| M2           | 1 | 250   | 28   | 300  |
|              | 2 | 500   | 3    | 300  |
|              | 3 | 600   | 10   | 550  |
| M3           | 1 | 260   | 70   | 320  |
|              | 2 | 500   | 30   | 200  |
| M4           | 1 | 300   | 140  | 600  |
|              | 2 | 115   | 135  | 120  |
| M5           | 1 | 123   | 260  | 130  |
|              | 2 | 300   | 40   | 5000 |
| Valence band | 1 | 16    | 65   | 6.5  |
|              | 2 | 30    | 3    | 21   |
|              | 3 | 3.7   | 0.1  | 1    |
|              | 4 | 14    | 10.5 | 2    |
|              | 5 | 10    | 13   | 3    |
|              | 6 | 12    | 2    | 1    |

# Bibliography

- [1] P. Emma et al. First lasing and operation of an angstrom-wavelength free-electron laser. *Nat. Photonics*, 4(9):641–647, 2010.
- [2] D. Pile. X-rays: First light from SACLA. *Nat. Photonics*, 5:456, 2011.
- [3] E. Allaria et al. Highly coherent and stable pulses from the FERMI seeded free-electron laser in the extreme ultraviolet. *Nat. Photonics*, 6:699–704, 2012.
- [4] W. Ackermann et al. Operation of a free-electron laser from the extreme ultraviolet to the water window. *Nat. Photonics*, 1:336–342, 2007.
- [5] N. Medvedev, H.O. Jeschke, and B. Ziaja. Nonthermal phase transitions in semiconductors induced by a femtosecond extreme ultraviolet laser pulse. *New J. Phys.*, 15:015016, 2013.
- [6] I. Grguraš et al. Ultrafast x-ray pulse characterization at free-electron lasers. *Nat. Photonics*, 6:852–857, 2012.
- [7] Y. Ding et al. Measurements and simulations of ultralow emittance and ultrashort electron beams in the Linac Coherent Light Source. *Phys. Rev. Lett.*, 102:254801, 2009.
- [8] B.D. Patterson et al. Coherent science at the SwissFEL x-ray laser. *New J. Phys.*, 12:035012, 2010.
- [9] M. Altarelli et al. XFEL Technical Design Report, DESY 2006-097, Hamburg.

- [10] J. Rönsch-Schulenburg et al. Operation of FLASH with short SASE-FEL radiation pulses. *Proc. of FEL2014*, pages 342–345, 2014.
- [11] P. Finetti et al. Pulse duration in seeded free-electron lasers. *Accepted in Phys. Rev. X*, 2017.
- [12] G.R. Fleming. *Chemical Applications of Ultrafast Spectroscopy (International Series of Monographs on Chemistry)*. Oxford University Press, Clarendon Press, 1986.
- [13] S. Savikhin. Shot-noise-limited detection of absorbance changes induced by subpicosecond laser pulses in optical pump-probe experiments. *Rev. Sci. Instrum.*, 66:4470, 1995.
- [14] E. Allaria et al. Two-colour pump-probe experiments with a twin-pulse-seed extreme ultraviolet free-electron laser. *Nat. Commun.*, 4:2476, 2013.
- [15] A. Senftleben et al. Investigating temporal structure of FEL pulses by XUV pump-probe autocorrelation measurements. *J. Phys.: Conf. Ser.*, 388:032011, 2012.
- [16] A.A. Lutman et al. Experimental demonstration of femtosecond two-color x-ray free-electron laser. *Phys. Rev. Lett.*, 110:134801, 2013.
- [17] A.S. Ilyushin and A.P. Oreshko. *Vvedenie v difraktsionnyi strukturnyi analiz (Introduction into the diffractive structural analysis)*. MGU: Fizicheskii fakul'tet Moskva, 2008.
- [18] H.O. Jeschke. *Theory for Optically Created Nonequilibrium in Covalent Solids*. PhD thesis, Freie Universität Berlin, 2000.
- [19] P. Kleinert. Theory of hot-electron quantum diffusion in semiconductors. *Phys. Reports*, 485:1–42, 2010.
- [20] N. Medvedev, H.O. Jeschke, and B. Ziaja. Nonthermal graphitization of diamond induced by a femtosecond x-ray laser pulse. *Phys. Rev. B*, 88:224304, 2013.

- [21] N. Medvedev, Z. Li, and B. Ziaja. Thermal and nonthermal melting of silicon under femtosecond x-ray irradiation. *Phys. Rev. B*, 91:054113, 2015.
- [22] T. Maltezopoulos et al. Single-shot timing measurement of extreme-ultraviolet free-electron laser pulses. *New J. Phys.*, 10:033026, 2008.
- [23] M. Harmand et al. Achieving few-femtosecond time-sorting at hard x-ray free-electron. *Nat. Photonics.*, 7:215, 2013.
- [24] R. Riedel et al. Single-shot pulse duration monitor for extreme ultraviolet and x-ray free-electron lasers. *Nat. Commun.*, 4:1731, 2013.
- [25] J.P. Mathieu. *Optics*. Pergamon Press, Oxford, 1975.
- [26] P. Yeh. *Optical Waves in Layered Media*. Wiley, 2005.
- [27] V. Tkachenko et al. Transient optical properties of semiconductors under femtosecond x-ray irradiation. *Phys. Rev. B*, 93:144101, 2016.
- [28] J.P. Callan. *Ultrafast Dynamics and Phase Changes in Solids Excited by Femtosecond Laser Pulses*. PhD thesis, Harvard University, 2000.
- [29] J. Shah et al. Determination of intervalley scattering rates in GaAs by subpicosecond luminescence spectroscopy. *Phys. Rev. Lett.*, 59:2222, 1987.
- [30] E.N. Glezer, Y. Siegal, L. Huang, and E. Mazur. Behavior of  $\chi^{(2)}$  during a laser-induced phase transition in GaAs. *Phys. Rev. B*, 51:9589, 1995.
- [31] R.T. Willis, F.E. Becerra, L.A. Orozco, and S.L. Rolston. Four-wave mixing in the diamond configuration in an atomic vapor. *Phys. Rev. A*, 79:033814, 2009.
- [32] F. Bencivenga et al. Four-wave mixing experiments with extreme ultraviolet transient gratings. *Nature*, 520:205–208, 2015.
- [33] N.W. Ashcroft and N. David Mermin. *Solid State Physics*. Saunders College, 1976.

- [34] H.P. Gail and E. Sedlmayr. *Physics and Chemistry of Circumstellar Dust Shells*. Cambridge University Press, 2014.
- [35] E. Engel and R.M. Dreizler. *Density Functional Theory, Theoretical and Mathematical Physics*. Springer-Verlag Berlin Heidelberg, 2011.
- [36] W. Kohn and L.J. Sham. Self-consistent equations including exchange and correlation effects. *Phys. Rev.*, 140:A1133, 1965.
- [37] R.G. Parr and W. Yang. *Density-Functional Theory of Atoms and Molecules*. Oxford University Press, 1994.
- [38] H.O. Jeschke. Lectures on Computational Methods in Solid State Theory, Goethe-Universität Frankfurt  
[www.physics.okayama – u.ac.jp/jeschke\\_homepage/cmsst2016.html](http://www.physics.okayama-u.ac.jp/jeschke_homepage/cmsst2016.html).
- [39] P. Romaniello. *Time-Dependent Current-Density-Functional Theory for Metals*. PhD thesis, University of Groningen, 2006.
- [40] N.M. Harrison. Lectures on Density Functional Theory, Department of Chemistry, Imperial College London  
<https://www.ch.ic.ac.uk/harrison/teaching/dft2.pdf>.
- [41] P. Mori-Sánchez, A.J. Cohen, and W. Yang. Localization and Delocalization Errors in Density Functional Theory and Implications for Band-Gap Prediction. *Phys. Rev. Lett.*, 100:146401, 2008.
- [42] L. Li, T.E. Baker, S.R. White, and K Burke. Pure density functional for strong correlation and the thermodynamic limit from machine learning. *Phys. Rev. B*, 94:245129, 2016.
- [43] Y. Hao et al. Efficient electronic structure calculation for molecular ionization dynamics at high x-ray intensity. *Struct. Dyn.*, 2:041707, 2015.

- [44] S.-K. Son et al. Quantum-Mechanical Calculation of Ionization-Potential Lowering in Dense Plasmas. *Phys. Rev. X*, 4:031004, 2014.
- [45] B.F. Rozsnyai. Relativistic Hartree-Fock-Slater Calculations for Arbitrary Temperature and Matter Density. *Phys. Rev. A*, 5:1137, 1972.
- [46] F. Perrot and M.W.C. Dharma-wardana. Exchange and Correlation Potentials for Electron-Ion Systems at Finite Temperatures. *Phys. Rev. A*, 30:2619, 1984.
- [47] D. Shalitin. Exchange Energies and Potentials at Finite Temperatures. *Phys. Rev. A*, 7:1429, 1973.
- [48] J.C. Slater and G.F. Koster. Simplified LCAO method for the periodic potential problem. *Phys. Rev.*, 94:1498–524, 1954.
- [49] P. Pusching and C. Ambrosch-Draxl. Optical absorption spectra of semiconductors and insulators including electron-hole correlations: An *ab initio* study within the LAPW method. *Phys. Rev. B*, 66:165105, 2002.
- [50] M. Gajdos, K. Hummer, and G. Kresse. Linear optical properties in the projector-augmented wave methodology. *Phys. Rev. B*, 73:045112, 2016.
- [51] P. Nozières and D. Pines. Electron interaction in solids. General Formulation. *Phys. Rev.*, 109:741, 1958.
- [52] N.E. Brener. Random-phase-approximation dielectric functions for diamond, with local field effects included. *Phys. Rev. B*, 12:1487, 1975.
- [53] S. Baroni and R. Resta. Ab initio calculation of the macroscopic dielectric constant in silicon. *Phys. Rev. B*, 33:7017, 1986.
- [54] G.Y. Hu and R.F. O’Connell. Generalization of the Lindhard dielectric function to include fluctuation effects. *Phys. Rev. B*, 40:3600, 1989.

- [55] H. Ehrenreich and M.H. Cohen. Self-consistent field approach to the many-electron problem. *Phys. Rev.*, 115:786, 1959.
- [56] F. Trani, G. Cantele, D. Ninno, and G. Iadosini. Tight-binding calculation of the optical absorption cross section of spherical and ellipsoidal silicon nanocrystals. *Phys. Rev. B*, 72:075423, 2005.
- [57] C.F. Klingshirn. *Semiconductor optics*. Springer, Berlin, 1997.
- [58] H.J. Monkhorst and J.D. Pack. Special points for Brillouin-zone integrations. *Phys. Rev. B*, 13:5188, 1976.
- [59] Y.K. Kim and M.E. Rudd. Binary-encounter-dipole model for electron-impact ionization. *Proc. R. Soc. London Ser. A*, 126:259, 1930.
- [60] N.F. Mott. The wave mechanics of  $\alpha$ -ray tracks. *Phys. Rev. A*, 50(5):3954–3967, 1994.
- [61] Z. Jurek, B. Ziaja, and R. Santra. Applicability of the classical molecular dynamics method to study x-ray irradiated molecular systems. *J. Phys. B*, 47:124036, 2014.
- [62] B. Ziaja, R.A. London, and J. Hajdu. Ionization by impact electrons in solids: Electron mean free path fitted over a wide energy range. *J. Appl. Sci.*, 99:033514, 2006.
- [63] R.H. Ritchie and A. Howie. Electron excitation and the optical potential in electron microscopy. *Philos. Mag.*, 36:463–481, 1977.
- [64] N. Medvedev. Modeling Ultrafast Electronic Processes in Solids Excited by Femtosecond VUV-XUV Laser Pulse. *AIP Conf. Proc.*, 1464:582, 2012.
- [65] L. van Hove. Correlations in Space and Time and Born Approximation Scattering in Systems of Interacting Particles. *Phys. Rev.*, 95:249, 1954.

- [66] S. Galambosi. *Electronic excitations in solids studied using inelastic x-ray scattering*. Helsinki: Report series in physics, 2007.
- [67] A. Akkerman et al. Inelastic Electron Interactions in Insulators. *Phys. Stat. Sol. B*, 198:769, 1996.
- [68] J.-Ch. Kuhr and H.-J. Fitting. Monte Carlo simulation of electron emission from solids. *J. Electron Spectr. And Rel. Phenom.*, 105:257, 1999.
- [69] A.P. Horsfield, P.D. Godwin, D.G. Pettifor, and A.P. Sutton. Computational materials synthesis. I. A tight-binding scheme for hydrocarbons. *Phys. Rev. B*, 54:15773–5, 1996.
- [70] C. Molteni, L. Colombo, and L. Miglio. Tight-binding molecular dynamics in liquid II-V compounds: I. Potential generation. *J. Phys.: Condens. Matter*, 6:5243, 1994.
- [71] W.A. Harrison. *Electronic Structure and Properties of Solids*. San Francisco, CA: Freeman, 1980.
- [72] R. Virkkunen, K. Laasonen, and R.M. Nieminen. Molecular dynamics using the tight-binding approximation: application to liquid silicon. *J. Phys.: Cond. Matter*, 3:7455, 1991.
- [73] M. Parrinello and A. Rahman. Crystal structure and pair potentials: a molecular-dynamics study. *Phys. Rev. Lett.*, 45:1196–9, 1980.
- [74] M.P. Allen and D.J. Tildesley. *Computer Simulation of Liquids*. Oxford University Press, 1987.
- [75] B. Rethfeld et al. Interaction of dielectrics with femtosecond laser pulses: application of kinetic approach and multiple rate equation. *Appl. Phys. A: Mater. Sci. Process.*, 101:19–25, 2010.
- [76] N. Medvedev, Z. Li, V. Tkachenko, and B. Ziaja. Electron-ion coupling in semiconductors beyond Fermi’s golden rule. *Phys. Rev. B*, 95:014309, 2017.

- [77] N. Medvedev et al. Short-time electron dynamics in aluminium excited by femtosecond extreme ultraviolet radiation. *Phys. Rev. Lett.*, 107(16):165003, 2011.
- [78] C.H. Yoon et al. A comprehensive simulation framework for imaging single particles and biomolecules at the European X-ray Free-Electron Laser. *Sci. Rep.*, 6:24791, 2016.
- [79] Z. Jurek, G. Faigel, and M. Tegze. Dynamics in a cluster under the influence of intense femtosecond hard X-ray pulses. *Eur. Phys. J. D*, 29(2):217–229, 2004.
- [80] E.D. Palik. *Handbook of Optical Constants of Solids*. Academic Press, New York, 1985.
- [81] Y.M. Niquet, C. Delerue, G. Allan, and M. Lannoo. Method for tight-binding parametrization: Application to silicon nanostructures. *Phys. Rev. B*, 62:5109, 2000.
- [82] C. Tserbak, H.M. Polatoglou, and G. Theodorou. Unified approach to the electronic structure of strained Si/Ge superlattices. *Phys. Rev. B*, 47:7104, 1993.
- [83] G. Jaeger. *Archive for History of Exact Sciences*. Springer-Verlag Berlin Heidelberg, 1998.
- [84] V. Lipp. *Atomistic-continuum modeling of ultrafast laser-induced melting of silicon targets*. PhD thesis, University of Kassel, 2015.
- [85] S.J. Blundell and K.M. Blundell. *Concepts in thermal physics*. Oxford University Press, 2010.
- [86] J. Gaudin et al. Photon energy dependence of graphitization threshold for diamond irradiated with an intense XUV FEL pulse. *Phys. Rev. B*, 88:060101, 2013.
- [87] R.W. Carlson. *The mantle and core: Treatise on Geochemistry*. Elsevier-Pergamon Oxford, 2005.

- [88] F.P. Bundy, H.T. Hall, H.M. Strong, and R.H. Wentorf. Man-made diamonds. *Nature*, 176:51–55, 1955.
- [89] H. Tracy Hall. Ultrahigh-pressure research. *Science*, 128:445–449, 1958.
- [90] A.V. Palnichenko et al. Diamond formation by thermal activation of graphite. *Nature*, 402:162–165, 1999.
- [91] J.C. Angus and C.C. Hayman. Low pressure, metastable growth of diamond and “diamondlike” phases. *Science*, 241:913–921, 1988.
- [92] I.S. Grigor’ev and E.Z. Meilikhov. *Fizicheskie velichiny: Spravochnik (Physical Quantities. Handbook)*. Moscow: Energoatomizdat, 1991.
- [93] A.M. Zaitsev. *Optical properties of diamond: a data handbook*. Springer-Verlag Berlin Heidelberg, 2001.
- [94] V.A. Bushuev. Effect of the thermal heating of a crystal on the diffraction of pulses of a free-electron x-ray laser. *Bulletin of the Russian Academy of Sciences: Physics*, 77(1):15–20, 2013.
- [95] G. Davies and T. Evans. Graphitization of diamond at zero pressure and at a high pressure. *Proc. R. Soc. Lond. A*, 328:413–27, 1972.
- [96] D.H. Reitze, H. Ahn, and M.C. Downer. Optical properties of liquid carbon measured by femtosecond spectroscopy. *Phys. Rev. B*, 45:2677, 1992.
- [97] H.O. Jeschke and M.E. Garcia. Theoretical description of the ultrafast ablation of diamond and graphite: dependence of thresholds on pulse duration. *Appl. Surf. Sci.*, 197-198:839, 2002.
- [98] V. Tkachenko, N. Medvedev, and B. Ziaja. Transient changes of optical properties in semiconductors in response to femtosecond laser pulses. *Appl. Sci.*, 6(9):238, 2016.

- [99] B.T. Draine and H.M. Lee. Optical properties of interstellar graphite and silicate grains. *Astr. J.*, 258:89–108, 1984.
- [100] G.A. Thomas et al. Optical study of interacting donors in semiconductors. *Phys. Rev. B*, 23:5472, 1981.
- [101] R. Huber et al. How many-particle interactions develop after ultrafast excitation of an electron-hole plasma. *Nature*, 414:286–289, 2001.
- [102] R. Singla et al. THz-Frequency Modulation of the Hubbard U in an Organic Mott Insulator. *Phys. Rev. Lett.*, 115:187401, 2015.
- [103] N. Medvedev, V. Tkachenko, and B. Ziaja. Modeling of nonthermal solid-to-solid phase transition in diamond irradiated with femtosecond x-ray FEL pulse. *Contrib. Plasma Phys.*, 55:12, 2015.
- [104] D. Fisher et al. Interband and intraband (Drude) contributions to femtosecond laser absorption in aluminum. *Phys. Rev. E*, 65:016409, 2002.
- [105] T. Evans and P.F. James. A study of the transformation of diamond to graphite. *Proc. R. Soc. A*, 277:260, 1964.
- [106] A. De Vita, G. Galli, A. Canning, and R. Car. A microscopic model for surface-induced diamond-to-graphite transitions. *Nature*, 379:523, 1996.
- [107] Y. G. Gogotsi, A. Kailer, and K.G. Nickel. Materials: Transformation of diamond to graphite. *Nature*, 401:663, 1999.
- [108] H. Chacham and L. Kleinman. Instabilities in diamond under high shear stress. *Phys. Rev. Lett.*, 85:4904, 2000.
- [109] K. Sokolowski-Tinten, J. Bialkowski, and D. von der Linde. Ultrafast laser-induced order-disorder transitions in semiconductors. *Phys. Rev. B*, 51:14186, 1995.

- [110] F. Tavella et al. Soft x-rays induce femtosecond solid-to-solid phase transition. *arXiv:1612.06698*, 2016.
- [111] Website for calculation of x-ray attenuation length in solids [henke.lbl.gov/optical\\_constants/atten2.html](http://henke.lbl.gov/optical_constants/atten2.html).
- [112] L.S. Pan and D.R. Kania. *Diamond: Electronic Properties and Applications*. Springer US, New York, 1995.
- [113] H.O. Jeschke, M.E. Garcia, and K.H. Bennemann. Microscopic analysis of the laser-induced femtosecond graphitization of diamond. *Phys. Rev. B*, 60:R3701(R), 1999.
- [114] A.N. Tikhonov and A.A. Samarskii. *Equations of mathematical physics*. Oxford Pergamon Press, 1963.
- [115] M. Kozák, F. Trojánek, and P. Malý. Hot-carrier transport in diamond controlled by femtosecond laser pulses. *New J. Phys.*, 17:053027, 2015.
- [116] A.N. Bogolyubov and V.V. Kravtsov. *Zadachi po matematicheskoi fizike (Exercises on Mathematical Physics)*. Izdatel'stvo MGU, 1998.
- [117] M.A. Osman. High-temperature transport of electrons in diamond. *Physica B*, 185:471–474, 1993.
- [118] C. Kittel. *Introduction to Solid State Physics, 6th Ed.* New York:John Wiley, 1986.
- [119] P.L. Silvestrelli, A. Alavi, M. Parrinello, and D. Frenkel. *Ab initio* molecular dynamics simulation of laser melting of silicon. *Phys. Rev. Lett.*, 77:3149, 1996.
- [120] C.V. Shank, R. Yen, and C. Hirlimann. Time-resolved reflectivity measurements of femtosecond-optical-pulse-induced phase transitions in silicon. *Phys. Rev. Lett.*, 50:454, 1983.
- [121] K. Sokolowski-Tinten and D. von der Linde. Generation of dense electron-hole plasmas in silicon. *Phys. Rev. B*, 61:2643, 2000.

- [122] Z. Li, M.E.-A. Madjet, and O. Vendrell. Non-Born-Oppenheimer dynamics of the photoionized Zundel cation: A quantum wavepacket and surface-hopping study. *J. Chem. Phys.*, 138:094313, 2013.
- [123] T. Zier et al. Signatures of nonthermal melting. *Struct. Dyn.*, 2:054101, 2015.
- [124] K. Sugioka and Y. Cheng. *Ultrafast Laser Processing: From Micro- to Nanoscale*. Pan Stanford Publishing, 2013.
- [125] Z. Lin, L. Zhigilei, and V. Celli. Electron-phonon coupling and electron heat capacity of metals under conditions of strong electron-phonon nonequilibrium. *Phys. Rev. B*, 77:075133, 2008.
- [126] B. Rethfeld, A. Kaiser, M. Vicanek, and G. Simon. Ultrafast dynamics of nonequilibrium electrons in metals under femtosecond laser irradiation. *Phys. Rev. B*, 73:214303, 2002.
- [127] P.B. Allen. Theory of thermal relaxation of electrons in metals. *Phys. Rev. Lett.*, 59:1460–1463, 1987.
- [128] J. Vorberger, D. O. Gericke, T. Bornath, and M. Schlanges. Energy relaxation in dense, strongly coupled two-temperature plasmas. *Phys. Rev. E*, 81:046404, 2010.
- [129] N.H. March and M.P. Tosi. *Atomic Dynamics in Liquids*. Courier Corporation, 1991.
- [130] A. Volkov and V. Borodin. Heating of metals in swift heavy ion tracks by electron-ion energy exchange. *Nucl. Inst. Meth. Phys. Res. Sec. B: Beam Interactions with Materials and Atoms*, 146:137–141, 1998.
- [131] L.D. Landau and E.M. Lifshitz. *Quantum Mechanics, Third Edition: Non-Relativistic Theory*. Butterworth-Heinemann, 1976.
- [132] B.Y. Mueller and B. Rethfeld. Relaxation dynamics in laser-excited metals under nonequilibrium conditions. *Phys. Rev. B*, 87:035139, 2013.

- [133] J.C. Tully. Molecular dynamics with electronic transitions. *J. Chem. Phys.*, 93:1061, 1990.
- [134] C. Gahl et al. A femtosecond X-ray/optical cross-correlator. *Nat. Photonics*, 2:165–169, 2008.
- [135] O. Krupin et al. Temporal cross-correlation of x-ray free electron and optical lasers using soft x-ray pulse induced transient reflectivity. *Opt. Express*, 20:11396, 2012.
- [136] G. Grosso and G. Pastori Parravicini. *Solid State Physics*. San Diego: Academic Press, 2000.
- [137] F.J. Blatt. *Modern Physics*. McGraw-Hill, 1992.
- [138] B. Ziaja et al. Time-resolved observation of band-gap shrinking and electron-lattice thermalization within X-ray excited gallium arsenide. *Sci. Rep.*, 5:18068, 2015.
- [139] A. Haug. Auger recombination in direct-gap semiconductors: band-structure effects. *J. Phys C*, 16:4159, 1983.
- [140] N. Sano and A. Yoshii. Impact-ionization theory consistent with a realistic band structure of silicon. *Phys. Rev. B*, 45:4171, 1992.
- [141] R.P. Joshi and R.O. Grondin and D.K. Ferry. Monte Carlo simulation of electron-hole thermalization in photoexcited bulk semiconductors. *Phys. Rev. B*, 42:5685, 1990.
- [142] R. Tommassi and P. Langot and F. Vallee. Femtosecond hole thermalization in bulk GaAs. *Appl. Phys. Lett.*, 66:1361, 1995.
- [143] M. Hajlaoui et al. Tuning a Schottky barrier in a photoexcited topological insulator with transient Dirac cone electron-hole asymmetry. *Nat. Commun.*, 5:3003, 2014.
- [144] M. Bernardi et al. Ab initio study of hot electrons in GaAs. *Proc. National Acad. Sci.*, 112:5291–5296, 2015.

- [145] N. Vast, J. Sjakste, and V. Tyuterev. Ab initio method for the electron-phonon scattering times in semiconducting nanostructures. *2008 APS March Meeting*, 53, 2008.
- [146] N. Del Fatti, P. Langot, R. Tommasi, and F. Vallée. Temperature-dependent electron-lattice thermalization in GaAs. *Phys. Rev. B*, 59:4576, 1999.
- [147] J.F. Young, T. Gong, P.M. Fauchet, and P.J. Kelly. Carrier-carrier scattering rates within nonequilibrium optically injected semiconductor plasmas. *Phys. Rev. B*, 50:2208, 1994.
- [148] B.E.A. Saleh and M.C. Teich. *Fundamentals of Photonics*. J. Wiley and Sons, 1991.
- [149] S.I. Anisimov, B.L. Kapeliovich, and T.L. Perelman. Electron emission from metal surfaces exposed to ultrashort laser pulses. *Sov. Phys. JETP*, 39:375, 1974.
- [150] Solid state physics II: Optical Properties of Solids  
<http://web.mit.edu/course/6/6.732/www/6.732-pt2.pdf>.
- [151] B. Ziaja, D. van der Spoel, A. Szöke, and J. Hajdu. Auger-electron cascades in diamond and amorphous carbon. *Phys. Rev. B*, 64:214104, 2001.
- [152] V. Siklitsky. Ioffe Physico-Technical Institute. Database on Semiconductors  
<http://www.ioffe.rssi.ru/sva/nsm/semicond>.
- [153] N. Medvedev and B. Rethfeld. Transient dynamics of the electronic subsystem of semiconductors irradiated with an ultrashort vacuum ultraviolet laser pulse. *New J. Phys.*, 12:073037, 2010.
- [154] N. Medvedev et al. Electron Kinetics in Femtosecond X-ray Irradiated SiO<sub>2</sub>. *Contrib. Plasma Phys.*, 53:347, 2013.
- [155] J.S. Blakemore. Semiconducting and other major properties of gallium arsenide. *J. Appl. Phys.*, 53:R123, 1982.

- [156] M.D. Sturge. Optical Absorption of Gallium Arsenide between 0.6 and 2.75 eV. *Phys. Rev.*, 127:768, 1962.
- [157] R. Gunnella et al. Ultrafast reflectivity dynamics of highly excited Si surfaces below the melting transition. *Phys. Rev. B*, 94:155427, 2016.
- [158] H.M. van Driel. Kinetics of high-density plasmas generated in Si by 1.06- and 0.53- $\mu\text{m}$  picosecond laser pulses. *Phys. Rev. B*, 35:8166, 1987.
- [159] T.H. Liu et al. Electron scattering channels in GaAs: A fully first-principles study of electron transport. *arXiv:1606.07074*.
- [160] A. Ruiz-Serrano, N.D.M. Hine, and C.-K. Skylaris. Pulay forces from localized orbitals optimized *in situ* using a psinc basis set. *J. Chem. Phys.*, 136:234101, 2012.
- [161] P. Pulay. *Ab initio* calculation of force constants and equilibrium geometries in polyatomic molecules. I. Theory. *Mol. Phys.*, 17:197–204, 1969.
- [162] M.S. Murillo and J.C. Weisheit. Dense plasmas, screened interactions, and atomic ionization. *Phys. Reports*, 302:11–18, 1998.
- [163] A.P. Sorini. *The Passage of Fast Electrons Through Matter*. PhD thesis, University of Washington, 2008.
- [164] B. Nagler. X-ray sources: Tabletop X-ray lasers. *Nat. Photonics*, 6:719–720, 2012.
- [165] S.L. Cousin et al. High-flux table-top soft x-ray source driven by sub-2-cycle, CEP stable, 1.85- $\mu\text{m}$  1-kHz pulses for carbon K-edge spectroscopy. *Opt. Lett.*, 39:5383–5386, 2014.
- [166] L. Verlet. Computer 'experiments' on classical fluids. I. Thermodynamical properties of Lennard-Jones molecules. *Phys. Rev.*, 159:98–103, 1967.
- [167] R.W. Hockney. The potential calculation and some applications. *Methods Comput. Phys.*, 9:136–211, 1970.

- [168] D. Potter. *Computational Physics*. Wiley, New York, 1972.
- [169] C.H. Xu, C.Z. Wang, C.T. Chan, and K.M. Ho. A transferable tight-binding potential for carbon. *J. Phys. Cond. Mat.*, 4:6047–54, 1992.
- [170] I. Kwon et al. Transferable tight-binding models for silicon. *Phys. Rev. B*, 49:7242–50, 1994.

# Acknowledgement

This work would not be possible without help of several people and first of all, my supervisor Beata Ziaja. From the first day of my PhD career at DESY until the completion of the thesis she was taking care of me, directing my research, coming up with new ideas, giving valuable advices, promoting publications. Despite being busy with many other projects she could always find a time for me when I needed. Due to her numerous contacts with other scientific groups, I got an opportunity to collaborate with different scientists including experimentalists. My co-supervisor and our group leader Robin Santra was also always helpful and stimulated many useful discussions, especially concerning quantum mechanical aspects. The organization of work in his group is on a very high level.

Nikita Medvedev was another key person, whose development XTANT was a vital part of my study. I thank him for his continuous help both with physics and computing, preparation to the conferences and brushing up my texts. Even after moving from DESY he didn't stop participating in our joint investigations, and I'm very grateful to him for that. Another compatriot of mine, Vladimir Lipp, after joining the CFEL DESY Theory group helped me in different aspects as well, so I also express my thanks to him.

I would like to thank Franz Tavella from LCLS, Sven Toleikis and Hauke Höppner from DESY for their experiment on graphitization at FERMI@Elettra and future joint analysis of experimental and theoretical data. It was a great experience to work with such people.

CFEL colleagues, Zheng Li, Theophilos Maltezopoulos, Wilfried Wurth, and Przemysław Piekarczyk from Polish Academy of Sciences are acknowledged for their co-authorship in the publications I am involved and the joint work on them. I would also like to give my thankfulness to all of my group members, current and former. Sang-Kil Son and Ludger

Inhester told me much about XMOLECULE, Antonia Karamatskou kindly helped me with translation of the Abstract into German, valuable discussions with Oriol Vendrell, Zoltan Jurek, John Bekx are acknowledged. Special thanks are going to Otfried Geffert, who provided IT environment in our group, including work on cluster machines. In this regard, people organizing the work at DESY Maxwell cluster are thanked as well.

I would like to send my separate thanks to Vladimir Alexeevich Bushuev, my supervisor at Moscow State University during my undergraduate study. He brought me to the field of X-ray and FEL science, and was the first person who told me about DESY and the European XFEL in many details.

At the end, I say that I am very grateful to my parents, younger brother and to my wife Olga who always supported me during my PhD study. I thank all of our friends too. The family and friends encouraged me to do all my best to succeed with my thesis.

# Eidesstattliche Versicherung

Hermit erkläre ich an Eides statt, dass ich die vorliegende Dissertationsschrift selbst verfasst und keine anderen als die angegebenen Quellen und Hilfsmittel benutzt habe.

*I hereby declare, on oath, that I have written the present dissertation by my own and have not used other than the acknowledged resources.*

Hamburg, den

Unterschrift

*Hamburg, date*

*Signature*